UNIVERSITY OF CALIFORNIA, SAN DIEGO

Thermodynamic Modeling of Grain Boundary Complexions and Developing Grain Boundary Complexion Diagrams for Multicomponent Metallic Systems

A dissertation submitted in partial satisfaction of the
requirements for the degree Doctor of Philosophy

in

Materials Science and Engineering

by

Naixie Zhou

Committee in charge:

Professor Jian Luo, Chair
Professor Shyue Ping Ong
Professor Yu Qiao
Professor Kenneth S. Vecchio
Professor Kesong Yang

2017

The Dissertation of Naixie Zhou is approved, and it is acceptable in quality and form for publication on microfilm and electronically:

_____

_____

_____

_____

_____

Chair

University of California, San Diego

2017

DEDICATION

To

Tianhong Li and Zhicheng Zhou

TABLE OF CONTENTS

LIST OF FIGURES

LIST OF TABLES

ACKNOWLEDGEMENTS

First of all, I would like to thank my advisor, Dr. Jian Luo, for his immense patience, motivation and support, which are vital in making this dissertation a reality. Dr. Luo is a great advisor. He spent endless hours proofreading my research papers and providing excellent advices on improving my writing and presentation skills. He taught me how to be a professional researcher and guided me to overcome all the problems and difficulties I encountered during my graduate research. My appreciation for his guidance and continuous support is immeasurable. I am also very grateful to Dr. Shyue Ping Ong and Dr. Kesong Yang for being on my advisory committee and providing inspiring suggestions on materials modelings. I would like to further thank Dr. Kenneth S. Vecchio for being on my committee as well as his helpful suggestions on my experiment design. I would also extend my deepest gratitude to Dr. Yu Qiao for his time and guidance.

Secondly, I would like to thank my collaborators Dr. Tao Hu and Dr. Shengfeng Yang, from whom I learnt a lot of new experimental and simulation skills. I'm also grateful to colleagues Dr. Jae-Il, Dr. Yuangyao Zhang, Jiajia Huang, Mingde Qin, Sicong Jiang, Josh Gild, Richard Tran, Zihan Xu, Timothy Huang, Mojitaba Samiee and Zhao Zhang, who have helped me in many ways.

Finally, I would like to express my gratitude to Dr. Zhiyang Yu at Xiamen University of Technology, and Dr. Martin Harmer at Lehigh University for their invaluable help throughout the MURI projects.

I acknowledge the financial support from the U.S. Air Force Office of Scientific Research, the U.S. Office of Naval Research, DOE-NETL and NSF.

Chapter 1, in part, is a reprint of the material "GB complexions in multicomponent alloys: Challenges and opportunities" as it appears in Current Opinion in Solid State and Materials Science, Naixie Zhou, Tao Hu, and Jian Luo, 2016, 20, 268-277. The dissertation author was the primary investigator and author of this paper. All experiments and data analysis were performed by the author.

Chapter 2, in part, is a reprint of the material "Developing GB diagrams for multicomponent alloys" as it appears in Acta Materialia, Naixie Zhou and Jian Luo, 2015, 91, 202-216. The dissertation author was the primary investigator and author of this paper. All calculations and data analysis were performed by the author except for some of the sintering data.

Chapter 3, in part, is a reprint of the material "Calculation and validation of a GB complexion diagram for Bi-doped Ni" as it appears in Scripta Materialia, Naixie Zhou, Zhiyang Yu, Yuanyao Zhang, Martin P. Harmer, and Jian Luo, 2017, 130, 165-169. The dissertation author was the primary investigator and author of this paper. All experiments and data analysis were performed by the author except for the sample preparation and TEM characterization data.

Chapter 5, in part, is a reprint of the material "Developing thermodynamic stability diagrams for equilibrium-grain-size binary alloys" as it appears in Materials Letters, Naixie Zhou and Jian Luo, 2014, 115, 268-271. The dissertation author

was the primary investigator and author of this paper. All calculations and data analysis were performed by the author.

Chapter 6, in part, is a reprint of the material " Stabilization of nanocrystalline alloys at high temperatures via utilizing high-entropy GB complexions" as it appears in Scripta Materialia, Naixie Zhou, Tao Hu, Jiajia Huang, and Jian Luo, 2016, 124, 160-163. The dissertation author was the primary investigator and author of this paper. All experiments and data analysis were performed by the author except for the TEM characterization data.

VITA

2007 B.S. Shanghai Jiaotong University, People's Republic of China

2010 M.S. Shanghai Jiaotong University, People's Republic of China

2017 Ph.D. University of California, San Diego, USA

PUBLICATIONS

1. **N. Zhou**, Z. Yu, Y. Zhang, M. Harmer, J. Luo "Calculation and Validation of a GB Complexion Diagram for Bi-doped Ni" Scripta Mater. (2017) 130, 165-169
2. **N. Zhou**, T. Hu, J. Huang, J. Luo "Stabilization of nanocrystalline alloys at high temperatures via utilizing high-entropy GB complexions" Scripta Materialia (2016) 124, 160-163
3. J. Gild, Y. Zhang, T. Harrington, S. Jiang, T. Hu, M. C. Quinn, W. M. Miller, **N. Zhou**, K. Vecchio, J. Luo "High-Entropy Metal Diborides: A New Class of High-Entropy Materials and a New Type of Ultrahigh Temperature Ceramics" Scientific Report (2016) 6, 37946
4. **N. Zhou**, T. Hu, J. Luo "GB complexions in multicomponent alloys: Challenges and opportunities" Current Opinion in Solid State and Materials Science (2016) 20, 268-277
5. R. Tran, Z. Xu, **N. Zhou**, B. Radhakrishnan, J. Luo, S.P. Ong "Computational study of metallic dopant segregation and embrittlement at molybdenum grain boundaries" Acta Materialia (2016) 117, 91-99
6. **N. Zhou**, J. Luo "Developing GB diagrams for multicomponent alloys" Acta Materialia (2015) 91 202-216

7. **N. Zhou**, J. Luo “Developing thermodynamic stability diagrams for equilibrium-grain-size binary alloys” Materials Letters (2014) 115, 268-271
8. S. Ma, P.R. Cantwell, T.J. Pennycook, **N. Zhou**, et al. “GB complexion transitions in WO3 and CuO doped TiO2 bicrystals” Acta Materialia (2013) 61, 1691-1704
9. J.I. Jung, **N. Zhou**, J. Luo “Effects of sintering aids on the densification of Mo–Si–B alloys” Journal of Materials Science (2012) 47, 8308-8319

ABSTRACT OF THE DISSERTATION

Thermodynamic Modeling of Grain Boundary Complexions and Developing Grain Boundary Complexion Diagrams for Multicomponent Metallic Systems

by

Naixie Zhou

Doctor of Philosophy in Materials Science and Engineering

University of California, San Diego, 2017

Professor Jian Luo, Chair

Grain boundaries (GBs) in crystalline materials can be treated as interfacial phases which are called complexions. Like bulk phases, GB complexions can undergo first-order or continuous transitions with varying thermodynamic potential and such GB complexion transitions can cause abrupt changes in structure and chemistry of GBs, thereby critically influencing a broad range of interfacial controlled materials' properties such as sintering, grain growth, creep, embrittlement, electrical/thermal/ionic conductivity. Specifically, the presence of

multiple dopants and impurities can significantly alter the GB complexion formation and transition.

In this work, a thermodynamic framework is developed to forecast the thermodynamic tendency to form disordered premelting-like GB complexions in multicomponent alloys with consideration of the interactions between alloying components and multiple phase equilibrium. Subsequently, the framework was applied to W–Ni–M (M = Fe, Co, Cr, Zr, Nb and Ti) and Mo–Si–B–M (M = Ni, Co and Fe) systems to predict the sintering behaviors in these systems by calculating their ternary and quaternary GB diagrams.

In the second part, GB adsorption transitions are studied using an Ising type lattice model. The GB complexion diagram is computed for the average general GBs in Bi-doped Ni. The predictions are calibrated with previously-reported density functional theory calculations and further validated by aberration corrected scanning transmission electron microscopy characterization results as well as prior Auger electron spectroscopy measurements. Subsequently, a systematics of GB adsorption transitions is derived using the model. A normalized segregation strength is defined to represent the effects of mixing energy, solute strain and differential bonding energies as well as the misorientation for symmetrical twist boundaries, which is shown to be a dominant factor in controlling adsorption transition behaviors. This derived systematics of GBs exhibits phenomenological similarities to the cases of multilayer adsorption of inert gas molecules on the

surfaces of attractive substrates, enriches the classical GB segregation/adsorption theory.

In the third part, bulk computational thermodynamics are extended to model binary poly/nanocrystalline alloys by incorporating GB energies computed by a multilayer adsorption model. A new kind of stability diagram for equilibrium-grain-size poly/nanocrystalline alloys is developed. Computed results for Zr-doped Fe are validated by prior experiments and provide new physical insights regarding stabilization of nanoalloys and its relation to solid-state amorphization.

In the final part, the effect of multicomponent alloying on the thermal stability of nanocrystalline alloys is studied. By introducing more alloying components, the GB energy can be reduced more significantly via both bulk and grain-boundary high-entropy effects with increasing temperature at/within the solid solubility limit, thereby reducing the thermodynamic driving force for grain growth. Moreover, GB migration can be hindered by sluggish kinetics. The theory is supported by numerical experiments and experiments in Ni systems, and it provide guidance for developing thermally stable nanocrystalline alloys that can be used in extreme condition.

Chapter 1. Introduction

1.1. Motivation and outline.

Grain boundaries (GBs) in crystalline materials can be treated as "interfacial phases" that can undergo first-order or continuous transitions with varying thermodynamic potentials, such as temperature (T), pressure (P), and chemical potentials (μ). Recently, a new term "complexion" was introduced to differentiate such interfacial phases, which are thermodynamically two-dimensional (2D, while the variations in composition and structure in the third dimension is thermodynamically-determined and fixed) and cannot exist alone without abutting bulk phases, from the bulk phases defined by Gibbs [1-5].

A variety of GB complexions have been observed via high resolution electron microscopy (HREM) and aberration-corrected scanning transmission electron microscopy (AC STEM) as Fig. 1.1 shows. One common type of GB complexions is represented by the equilibrium intergranular films (IGFs) that are widely observed in ceramics [6]. Similar impurity-based, quasi-liquid, interfacial films have also been observed at GBs in metals such as W-Ni and Mo-Ni (where the primary phase is underlined) [7-10] and on oxide surfaces [11-23]. Dillon and Harmer [24-27] further discovered a series of discrete GB complexions in Al_2O_3-based ceramics, which may be considered as derivatives to IGFs with (nominal) discrete thicknesses of 0, 1, 2, 3, x, and $+\infty$ atomic layers, respectively [3, 28-30]. This series of Dillon-Harmer complexions have also been observed in other materials such as TiO_2-CuO-SiO_2 [28]; moreover, bilayer complexions have been

directly observed by AC STEM in metallic alloys such as Ni-Bi [31] and Cu-Bi [32], as well as in Si-Au [33].

GB complexion transitions can often result in the abrupt changes in GB structure and chemistry, which can in turn drastically alter various properties such as GB cohesion (embrittlement) [31, 32], ductility [34], GB mobility (normal and abnormal grain growth) [24-27], GB diffusivity (activated sintering) [7, 9, 10, 21, 29, 35-38], and ionic conductivity [39].

For the purpose of tailoring materials macroscopic properties by controlling GB complexions, a comprehensive understanding of the formation mechanisms for GB complexions is desirable and imperative. Various GB models were developed to describe the GB complexion formation and transition. Using the Mclean-type segregation model, Hart [40], in 1968, first postulated that GBs can be considered as 2-D interfacial phases that may undergo first order interface transformations. Hondros and Seah [41], Cahn [42, 43] further elaborated such idea by exploring equilibrium GB states via lattice-gas-based GB models. Recently, Wynblatt and Chatain [44] have developed more sophisticated lattice-gas segregation models [44, 45] based on a regular solution type model, by which, they demonstrated the existence of multilayer solid-state GB prewetting transition, that are analogous to the prewetting transition described by Cahn's critical-point wetting model for a binary de-mixed liquid [46]. Later Rickman et al. [47] derived the interaction between GBs and segregants from elastic theories and a series of first order layering GB transitions were also found in his study. In parallel, Tang *et*

al. [1, 2] and Mishin *et al.* [48] used diffuse-interface (phase-field type) models to describe coupled GB prewetting and premelting transitions. The formation and stability of premelting-like GB complexions (enhanced by concurrent GB adsorption or prewetting) in binary alloys have also been treated by a sharp-interface model, where a new type of GB λ diagrams have been constructed to present the thermodynamic tendency for average general GBs to disorder [7, 29, 36-38]; although GB λ diagrams are not rigorous GB complexion diagrams with well-defined transition lines and critical points, they have been validated by direct HRTEM and proven useful for predicting trends in activated sintering [7, 29, 36-38]. Rickman *et al.* also demonstrated the existence of a series of first-order layering GB transitions using a lattice model by considering elastic interactions between GBs and adsorbates [47]. GB transitions have also been modeled by Frolov *et al* using molecular dynamics simulations [49-52].

For the purpose of enriching the theory of GB adsorption and transitions as well as exploring the application of GB complexion theories in materials design, the objective of this thesis are divided into three folds: 1) extending the GB thermodynamic models to many-component systems and construct GB complexion diagrams for many-component systems, 2) investigating a systematics of GB adsorption transitions that unites the wetting, prewetting, layering, and roughening transitions into a coherent picture by finding the key parameter controlling GB adsorption and transitions, 3) predicting the thermal stability of grain

sizes in nanocrystalline alloys and designing thermodynamically thermal stable nanocrystalline alloys by GB thermodynamic modeling.

Chapter 1. gives an introduction of interfacial complexions and typical thermodynamic models for GB complexions. **Chapter 2** is focused on constructing GB complexion diagrams in multicomponent alloys by thermodynamic modeling. The modeling results are validated by sintering experiments in Mo and W systems. **Chapter 3** explores the GB complexion transition in Ni-Bi systems. A thermodynamic description of layered complexion states is developed with a lattice-type GB statistical model and the modeling results are validated with density functional theory calculations and TEM observations. **Chapter. 4** investigates the systematics of GB complexion transition generated by a multi-layer lattice-type GB statistical model. A normalized segregation strength is defined to represent the overall effect of materials' intrinsic properties and GB misorientation angles on the complexion transition behaviors, and 3-D GB complexion diagrams can be constructed in the space of normalized segregation strength, normalized temperature and chemical potential (composition). In **Chapter 5**, the multilayer GB adsorption model was applied to the calculation of equilibrium grain size diagram for predicting and designing thermodynamically stable nanocrystalline alloys. **Chapter 6** studied the effect of multicomponent alloying on the thermal stability of nanocrystalline alloys. A theory of reducing GB energy with increasing temperature using high entropy GBs is developed and used to guide the design of nanocrystalline Ni alloys with grain size stability up to 1000 ^{o}C. **Chapter 7**

summarizes the work in this thesis and proposes the research plan for the future study.

1.2. GB thermodynamic models

Gibbs [53] first introduced the thermodynamic description of interfacial adsorption phenomenon over a century ago. The famous Gibbs adsorption equation can be expressed as:

$$d\gamma = -s^{ex}dT - \sum_i \Gamma_i d\mu_i \quad (1)$$

where s^{ex} is the excess entropy of the interface, Γ is the interfacial adsorption with subscript denoting the component species and μ is the chemical potential. For a binary system, a useful relation can be derived from Eq. (1) as:

$$-\Gamma_{2,1} = d\gamma/d\mu_2 \quad (2)$$

where $\Gamma_{2,1}$ is the relative adsorption representing the adsorption of second component at the interface by choosing the dividing surface so as to make the first component's adsorption vanish in Eq. (1). Eq. (2) relates the adsorption to the variation of interfacial energy and bulk chemical potential (or bulk composition). However, there are several shortcomings of Gibbsian adsorption isotherm that limit its usefulness in GB problems:

1. γ and its derivative to bulk chemical potential (or bulk composition) are not easy to measure in solids.
2. $\Gamma_{2,1}$ can only be measured directly when the composition profiles (or the distributions of components) along the interface for all components are

specified. Otherwise, the dividing surface of the interface cannot be determined so the Gibbs adsorption isotherm cannot be integrated.

Such limitations prompted the later development of GB analytical models based on the statistical thermodynamics.

1.2.1. Monolayer GB models

McLean [54] developed a classic interfacial adsorption model, which assumes that the GB segregation is limited to a monolayer of atomic sites at GBs and both GB sites and bulk sites are ideal solutions. By his model, a segregation isotherm is derived as:

$$\frac{X_{GB}}{X_{Bulk}} = \frac{1-X_{GB}}{1-X_{Bulk}} exp\left(\frac{\Delta G_{seg}}{RT}\right) \quad (3)$$

where R is the ideal gas constant, the ΔG_{seg} is the molar free energy of segregation, X_{GB} and X_{Bulk} are the average composition of GB region and bulk region respectively. Eq. (3) can be understood as the equilibrium state of exchanging bulk solute atoms with GB solvent atoms, while ΔG_{seg} generally corresponds to the free energy difference before and after the exchanging process. McLean model represents the ideal segregation behavior of solutes without considering the interactions between components, numerous attempts were made to extend the model to non-ideal cases. For binary materials, we can apply Fowler-Guggenheim surface segregation model to address the non-ideal segregation behavior of GBs:

$$\frac{X_{GB}}{X_{Bulk}} = \frac{1-X_{GB}}{1-X_{Bulk}} exp\left(\frac{\Delta G_{seg}+\alpha z X_{GB}}{RT}\right) \quad (4)$$

where z is the coordinate number and α is the parameter characterizing the strength of adsorbate-adsorbate interactions. Fowler's model is essentially a generalized McLean model , where the GB region is assumed to be a regular solution (with regular solution interaction parameter as Ω_{GB}) while the bulk region still remains ideal or in the dilute-solution limit where henry's law applies. It can be derived that $\alpha = 2\Omega_{GB}/z$. Using Fowler's model, Hondros and Seah demonstrated that GB transition can happen when the adsorbate-adsorbate interaction is strongly attractive ($-\alpha z > 4RT$), as Fig. 1.2 illustrates [41]. The GB transition obtained from the Fowler's model is similar to the phase separation of a regular solution system, which hints the physical origin of the GB transitions.

1.2.2. Multilayer GB models

The McLean type monolayer adsorption model provides a simple statistical framework to deal with the complexion adsorption and transition problems, while in realistic systems, solute segregation is not limited to the monolayer region at GBs. A more sophisticated treatment has been developed by Wynblatt, Shi, and Chatain based on a regular-solution type lattice model to consider the multilayer adsorption at metallic GBs [44, 45, 55]. The formulae of the Wynblatt-Shi-Chatain model in Refs. [45, 55] were developed for binary alloys. For a special case of a symmetric twist GB with J_{max} =1 [45, 55] (meaning that all bonds are either in the atomic plane or between the immediate adjacent planes) for simplicity. The following GB adsorption equation can be derived for binary alloys:

$$\frac{X_{GB}^{k}}{X_{Bulk}} = \frac{1-X_{GB}^{k}}{1-X_{Bulk}} exp\left(\frac{\Delta H_{seg}^{k}}{RT}\right), \quad (5)$$

where the superscript *k* represents the *k*-th GB layer, and the (molar) segregation enthalpy of the solute at the *k*-th GB layer is expressed (in a form that can be compared with the Fowler's model as described in previous section) as:

$$\Delta H_{seg}^{k} = \Delta H_{seg,(0)}^{k} - 2zN_A(X^k - X^{Bulk})\omega - 2z_v N_A(X^{k-1} - 2X^k + X^{k+1})\omega \quad (6)$$

where $\Delta H_{seg,0}^{k}$ is the intrinsic segregation enthalpy (originating from the differential bonding energies and the strain energy of solutes [45, 55]), z is the total coordination number (numbers of bonds per atom), z_v is the number of bonds between adjacent layers (so that $z = 2z_v + z_l$, where z_l is the lateral coordination number within the same atomic plane; noting that J_{max} =1 [45, 55] for this simplified case), and ω is the pair-interaction parameter (a.k.a. regular solution parameter) for the bulk solid-solution phase. Please note that $X_i^0 = X_i^1$ for the symmetrical twist GB since the 0-th layer is essentially the 1-st GB layer on the other side and the effects of "broken bonds" at the GB core are considered separately in the $\Delta H_{seg,(0)}^{k}$ term. Using this model, Wynblatt and Chatain demonstrated the existence of a GB prewetting (thin-thick adsorption) transition line [44], analogous to that shown by Cahn in his critical-point wetting model for a binary de-mixed liquid [46].

1.2.3. Diffuse interface model

The lattice type GB models are restricted only to the cases where GB transitions are dominated by GB chemistry change and the structure disordering of GBs (such as premelting transition) is omitted. To combine the structural and chemistry factors in GB thermodynamic modeling, Tang et al. [1, 2] and Mishin et

al. [48] used diffuse-interface (phase-field type) models to describe coupled GB prewetting and premelting transitions. Different from lattice type model introduced previously, diffuse-interface model treats the system as continuous matter and the discrete nature of atomic structures are omitted for simplicity. In Tang's model, a GB system is characterized by three field variables: composition (X), crystallinity (η) and misorientation (θ) and the excess free energy per unit area of the GB system can be expressed as:

$$\gamma_{GB} = \int \left[\Delta f_v(X,\eta,T) + \frac{\kappa^2}{2}\left(\frac{dX}{dx}\right)^2 + \frac{\nu^2}{2}\left(\frac{d\eta}{dx}\right)^2 \right] dx + \Delta\gamma_{core}(X,\eta) \qquad (7)$$

where Δf_v is the excess volumetric free energy with respect to a reference state set by crystalline grains (X = X_{Bulk}, η = 1), κ and ν are the free energy gradient coefficients of composition and crystallinity field respectively that can be estimated from fusion enthalpy or solid-liquid interfacial energies, the last term corresponds to the overall contribution of broken bonds and/or strain energy at the GB core, that hypothetically can be relaxed by GB adsorption and/or GB structural disordering (reduction of η). The equilibrium GB profiles can be solved by minimizing Eq. (7) with respect to by providing a certain boundary condition X_{Bulk} and T. The model successfully predicted GB transitions produced by structural disordering and segregation cooperatively within the single-phase region as Fig. 1.3 show. The modeled behaviors of GBs are generally consistent with experimental observations of GB premelting/prewetting phenomena in both ceramic and metallic systems [24, 56].

1.2.4. GB λ model

Alternatively, coupled GB disordering and adsorption can also be modeled by extending a sharp-interface phenomenological thermodynamic model that was originally developed for premelting in unary systems [57] to multicomponent alloys. In this phenomenological interfacial thermodynamic model [7, 29, 35-38], a disordered GB complexion is regarded as a confined liquid-like interfacial film as Fig. 1.4 shows, with their thermodynamic properties being modified by the presence of various interfacial interactions. The excess grand potential as a function of the effective interfacial width (*h*, which is often called “film thickness”) can be written as:

$$\sigma^{x}(h) = \Delta G_{\text{amorph}}^{(\text{vol})} \cdot h + 2\gamma_{\text{cl}} + \sigma_{\text{interfacial}}(h) \ , \tag{8}$$

where $\Delta G_{\text{amorph}}^{(\text{vol})}$ is the volumetric free energy for forming an undercooling liquid from the equilibrium solid phase(s) and γ_{cl} is the crystal-liquid interfacial energy. The interfacial potential, $\sigma_{\text{interfacial}}(h)$, represents the effects of all interfacial interactions ($\sigma_{\text{interfacial}}(+\infty) = 0$ by definition). A premelting-like GB complexion can be stabilized if the energy penalty for forming an undercooled quasi-liquid film is overcompensated by the reduction in the interfacial energy:

$$-\Delta\gamma \cdot f(h) > \Delta G_{amorph}^{(vol)} h \tag{9}$$

where

$$\Delta\gamma \equiv 2\gamma_{\text{cl}} - \sigma^{x}(0) \tag{10}$$

and $f(h)$ is a dimensionless interfacial coefficient:

$$f(h) = 1 + \sigma_{\text{interfacial}}(h) / \Delta\gamma \tag{11}$$

with the boundary conditions: $f(0) = 0$ and $f(+\infty) = 1$.

As Fig. 1.5 shows, the equilibrium thickness, h_{eq}, corresponds to the minimum of Eq. (7) with respect to h (so that $d\sigma^{x}(h)/dh\big|_{h=h_{eq}} = 0$), which is difficult to be quantified because the exact form of $f(h)$ or $\sigma_{\text{interfacial}}(h)$ is typically unknown. Thus, a thermodynamic parameter can be introduced as:

$$\lambda \equiv \frac{-\Delta\gamma}{\Delta G_{\text{amorph}}^{(\text{vol})}}, \tag{12}$$

which scales the actual interfacial width (h_{eq}) and can be quantified by combining bulk CALPHAD data with statistical interfacial thermodynamic models [7, 29, 35-38].

Subsequently, the computed lines of constant λ values can be plotted into bulk phase diagrams to represent the thermodynamic tendency for average general GBs to disorder. These GB λ diagrams can predict useful trends in GB disordering in binary and multicomponent alloys at high temperatures that have been validated by experiments [7, 29, 35-38], even if they are not rigorous GB complexion diagrams with well-defined transition lines and critical points.

1.3. Nanocrystalline alloys with stable grain sizes

Nanocrystalline metals attracts a lot of research interests due to their outstanding mechanical properties such as high strength and wear resistance [58]. However, with the presence of a large amount of grain boundaries within these nanocrystalline metals, large driving force of grain growth occurs concurrently letting the materials become vulnerable to grain coarsening at high temperature. Consequently, the mechanical properties change dramatically if grain size is increased out of the nanocrystalline regime [59]. Such instability of these materials limits the application of nanocrystalline metals at elevated temperature. Alloying has been used traditionally to oppose grain growth by reducing the GB motion through solute drag or second phase pinning. Slowing GB motion can be sufficient to stable nanocrystalline states. However, the kinetic nature of the drag mechanism generally produces transient stability for nanocrystalline states, while at high temperature, grain coarsening still can be activated because the velocity of GB generally increases exponentially with the temperature according to Arrhenius equation.

Alternatively, grain growth of nanocrystalline metals can be inhibited by reducing the excess free energy of the GB, which is the underlying cause of grain growth. It was well known by Gibbs adsorption isotherm that GB free energy can be relieved by solute adsorption. With the decrease of GB free energy, the overall tendency of grain coarsening is also reduced and the grain size stability is enhanced. If the GB adsorption can fully eliminate the GB free energy, then there is no driving force for grain coarsening and the grain size reaches a

thermodynamic equilibrium state [60], where nanocrystalline states can be retained during infinitely long time exposure to high temperature environment.

1.3.1. Thermodynamic models for nanocrystalline alloys

Weissmüller first developed a thermodynamic framework describing the equilibrium grain size states in polycrystalline materials by establishing the relationship between GB adsorption and thermodynamic stability of grain size [60, 61]. Weissmüller's model is essentially a variation of McLean GB model which has already been introduced in 1.2.1. Instead of assuming fixed GB sites as McLean model, he considered a polycrystalline system where the total number of GB sites is a variable proportional to the GB area. Then, the total system energy G^{PX} of a binary system can be written as:

$$G^{PX} = A_{GB}\gamma_{GB}^{(0)} + N_{tot}^{A}\mu_{A}^{0} + N_{tot}^{B}\mu_{B}^{0} + N_{tot}^{B}\Delta H_{mix} + N_{GB}^{B}\Delta H_{seg} + N_{bulk}^{tot}RT(X_{bulk}^{A}lnX_{bulk}^{A} + X_{bulk}^{B}lnX_{bulk}^{B}) + N_{GB}^{tot}RT(X_{GB}^{A}lnX_{GB}^{A} + X_{GB}^{B}lnX_{GB}^{B}) \quad (13)$$

where A_{GB} is the total GB area, N_{tot}^{A} and N_{tot}^{B} are the total number of A and B atoms in the system, ΔH_{mix} is the mixing energy (a.k.a. enthalpy of solution) of B in A, N_{bulk}^{tot} and N_{GB}^{tot} are the total bulk and GB sites in the system, $X_{GB}^{i} = N_{GB}^{i}/N_{GB}^{i}$ and $X_{GB}^{i} = N_{GB}^{i}/N_{GB}^{i}$ are the GB and bulk compositions of *i* = A or B component. Conservation laws impose that $\sum N_{GB}^{i}$=N_{GB}^{tot}, $\sum N_{GB}^{i}$=N_{GB}^{tot} and $N_{GB}^{tot} + N_{bulk}^{tot} = N^{tot}$ and the number of GB sites are related to GB area empirically by $N_{GB} = nA_{GB} \approx 3V/d$ where *n* is the GB sites per unit area, *V* is the volume of the system and *d* is the grain size. For a confined system, the equilibrium distribution of solutes (X_{bulk}

and X_{GB}) minimizing eq. (13) can be solved by letting $\frac{\partial G^{pX}}{\partial X_{GB}} = 0$ by providing a grain size value *d*, and by varying *d*, G^{PX} can be calculated as a function of *d*. A minimum point of G^{PX} at finite d_{eq} can be generated with certain parameter setting (e.g. strong negative ΔH_{seg}), where the system reaches an equilibrium grain size state ($\frac{\partial G^{pX}}{\partial d} \propto \gamma_{GB} = 0$) and grain coarsening (larger *d* value) is no longer thermodynamically favored. Weissmüller's theory successfully demonstrates the theoretical possibility of stabilizing polycrystalline alloys' grain sizes by fully eliminating the GB excess free energy via GB segregation. A more rigorous model, named the regular nanocrystalline solution (RNS) model, was development by Trelewicz and Schuh who used a regular solution approach to describe the solute-solvent interactions, providing a more accurate estimation of system enthalpies for high bulk concentration. The RNS model was modified and used by Murdoch et al. [62] to explore the desired parameter space where thermodynamic stable nanocrystalline states exist as well as help design binary nanocrystalline alloys. A model similar to the RNS model with consideration of third alloying component as well as the strain energy of solutes has been later developed by Saber et al [63]. As no explicit analytic expressions of GB energy as a function of bulk composition and temperature are derived, the calculation of these regular solution usually on complex numeric simulations. More quick and convenient approach of estimating solute's effect on stabilizing nanocrystalline alloys is employed by Kircheim by assuming dilute solutions and omitting the grain size dependency of segregation energy [64]. In such cases, the GB energy can be expressed as:

$$\gamma_{GB} = \gamma_{GB}^{(0)} - \Gamma\left[\Delta H_{seg} + RTlnX_{bulk}\right] \quad (14)$$

where $\gamma_{GB}^{(0)}$ is clean GB energy, $\Gamma = nX_{GB}$ is the amount of solute adsorption. As Eq. (14) describes, γ_{GB} can be reduced to zero when ΔH_{seg} and Γ are sufficiently large. Using the model and Wynblatt-Ku segregation model to estimate ΔH_{seg}, Darling calculated γ_{GB} vs. X_{GB} solute curves at a fixed annealing temperature as shown in Fig. 1.6 for doped Fe alloys. The results show that Zr can effectively reduce the γ_{GB} energy to zero, which is validated by the experiment results showing that nanocrystalline Fe can be stable at 900 ºC with Zr doping.

1.3.2. Synthesis of nanocrystalline alloys

Based on GB thermodynamic models' predictions, various binary and ternary thermal stable nanocrystalline alloys are designed and synthesized. Darling *et al.* found that the grain size of NC Fe can be stabilized smaller than 100 nm at 913 ºC for 1 hour by Zr segregation in the GBs [65, 66]. Cu-Ta (10 at.%) binary alloy can substantially retain the grain size of 200 nm after 1 hour annealing at approximately 97% of the melting point (T_m) of pure Cu [67, 68]. More recently, Rupert group found that Zr segregation in the GBs of Cu resulted in a Zr-rich intergranular film that stabilized the grain size at around 50 nm above $0.9T_m$[69]. With W segregated into the GB, the grain size for the electrodeposited Ni-W NC alloy was found to be stable up to $0.5T_m$ [70, 71]. Li *et al.* reported the stabilizing of nanograins in a ternary Fe-Zr-Hf system, in which addition of 1-4 at.% Hf resulted in more pronounced thermal stability than that of the binary Fe-Zr alloys [72]. NC Pd stabilized by Zr segregation were also reported [73].

Nanocrystalline materials can be synthesized via various ways. One way of classifying different synthesizing techniques is based on the initial state of materials' microstructures, by which two classes of techniques can be defined: the first one is ‘‘bottom-up’’ method and the second one is “top-down”. The bottom-up approach uses atoms, ions, or even nanocrystalline powders as building blocks to form a bulk material parts by assembling techniques. Conversely, top-down approaches start with a bulk material while their structure was break down into the nanoscale pieces during the processing procedure, typically by severe plastic deformation or fast cooling. The bottom-up approach includes: powder metallurgy methods, such as mechanical alloying by ball milling followed with consolidation of grinded powders or direct consolidation of nano-size powders; deposition methods such as sputter deposition, e-beam deposition and electrodeposition. Representative top-down approaches are: equal-channel angular extrusion (ECAE), high-pressure torsion and crystallization of amorphous precursors. Each method has its own advantages and limitations. In general, top-down methods can produce “bulk” nanocrystalline pieces, while they usually require extreme processing environments to achieve grain size < 100 nm such as ultra-high pressure or ultra-fast cooling rate, which bring difficulty to designing and implementing experiments. Bottom-up techniques are relatively easier to realize nanocrystalline states while the challenge of such methods is to fabricate samples with sizes large enough for proper testing (e.g. the maximum thickness of sputtered nanocrystalline films are usually limited to several micrometers).

Among bottom-up techniques, powder processing routes offers a readily scalable routine of bulk nanocrystalline materials production (e.g. near fully dense bulk nanocrystalline Cu and Al alloys made by powder metallurgy techniques have been reported). Fig. 1.7 shows a typical work flow of synthesizing bulk nanocrystalline alloys using bottom-up technique. The bottom-up techniques usually include ‘‘two-step’’ major processes: 1) creating nanostructured powders, 2) consolidating at elevated temperatures (>50% of the melting temperature, T_m). A common method used for the first step is ball milling process that involves grinding and impacting of metallic particles powders. During the milling process, the repeated impacts introduced a lot of dislocations and defects to the system by plastic deformation and fractures, causing grain refinements of the particles. In addition, mechanical alloying of different elemental powders can be realized using ball milling. Various types of mills can be used for nanocrystalline powder preparation, ranging from laboratory-scale shaker mills (e.g., SPEX 8000 mill, used in this thesis) that can produce 5–10 g of powder to commercial-scale mills that can process large volume of powder at a time. Additionally, milling machines are also often classified into low-energy or high-energy mills according to the frequency and amplitude of the vibrations of the mills. High energy ball milling is more efficiency than low-energy mills while it tends to introduce more contaminations from the milling media. The milling efficiency is also dependent on the weight ratio of ball to powder as the larger of the ratio, the higher of the efficiency. Typically, metallic powders are turned into nanocrystalline powders completely after 6 hrs high energy ball milling. In the second step, the milled

powders are consolidated into dense. Traditional consolidation method is conventional sintering, whereby particles are sintered to reduce the overall surface area of the system. Conventional sintering usually takes several hours. To reduce the sintering time and further improve the density, hot pressing and hot isostatic pressing can be used, that are typically carried out by applying a uniaxial or static pressure upon samples during heating. More recently, spark plasma sintering (SPS) technique draws a lot of research interests powder metallurgy community and becomes more and more popular. During the SPS process, an electric field passes through the sample under pressure, that results joule heating at the particle-to-particle contacts providing rapid volumetric heating within the materials.

Chapter 1, in part, is a reprint of the material "GB complexions in multicomponent alloys: Challenges and opportunities" as it appears in Current Opinion in Solid State and Materials Science, Naixie Zhou, Tao Hu, and Jian Luo, 2016, 20, 268-277. The dissertation author was the primary investigator and author of this paper. All calculations and data analysis were performed by the author.

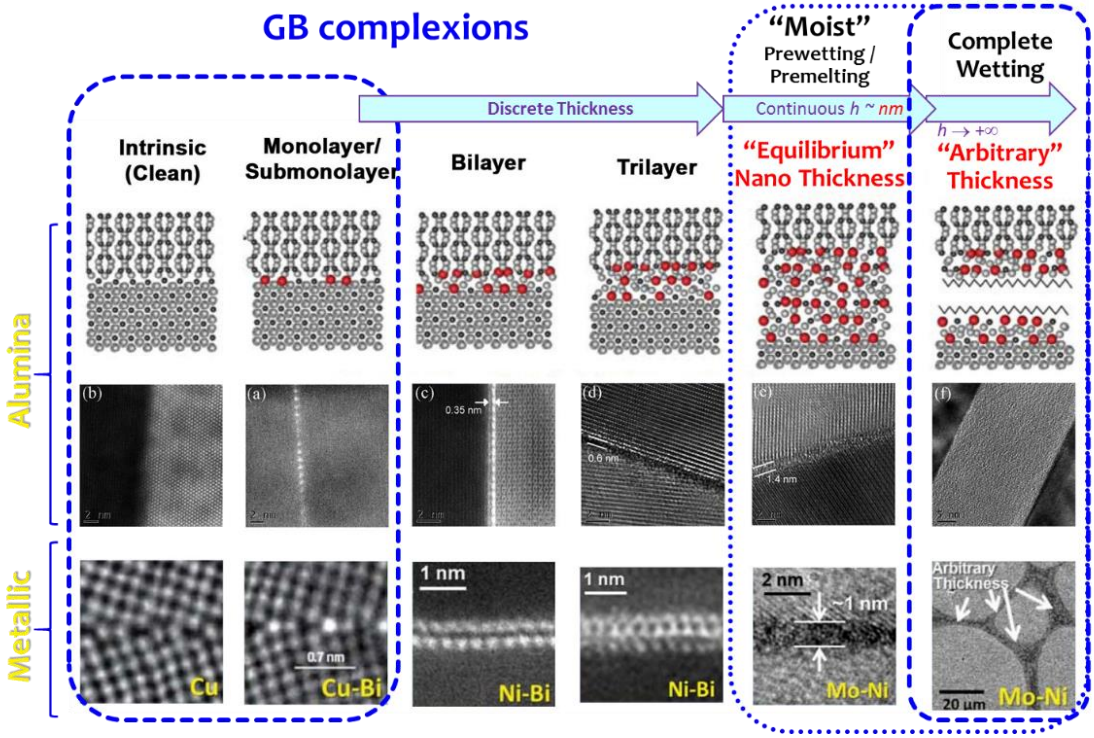

Figure 1.1 GB complexions observed in ceramic and metallic systems.

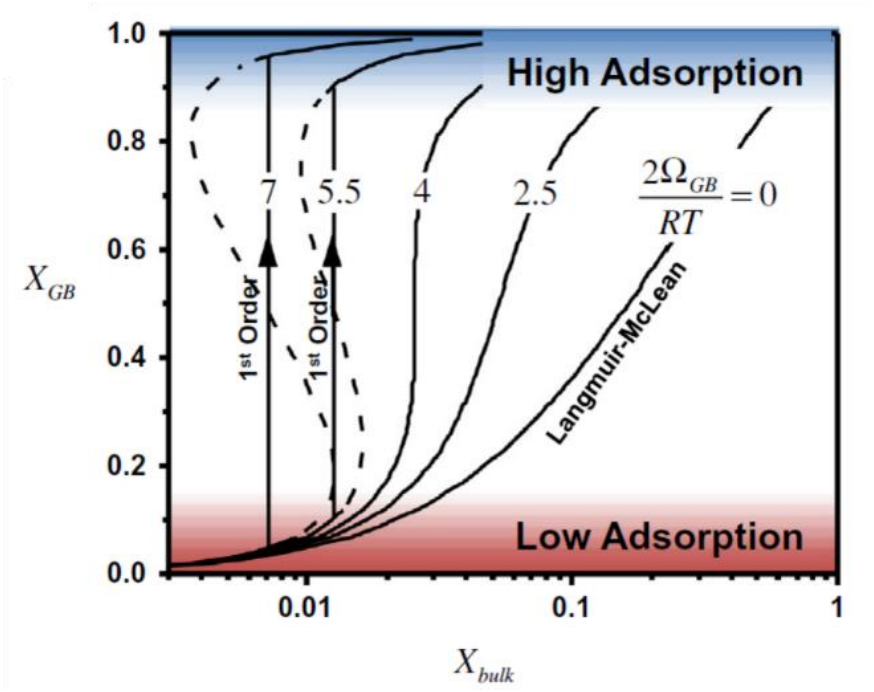

Figure 1.2 An illustration of first-order complexion transition. The complexion transition is captured by calculating GB composition as a function of bulk composition using Fowler-Guggenheim model, that corresponds to the abrupt change of GB composition on the calculated curve.

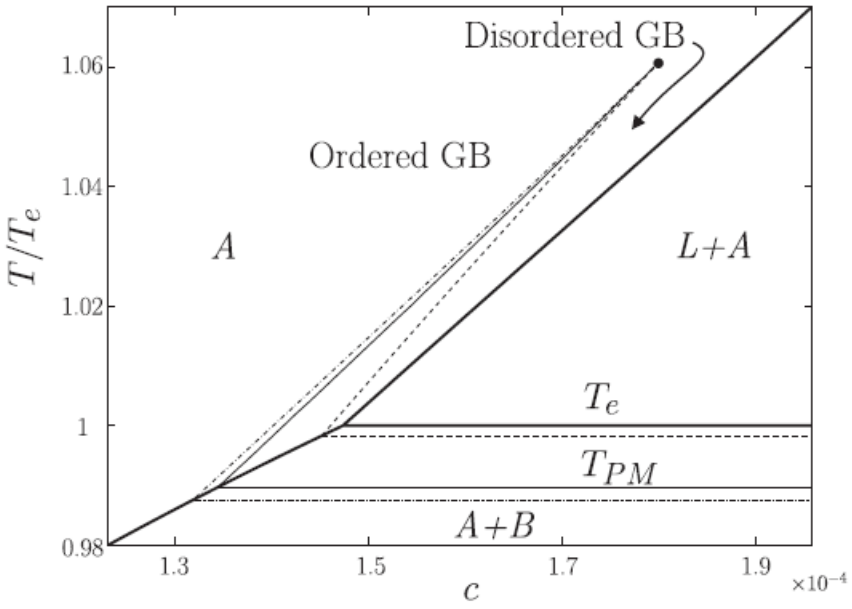

Figure 1.3 Calculated GB diagram for a binary system. The ordered–disordered GB coexistence line in single-phase region corresponds to thin solid line, the spinodal lines (i.e., limits of stability) of ordered GBs are plotted with dashed lines and disordered GBs (dashed-dotted line) are also shown. The first order transition terminates at the critical point (solid dot).

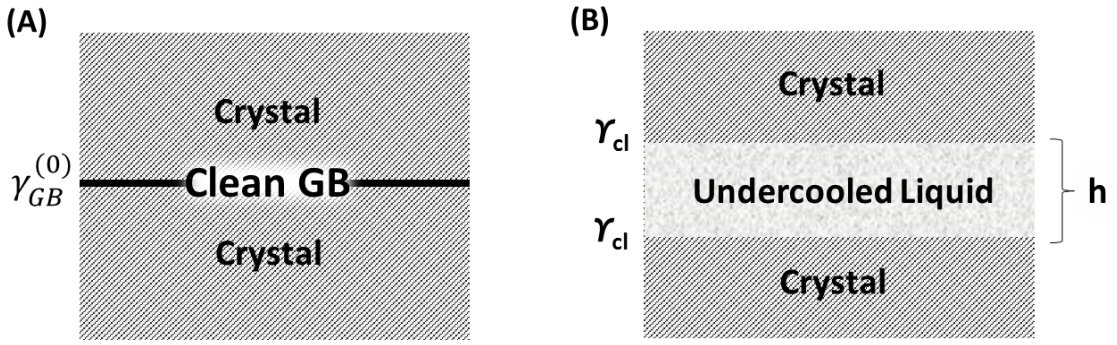

Figure 1.4 Schematics of comparison between clean GB and disordered GB. (A) is a clean GB and (B) is a disordered GB.

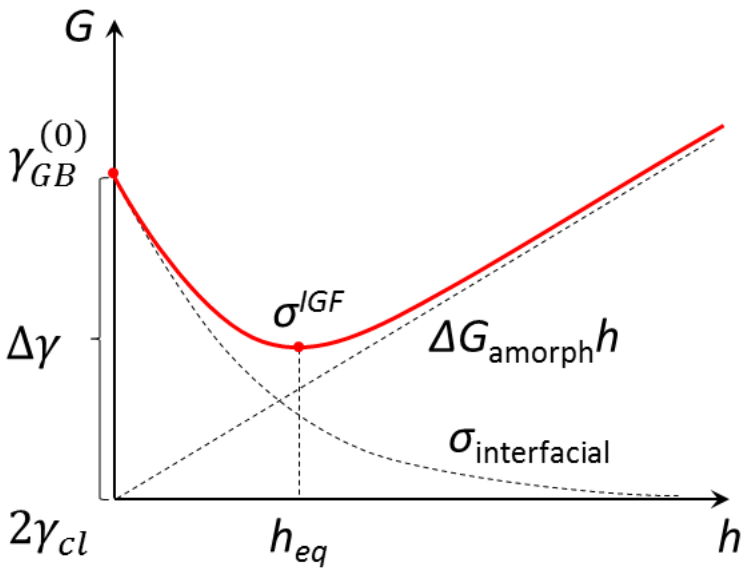

Figure 1.5 GB excess free energy curve calculated using force balance model.

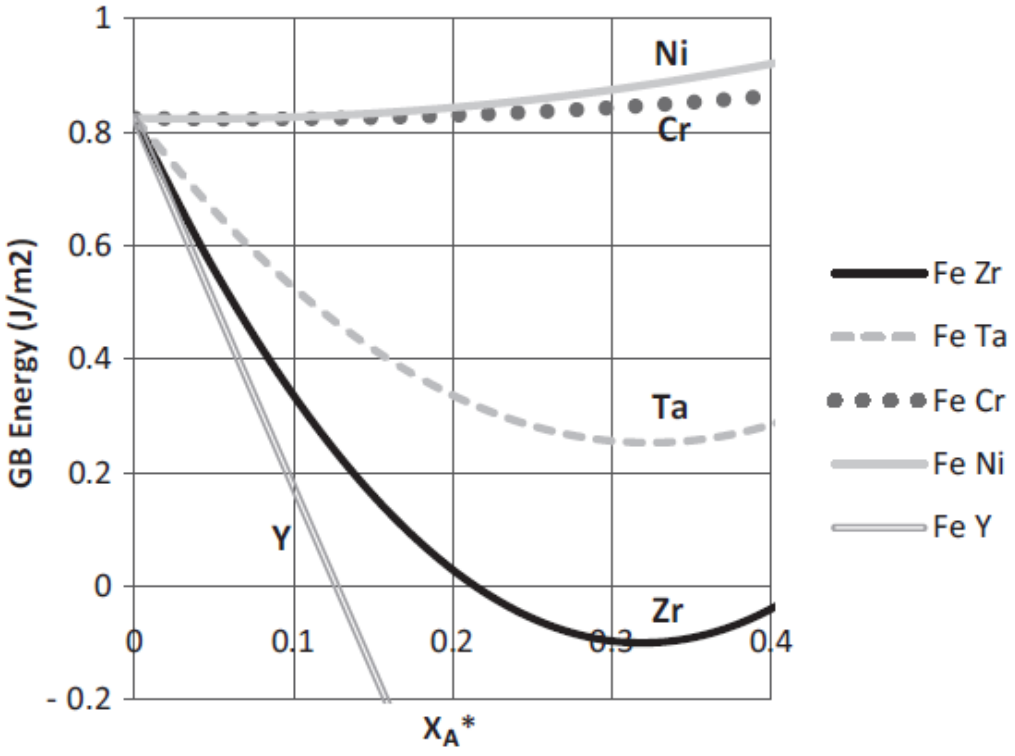

Figure 1.6 Calculated GB energy versus solute concentration for Fe system [66].

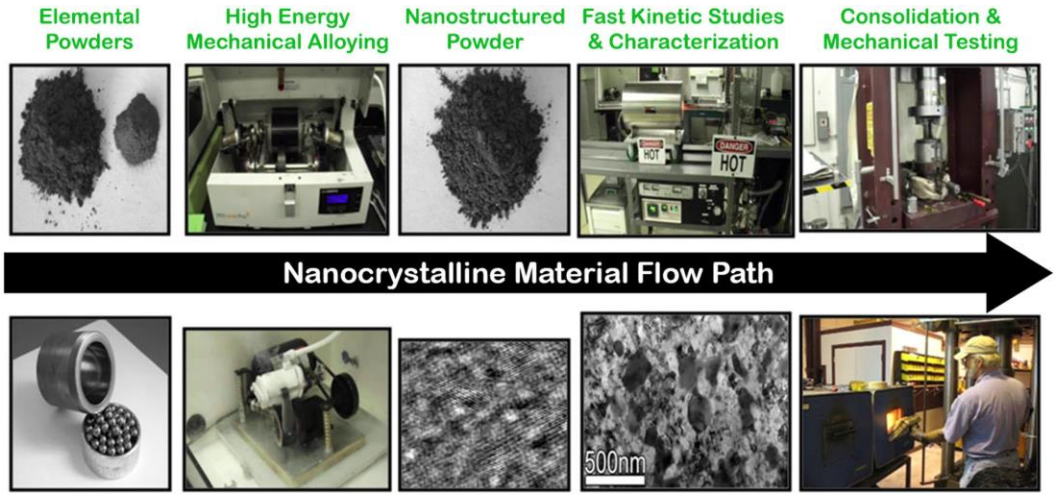

Figure 1.7 Typical flow path of synthesizing nanocrystalline alloys using powder methods[74].

Chapter 2. Developing GB Diagrams for Multicomponent Alloys

Impurity-based, premelting-like, intergranular films (IGFs) can form in various materials and influence sintering, creep, and microstructure development. A thermodynamic framework is presented to forecast the formation and stability of these premelting-like IGFs in multicomponent alloys to consider the interactions of multiple alloying elements. Key thermodynamic parameters that control the interfacial segregation and disordering behaviors have been identified and systematically examined. Subsequently, ternary and quaternary GB diagrams have been computed and used to forecast the sintering behaviors of W-Ni-M (M = Fe, Co, Cr, Zr, Nb and Ti) and Mo-Si-B-M (M = Ni, Co and Fe) systems. This work supports a long-range scientific goal of extending bulk computational thermodynamics and CALPHAD methods to interfaces and developing GB diagrams as extensions to bulk phase diagrams, which can be a generally useful materials science tool.

2.1. Introduction

The development of bulk phase diagrams and calculation of phase diagram (CALPHAD) methods established one of the foundations for modern materials science. In a series of recent studies, bulk CALPHAD methods were extended to model GBs to forecast the stability of impurity-based, premelting-like IGFs in binary alloys; subsequently, a type of GB λ diagrams have been developed to represent the thermodynamic tendency for general GBs to disorder and forecast related activated sintering behaviors in binary alloys (only) [7, 29, 36, 37]. Although they

are not yet rigorous GB “phase” (complexion) diagrams, the correctness and usefulness of these binary GB λ diagrams have been validated by a series of experiments. First, the model predictions were corroborated with direct HRTEM and GB chemistry analysis for selected systems [7-9, 36, 56]. Second, the computed GB λ diagrams (with no free parameters) correctly predicted the onset sintering temperatures for a series of W based binary alloys as well as some trends in sintering rates [7, 36, 37]. Specifically, the predicted GB solidus temperature was consistent with a prior direct GB diffusivity measurement for W-Co (the primary element/phase is underlined) using radioactive tracers [36, 75]. Third, the estimated GB diffusivity as a function of temperature and overall composition correlated well with the computed binary GB λ diagram for Mo-Ni [7]. Finally, a counterintuitive phenomenon of decreasing GB diffusivity with increasing temperature was predicted and subsequently verified experimentally in a Mo + 0.5 at. % Ni alloy [38].

Historically, bulk CALPHAD methods were first developed for binary alloys, for which phase diagrams have already been determined by experiments. CALPHAD methods become useful when they can utilize the thermodynamic data that are largely obtained from binary systems to extrapolate (by adding only a few multi-body interaction parameters) and predict behaviors of multicomponent alloys, where the Edisonian approach is no longer feasible. Likewise, such strategy can also be applied to the construction of GB diagrams for multicomponent systems. As previous studies demonstrated the basic feasibility of constructing binary GB λ

diagrams and their usefulness in predicting sintering behaviors, the challenging goal of this study is to extend and validate the model and computation methods to multicomponent ($N \geq 3$) alloys.

2.2. The model and computational methods

The GB λ model used in this Chapter is described previous in 1.2.4. λ values can be solved from Eq. (12) by knowing the interfacial energies Δγ and bulk amorphization energy ΔG_{amorph}.

2.2.1. Estimation of reference interfacial energies

The interfacial energies can be estimated by a macroscopic-atom model that was originally developed by Benedictus, Böttger, and Mittemeijer for simulating solid-state amorphization [76, 77], which utilizes the Miedema type parameters. Since we use CALPHAD data to compute bulk thermodynamic functions, here we adopt and refine a lattice model [78] that utilizes the regular-solution (pair-interaction) parameters to estimate interfacial energies to be self-consistent (as a further improvement from the prior studies [7, 29, 36, 37] that used the macroscopic-atom model, in addition to a major extension from binary to multicomponent alloys). In such a lattice model, the interfacial energy of an interface between a crystal of pure *A* (with a negligibly small solubility of *B*) and a liquid of a uniform composition of X_B^L (the molar/atomic fraction of *B*) in a binary *A*-*B* system is estimated as:

$$\gamma_{cl} \approx \gamma_{cl}^{(0)} = \frac{\Delta H_A^{\text{fuse}}}{\kappa m_1^{-1} V^{2/3}} + \frac{\Omega_{A-B}^L}{\kappa m_1^{-1} V^{2/3}} (X_B^L)^2 + \frac{1.9RT}{\kappa m_1^{-1} V^{2/3}}, \quad (15)$$

where ΔH_A^{fuse} is the fusion enthalpy of *A*, Ω_{A-B}^L is the molar liquid phase regular-solution parameter, *V* is the molar volume (neglecting the thermal expansion for simplicity), m_1 is the fraction of bonds crossing the interface, and κ is a geometric factor ($\kappa \equiv A_m / V^{2/3}$, where A_m is the area of one mole of atoms spread as a monolayer [78]). The value of κm_1^{-1} depends the crystalline orientation of the interface: for example, $\kappa m_1^{-1} \approx 5 \times 10^8$ for (100) planes for any cubic lattice and $\kappa m_1^{-1} \approx 3.7 \times 10^8$ for the close-packed (111) plane in an FCC lattice. In this study, we set $\kappa m_1^{-1} = C_0 \approx 4.5 \times 10^8$ to represent the average value (of all different crystalline orientations), which is a parameter adopted in the macroscopic-atom model [79] to represent the *average* grain surface orientation of general GBs in a polycrystal.

The first term in Eq. (15) is an enthalpic contribution that corresponds to the excess enthalpy of a crystal-liquid interface of pure *A*. The second term represents the chemical interaction, *a.k.a.* the change in the interfacial energy when the fraction of *B* in the liquid increases from zero to X_B^L, where bonds at the solid-liquid interface are assumed to be liquid type. The third term is an entropic contribution due to the near-interface ordering, which is adapted from the Benedictus-Böttger-Mittemeijer model [76, 77]. The superscript (0) is used in $\gamma_{cl}^{(0)}$ to denote that it is a reference interfacial energy without considering the near-interface variation in

composition (as an estimation of the true equilibrium γ_{cl}). The main reason to adopt this lattice model is that it uses the regular-solution parameters that can be obtained from the CALPHAD data so that the same set of parameters are used in both the bulk thermodynamic functions and the statistic interfacial thermodynamic model to compute GB λ diagrams in a self-consistent manner.

Eq. (15) can be further extended to model a multicomponent alloy, where the interfacial energy of an interface between a crystal of pure *A* (with negligible solid solubilities) and a multicomponent liquid (of composition X_i^L, *i* = A, B, C…) is estimated as:

$$\gamma_{cl} \approx \gamma_{cl}^{(0)} = \frac{1}{C_0 V^{2/3}}\left[\Delta H_1^{\text{fuse}} + \left(\sum_{i\neq A}\Omega_{i\text{-A}}^L X_i^L - \frac{1}{2}\sum_{i\neq j}\Omega_{i\text{-}j}^L X_i^L X_j^L\right) + 1.9RT\right], \tag{16}$$

where the first, second, and third terms, respectively, are again the enthalpic, chemical, and entropic contributions, respectively, and κm_1^{-1} is set to be C_0. In Eq. (10), the $\frac{1}{2}\sum_{i\neq j}\Omega_{i\text{-}j}^L X_i^L X_j^L$ term represents the reference energy state set by the chemical potential of the bulk liquid phase (noting that this term is not included for the Benedictus-Böttger-Mittemeijer model [76, 77], where the reference state is set to be the pure metals for solid state amorphization).

If the solid solubility limits are not negligibly small, Eq. (16) can be further generalized to:

$$\gamma_{cl} \approx \gamma_{cl}^{(0)} = \frac{1}{C_0 V^{2/3}} \left[\sum_i X_i^C \left(\Delta H_i^{fuse} + \sum_{i \neq j} X_j^L \Omega_{i-j}^L \right) - \frac{1}{2} \left(\sum_{i \neq j} X_i^L X_j^L \Omega_{i-j}^L + \sum_{i \neq j} X_i^C X_j^C \Omega_{i-j}^C \right) + 1.9RT \right] \quad (17)$$

where the superscripts “C” and “L” are used to represent the crystal and liquid phases, respectively. Eq. (17) can be reduced to Eq. (16) if $X_A^C \approx 1$ and $X_i^C << 1$ for all $i \neq$ A, which are the cases for most of our examples discussed below.

To calculate the reference interfacial energy change $\Delta\gamma$ from Eq. (12), we also need to know the GB energy for a “dry” boundary (without any adsorption and disordering). If the solid solubility limits of all alloying elements are small, the measured GB energy of for the average general boundaries is typically used and the Turnbull estimation, $\gamma_{\mathrm{GB}}^{(0)} \approx \frac{1}{3}\gamma_{\mathrm{Surface}}^{(0)} \approx \frac{1}{3}\Delta H^{\mathrm{vaporization}} / (C_0 V^{2/3})$, can be used in the cases where the experiment data are not available. If the solid solubility limits of alloying elements are not negligibly small, the “dry” GB energy of an alloy can be expressed as:

$$\gamma_{GB}^{(0)} \approx \sum_i X_i^C \gamma_{GB,i}^{(0)} + \frac{Q}{C_0 V^{2/3}} \sum_{i \neq j} X_i^C X_j^C \Omega_{i-j}^C , \quad (18)$$

where Q is the average broken bond fraction, which is typically set to 1/6 for an average general GB to satisfy the Turnbull estimation. In most case studies of W and Mo based alloys presented in this paper, the solid solubility limits are small so that Eq. (18) and experimentally measured GB energy of the average general boundaries can be used to estimate $\Delta\gamma$.

2.2.2. Evaluating the volumetric free-Energy penalty for forming an undercooled liquid

Bulk CALPHAD data (thermodynamic functions) and methods are used to evaluate the volumetric free energy penalty for forming an undercooled liquid, $\Delta G_{\text{amorph}}^{(\text{vol})}$. The free energy of a phase Φ in a multicomponent system can be expressed as:

$$G^{\Phi} = \sum_i X_i^{\Phi}\, {}^0G_i^{\Phi} + RT\sum_i X_i^{\Phi} \ln X_i^{\Phi} + {}^{XS}G^{\Phi} , \tag{19}$$

where X_i^{Φ} and ${}^0G_i^{\Phi}$, respectively, are the fraction and the free energy, respectively, of the component *i*. ${}^{XS}G^{\Phi}$ is the excess free energy of mixing, which can be expressed in a Redlich-Kister polynomial:

$${}^{XS}G^{\Phi} = \sum_m \sum_{i\neq j} L_{m(i,j)}^{\Phi} X_i^{\Phi} X_j^{\Phi} (X_i^{\Phi} - X_j^{\Phi})^m . \tag{20}$$

Here, $L_{m(i,j)}^{\Phi}$ is the m-th order interaction parameter between the components *i* and *j* in the phase *Φ*. Specifically, $L_{0(i,j)}^{\Phi}$ is the regular solution parameter ω_{i-j}^{Φ} and this polynomial is reduced to a regular-solution equation for the zero-th order expansion (*m* = 0 only). The molar free-energy penalty for forming an undercooled liquid (film) of composition $\mathbf{X}_{film}^{L} = \{X_i^{L}, i = A, B, C...\}$ can be written as:

$$\Delta G_{\text{amorph}}^{(\text{mol})} = G^{\text{L}}(\mathbf{X}_{film}^{L}) - \sum_i \mu_i^{C} X_i^{\text{L}} . \tag{21}$$

The first term in Eq. (21) is the molar free energy of the bulk liquid phase. It is important to note that partial order and compositional gradients generally exist in the nanoscale quasi-liquid IGF so that it is not perfect liquid; however, λ can be defined and calculated based on *a reference state* of uniform and perfect liquid film, while the variations in free energies due to order and compositional gradients can be (at least partially) considered in the interfacial potential term in Eq. (8); this approach was elaborated in a prior review [6]. The second term in Eq. (21) represents the reference free-energy state set by the chemical potentials (μ_i^C) of the bulk phase (crystalline grains) of a given composition $\mathbf{X}_{bulk}^C = \{X_i^C, i = A, B, C...\}$:

$$\sum_i \mu_i^C X_i^{\mathrm{L}} = G^{\mathrm{C}}(\mathbf{X}_{bulk}^C) + \sum_{i \neq A} \frac{\partial G^{\mathrm{C}}}{\partial X_i}(X_i^{\mathrm{L}} - X_{0,i}^C) \tag{22}$$

As illustrated in Fig. 2.1, $\Delta G_{\mathrm{amorph}}^{(\mathrm{mol})}$ is represented by the distance between the liquid free-energy surface and the bulk chemical potential plane at the composition of $\mathbf{X}_{film}^L$ in a ternary system. Then, the volumetric free-energy penalty for forming an undercooled liquid is given by:

$$\Delta G_{\mathrm{amorph}}^{(\mathrm{vol})} = \frac{\Delta G_{\mathrm{amorph}}^{(\mathrm{mol})}}{\sum_i X_i^{\mathrm{L}} V_i}\,. \tag{23}$$

Finally, Eq. (23) can be re-written for a multicomponent alloy as:

$$\lambda(\mathbf{X}_{bulk}^C) = \underset{\{\text{all possible } \mathbf{X}_{film}^L\}}{\mathrm{Max}} \left\{ \frac{-\left[2\gamma_{cl}(\mathbf{X}_{film}^L, \mathbf{X}_{bulk}^C) - \gamma_{GB}^{(0)}(\mathbf{X}_{bulk}^C)\right]}{\Delta G_{\mathrm{amorph}}^{(\mathrm{vol})}(\mathbf{X}_{film}^L, \mathbf{X}_{bulk}^C)} \right\} \tag{24}$$

Subsequently, λ can be computed as a function of the bulk composition ($\mathbf{X}_{bulk}^{C}$) and lines of constant λ can be plotted in a bulk phase diagram to construct a GB λ diagram.

2.3. Evaluating the volumetric free-energy penalty for forming an undercooled liquid

2.3.1. Ternary λ diagram for average general GBs

First, we use W-Ni-Fe (*a.k.a.* Ni and Fe co-doped/co-alloyed W, where the average, general GBs of the W primary phase are represented in the computed λ diagram) as an example to demonstrate how to construct a ternary GB λ diagram with multiple phases, including the secondary crystalline precipitates. Fig. 2.2(a) and (b) schematically illustrate a two-step procedure of constructing an isothermal section of a ternary GB λ diagram. First, we computed $\lambda(\mathbf{X}_{bulk}^{BCC})$ as a function of bulk composition ($\mathbf{X}_{bulk}^{BCC} = \{X_{W}^{BCC}, X_{Ni}^{BCC}, X_{Fe}^{BCC}\}$; noting that in this case the primary crystal phase is the W-rich body-centered cubic or BCC phase so we substitute "C" with "BCC") using Eq. (24) and the bulk thermodynamic functions developed in Ref. [80, 81] at a constant temperature of 1673 K. The film composition $\mathbf{X}_{film}^{L}$ adopts the value which maximizes λ according to eq. (24). Subsequently, we plotted the computed λ values (represented by the color) in the composition space of the W-Ni-Fe ternary system (for the W-rich corner) in Fig. 2.2(a), where we also plotted lines of constant λ values. In this W-rich corner, λ values increase monotonically

with increasing Ni and Fe compositions, indicating that both Ni and Fe promote GB disorder.

In the second step, we considered the precipitation of secondary crystalline phases, such as the Ni-rich FCC phase and the μ-FeW compound in this specific case, which limit the chemical potentials of Ni and Fe. Then λ values and $\mathbf{X}_{film}^{L}$s are determined by the chemical potentials of the bulk FCC phase which are pinned by the solubility limit within the multi-phase equilibrium region. Thus, in a ternary system, the λ values and $\mathbf{X}_{film}^{L}$s should be constant along the tie lines in any two-phase region, identical to the values at the solid solubility limit (solvus or solidus) line of the BCC alloy. Moreover, the λ value and $\mathbf{X}_{film}^{L}$ are constant throughout a three-phase coexistent region in a ternary alloy. Subsequently, the bulk phase boundaries and tie lines in two-phase regions (BCC + FCC and BCC + μ-FeW, respectively, in this specific case) were calculated for the W-Ni-Fe system using bulk CALPHAD methods to construct the equilibrium ternary GB λ diagram with all equilibrium bulk phases, which is shown in Fig. 2.2(b).

2.3.2. GB-to-GB variations

We emphasize that computed GB λ diagrams represent the *average* behaviors of *general GBs* and recognize significant GB-to-GB variations in polycrystalline alloys because GBs have five macroscopic degrees of freedom. Such GB-to-GB variations may be modeled by assuming the initial $\gamma_{\mathrm{GB}}^{(0)}$ can vary by approximately $\pm$ 15% due to the anisotropy (which is typically for the general GBs

for most metals). Fig. 2.3(b) shows a computed GB λ diagram for W-Ni-Fe that considers GB-to-GB variations, where the lines of constant λ (in Fig. 2.3(a)) expand to bands (in Fig. 2.3(b)); noting that these bands are only to represent the variations in general GBs, while the special low-energy GBs are not represented here. Such GB-to-GB variations may be a root cause for abnormal grain growth, as hypothesized in a series of prior studies by Harmer and co-workers [25-27], and our calculations support and quantitatively rationalize this hypothesis. Although the lines of constant λ should always be bands for any polycrystal, we typically only plot GB λ diagrams that reflect *the average general GBs* to ensure the clarity of the diagram. It is important to recognize that GB-to-GB variations similar to that shown in Fig. 2.3(b) ubiquitously exist in all W and Mo based GB λ diagrams computed in this paper.

2.4. Effects of adding co-Alloying elements on GB disorder in ternary systems

Following earlier experimental and modeling studies of the binary W-Ni [9, 10, 36, 37] and Mo-Ni [7, 8, 38] alloys, we first conducted numerical experiments of W-Ni-*X* and Mo-Ni-*X* alloys (with *X* being a fictive element) to identify the key thermodynamic parameters that influence co-alloying effects. Specifically, we systematically varied five key parameters, *i.e.*, the melting temperature of *X* (T_X^m) and four regular-solution parameters ($\Omega_{X-A}^{\mathrm{L}}$, $\Omega_{X-A}^{\mathrm{BCC}}$, $\Omega_{X-\mathrm{Ni}}^{\mathrm{L}}$, $\Omega_{X-\mathrm{Ni}}^{\mathrm{BCC}}$, where *A* = W or Mo, assuming that *X* forms regular solutions with W, Mo and Ni in both solid and liquid phases). To focus on investigating the effects of these key parameters, a

few simplifications were adopted. We assumed the fusion entropy of *X* (ΔS_X^{fuse}) to be10 J/mol·K and its molar volume (V_X) to be 8 cm^3/mol (both are typical values for transition metals). Moreover, we only considered the BCC and liquid phases in these calculations (while the precipitation of other phase(s) was considered in examples of real alloys in the next two sections).

Prior studies had already demonstrated the formation of 0.80 ± 0.12 nm thick Ni-enriched quasi-liquid IGFs in Mo + 1% Ni specimens at 1668 K (*vs.* the computed λ = 0.99 nm) [7, 8]. In the first numerical example, we analyzed the effect of adding *X* in Mo-Ni-*X* assuming that $\Omega_{X-\mathrm{Mo}}^{\mathrm{BCC}}$ = ± 25 kJ/mol, $\Omega_{X-\mathrm{Mo}}^{\mathrm{L}} = \Omega_{X-\mathrm{Ni}}^{\mathrm{L}} = \Omega_{X-\mathrm{Ni}}^{\mathrm{BCC}}$ = 0 and T_X^m = 2000 K and using the Mo-Ni binary CALPHAD data from Ref. [82]. The computed GB λ diagrams shown in Fig. 2.4 suggest that a positive regular-solution (pair-interaction) parameter ($\Omega_{X-\mathrm{Mo}}^{\mathrm{BCC}}$) with Mo in the solid phase promotes GB disorder (by rejecting *X* into the IGFs, as evident in the film compositional map in Fig. 2.4). In comparison, a negative $\Omega_{X-\mathrm{Mo}}^{\mathrm{BCC}}$ slightly inhibits GB disorder; the corresponding film compositional map shows that *X* does not segregate to GBs/IGFs appreciably. It is interesting to note that in the W-Ni-Fe example shown in Fig. 2.2, co-alloying of Fe also enhances GB disordering in W-Ni systems as a result of a positive $\Omega_{\mathrm{Fe}-\mathrm{W}}^{\mathrm{BCC}}$ (= 41.5 kJ/mol, while all other Ω's are small; see Table I for all relevant parameters; the same effect was also evident in Fig. 2.8 for a lower temperature, where the co-alloying effect was confirmed by sintering experiments).We believe that this represents one general co-alloying effect in ternary systems.

Furthermore, we conducted a series of systematic numerical experiments of W-Ni-*X* systems, where the stabilization of subeutectic quasi-liquid IGFs in the W-Ni system had been confirmed experimentally (Fig. 2.2(e)) [9, 10]. In these calculations, we adopted $\gamma_{\mathrm{GB}}^{(0)}$ = 1.08 J/m^2 using the experimental data reported in Ref. [83] and used the W-Ni binary thermodynamic functions developed in Ref. [81]. Then, we examined the effects of five key parameters (T_X^m, $\Omega_{X-\mathrm{W}}^{\mathrm{BCC}}$, $\Omega_{X-\mathrm{W}}^{\mathrm{L}}$, $\Omega_{X-\mathrm{Ni}}^{\mathrm{BCC}}$ and $\Omega_{X-\mathrm{Ni}}^{\mathrm{L}}$; typical Ω values for W based systems are shown in Table 2.1) via a systematical approach.

First, we investigated the effect of the melting temperature of the co-alloying element *X*, where we set the four regular-solution parameters ($\Omega_{X-\mathrm{W}}^{\mathrm{BCC}}$, $\Omega_{X-\mathrm{W}}^{\mathrm{L}}$, $\Omega_{X-\mathrm{Ni}}^{\mathrm{BCC}}$ and $\Omega_{X-\mathrm{Ni}}^{\mathrm{L}}$) to be zero for simplicity. Intuitively, one might speculate that adding co-alloying element *X* with a low melting temperature will promote disordering of W GBs due to two reasons: for *X* with lower melting point, 1) the amorphization energy of pure *X* should smaller by ${}^0G_X^{\mathrm{L}} - {}^0G_X^{\mathrm{BCC}} = (T_M^X - T)\Delta S_X^{fuse}$; 2) a lower solid-liquid interfacial energy is expected due to a smaller fusion enthalpy term $\Delta H_X^{fuse} = T_M^X \Delta S_X^{fuse}$ in eq. (13). However, the computed λ diagrams shown in Fig. 2.5 suggest that reducing the melting temperature of *X* has little effects on promoting GB disordering in the W-rich BCC phase.

Second, we varied one of the four regular-solution parameters ($\Omega_{X-\mathrm{W}}^{\mathrm{BCC}}$, $\Omega_{X-\mathrm{W}}^{\mathrm{L}}$, $\Omega_{X-\mathrm{Ni}}^{\mathrm{BCC}}$ and $\Omega_{X-\mathrm{Ni}}^{\mathrm{L}}$, respectively), where we set T_m^X to be 2000 K and the three other Ω's to be zero. Fig. 6(a) and 6(b) show that a positive $\Omega_{X-\mathrm{W}}^{\mathrm{BCC}}$ or negative

$\Omega^{\mathrm{L}}_{X-\mathrm{W}}$ promotes the GB disordering in W and a negative $\Omega^{\mathrm{BCC}}_{X-\mathrm{W}}$ or positive $\Omega^{\mathrm{L}}_{X-\mathrm{W}}$ suppresses GB disordering. This can be understood intuitively since a positive $\Omega^{\mathrm{BCC}}_{X-\mathrm{W}}$ should reject *X* from the crystalline BCC phase, while a negative $\Omega^{\mathrm{L}}_{X-\mathrm{W}}$ should attract *X* to GBs to form a liquid-like complexion (or a bulk secondary liquid phase above the solidus line when a sufficiently high fraction of *X* is added). Since it is known that Ni segregates at GBs, which leads to the formation of liquid-like IGFs at high temperatures (but below the bulk solidus line), a negative $\Omega^{\mathrm{L}}_{X-\mathrm{Ni}}$ should promote GB disordering via attracting *X* to the liquid-like GB structures to thicken the effective interfacial width (Fig. 2.6(d1)). Finally, while adding *X* with a negative $\Omega^{\mathrm{BCC}}_{X-\mathrm{Ni}}$ does suppress GB disordering (Fig. 2.6(c1)), a positive $\Omega^{\mathrm{BCC}}_{X-\mathrm{Ni}}$ does not appreciably enhance GB disordering as the case of positive $\Omega^{\mathrm{BCC}}_{X-\mathrm{W}}$ (as shown in Fig. 2.6(c4) vs. Fig. 2.6(a4)). This is presumably because the Ni content in the bulk phase is low, so that a positive $\Omega^{\mathrm{BCC}}_{X-\mathrm{Ni}}$ cannot effectively reject *X* into GBs in the case of a positive $\Omega^{\mathrm{BCC}}_{X-\mathrm{W}}$). In summary, this set of numerical experiments (Fig. 2.6) suggest interesting GB adsorption and disordering behaviors that can be understood via the interactions of two co-alloying elements (Ni and *X*) the primary metal (W) and we should be able to generalize these understandings to other ternary alloys.

In general, the regular-solution parameters of the solid and liquid phases are not independent to each other; they are positively correlated and the regular-solution parameter of the corresponding solid is typically greater due to the additional strain energy in the solid phase (see typical values in Table 2.1). Thus,

in the last set of numerical experiments, we assumed ($\Omega^{BCC}_{W\text{-}X}$ - $\Omega^{L}_{W\text{-}X}$) = 50 kJ/mol (a mediate value) and varied $\Omega^{L}_{W\text{-}X}$ ($\Omega^{BCC}_{W\text{-}X}$). As shown in Fig. 2.7, addition of *X* with a greater (coupled solid/liquid) regular-solution parameter promotes GB disordering, which represents another general co-alloying effect.

2.5. Application to W-Ni-M (M = Fe, Co, Cr, Zr, Nb and Ti) ternary systems

We further modeled W-Ni-*M* (*M* = Fe, Co, Cr, Zr, Nb, Ti) ternary systems. These real ternary alloys are generally more complex because the bulk crystal/liquid solutions are not just symmetrical regular solutions (with non-zero order terms in the Redlich-Kister polynomials) and various intermediate compounds can precipitate and change the bulk phase equilibria. We considered these effects via conducting full CALPHAD analyses of the bulk phases.

We followed earlier studies [7, 29, 36, 38] to use activated sintering experiments as an efficient way to test computed results (with the underlying assumption that the enhanced sintering rates are correlated with the GB structural disorder represented by computed λ values, which has been proven in prior studies [7, 29, 36, 38]). Specifically, specimens of W, W-0.5Ni, W-1Ni and W-0.5Ni-0.5*M* (at. %) were made by mixing high-purity tungsten (99.999%, ~ 5 μm particle size) powder and metal chlorides (purchased from Alfa Aesar) in acetone solutions. Slurries were dried in an oven at 353 K (80 °C) and calcined and reduced at 873 K for an hour in a tube furnace a flowing Ar + 5% H_2 gas. The dried powders were then pressed into discs and pre-sintered at 1173 K for 2 hours in a flowing Ar + 5% H_2 gas. After measuring the initial density (ρ_0), the pre-sintered specimens

were sintered isothermally at 1573 K for two hours in a flowing Ar + 5% H_2 gas. The sintering experiments were conducted using a specially-designed vertical furnace where the specimens could be inserted into or withdrawn from the hot zone within ~ 1 minute so that the densification during ramping and cooling stages can be neglected [7]. The density of the sintered sample (ρ) was measured to calculate the density increase percentage, (ρ - ρ_0)/ρ. The mean values measured from multiple specimens sintered at identical conditions were reported and the standard deviations were used as the error bars.

Fig. 2.8(a) shows the average density increase percentages for three compositions, pure W, W-0.5Ni and W-0.5Ni-0.5Fe (at. %), that were sintered at 1573 K for two hours. Addition of 0.5 at. % of Ni substantially increased the densification of W, which was attributed to the enhanced mass transport in the subeutectic quasiliquid IGFs by both modeling and experimental studies [9, 10, 36, 37], and such Ni-based disordered IGFs have been directly observed by HRTEM (Fig. 2(e)) [9, 10]. As shown in Fig. 2.8(a), adding 0.5 at. % of Fe together with 0.5 at. % of Ni further enhanced sintering. To explain this co-alloying effect, a ternary W-Ni-Fe GB λ diagram was computed and shown in Fig. 2.8(b), where the three relevant composition points are labeled. Fig. 2.8(b) suggests that co-allying of Fe can promote GB disordering, which is consistent with experimental observations (Fig. 2.8(a)). The relevant regular-solution parameters of W-Ni-Fe are shown in Table 2.1 ($\Omega_{X-\mathrm{W}}^{\mathrm{BCC}}$ = 41.5 kJ/mol and the other three are all small); this case is close to the case shown in Fig. 2.6(a4). Thus, the enhancement effect is likely due to the

large, positive $\Omega_{X-\mathrm{W}}^{\mathrm{BCC}}$, but the current case is more complex (than that shown in Fig. 2.8(a)) due to the formation of secondary FCC phase (which was represented in Fig. 2.6) and the W-Fe binary solutions are more complex than simple regular solutions (with high-order, asymmetrical terms in the Redlich-Kister polynomials).

Furthermore, we systematically computed ternary GB λ diagrams for W-Ni-*M* (*M* = Cr, Zr, Co, Fe, Nb and Ti) systems at 1573 K using the CALPHAD data from Refs. [80, 81, 84-91], where ternary compounds were represented whenever the relevant data exist; otherwise, the ternary systems were built by combining two binary systems. First, the computed ternary GB λ diagrams with only the BCC and liquid phases (without considering the precipitation of any secondary crystalline phase) are shown in Fig. 2.9(a). Second, the computed ternary GB λ diagrams considering all possible phases (or all phases with known thermodynamic data) are shown in Fig. 2.9(b). Finally, Fig. 2.9(c) shows the measured density increases after 2-hour isothermal sintering of various ternary W-0.5Ni-0.5*M* (at. %) alloys, along with binary W-0.5Ni and W-1Ni (at. %) alloys as the references; the measured densifications for these systems generally correlate with calculated λ values with the exception of W-0.5Ni-0.5Zr (which will be explained separately). In fact, adding Nb and Ti likely enhanced the densification via liquid phase sintering since the compositions appeared to be above the solidus lines. Fe is the most effective solid-state co sintering aid, where the enhancement was likely due to the large, positive $\Omega_{X-\mathrm{W}}^{\mathrm{BCC}}$ (as we have discussed earlier). The computed results

predicted Co and Cr to be less effective co sintering aids, consistent with experimental observations.

It is interesting to note that adding Zr decreased the sintering rate in W-0.5Ni-0.5Zr, as compared with W-0.5Ni and W-1Ni, although the computed λ values suggest a small enhancement effect after adding Zr (at the thermodynamic equilibrium with the FCC and ZrW_2 precipitation; Fig. 2.9(b2)). However, the computed GB λ diagram for W-Ni-Zr without the FCC and ZrW_2 precipitation (Fig. 9(a2)) did suggest that adding Zr could suppress GB disordering if the precipitation was hindered, which offers a possible explanation for this exception. We note that Zr is prone to oxidation, which may be an alternative reason for Zr to suppress activated sintering.

2.6. Applications to Mo-Si-B-M (M = Fe, Co and Ni) quaternary systems

As the final application example, we used our model and computed GB λ diagrams to select sintering aids to enhance the densification of Mo-Si-B based alloys. A prior experimental study reported the effects of various sintering aids on enhancing the densification of Mo-8.9Si-7.7Bi (at. %) three-phase alloys, which contain the Mo-rich BCC, A15 (Mo_3Si) and T2 (Mo_5SiB_2) phases [92]. Cochran and co-workers originally introduced a reactive sintering method to sinter Mo-Si-B alloys [93]. Jung *et al.* found that adding 0.5 at. % of Ni, Co and Fe can further enhance the densification (Fig. 2.10(a)), and the effectiveness was ranked as: Ni > Co > Fe [92]. At that time, the methods to compute ternary and quaternary GB λ diagrams had not been developed, so that the experimental results were explained

based on binary interactions on a qualitative basis in Ref. [92]. Here, we computed the relevant ternary and quaternary GB λ diagrams to further explain the effects of these sintering aids on a more quantitative basis.

First, we computed a ternary GB λ diagram for Mo-Si-B at 1873K (the sintering temperature), where we used CALPHAD data of the Mo-Si-B ternary system reported in Ref. [94-96] and estimated average general GB energy ($\gamma_{GB}^{(0)}$) for pure Mo to be 1 J/m^2 using the Turnbull estimation [83]. As shown in Fig. 2.10(b), the GBs in Mo-Si-B are highly "dry;" the computed λ value generally increases with increase fraction of Si and reaches a maximum at $\lambda \approx 0.55$ nm in the Mo-A15-T_2 three-phase region. It should be noted that the computed λ value in this three-phase region represents the average Mo general GBs in Mo-8.9Si-7.7Bi, because the chemical potentials in the three-phase region are constant regardless the phase fractions. This result is consistent with the general understanding that Mo-Si-B alloy is difficult to sinter at this temperature [97] (and the reactive sintering route [93] has to be used to achieve >90% of the theoretical density (Fig. 2.10(a) and (f))).

Subsequently, we computed pseudo-ternary sections of the GB λ diagrams for the Mo-Si-B-0.5*M* (*M* = Ni, Co and Fe) systems at 1873K and a fixed atomic fraction of 0.5 % *M*, by combining the Mo-Si-B ternary CALPHAD data [94] with Mo-*M*, *M*-Si, *M*-B binary thermodynamic functions adopted from Refs.[82, 98-104]. Here, we adopted two simplifications, as follows: (1) *M* has negligible solubility in T_2 or A15 phase and (2) no *M*-containing ternary or quaternary compounds

precipitates in the composition region (up to 0.5 at. % *M*). The computed pseudo-ternary sections of the GB λ diagrams for Mo-Si-B-0.5Ni, Mo-Si-B-0.5Co, and Mo-Si-B-0.5Fe GB are shown in Fig. 2.10(c-e). It can be found that the computed λ values increased significantly (reaching λ > 2 nm in the Mo-A15-T_2 three-phase region, which corresponds to the chemical potentials of Mo GBs during the sintering) after adding 0.5 at. % Ni. Adding 0.5 at. % Co also increased the computed λ values to reach > 1 nm in the Mo-A15-T_2 three-phase region, while adding 0.5 at. % Fe increased the computed λ values moderately. Thus, the computed λ diagrams can correctly predict the relative effectiveness of these three sintering aids (Ni > Co > Fe). With the best sintering aid Ni, the densification could be substantially improved after sintering at 1873 K for 12 hour to reach ~97% of the theoretical density (Fig. 2.10 (g)), which represents the highest sintered density achieved for this alloy. It should be noted that nanometer-thick, impurity-based, disordered (quasi-liquid) IGFs have been directly observed by HRTEM in sintered Mo-Si-Ni alloys in the prior study [92], suggesting that enhanced densification is due to increased transport in these quasi-liquid IGFs.

2.7. Conclusion

A quantitative interfacial thermodynamic model has been developed for computing GB λ diagrams for ternary and quaternary alloys to forecast useful trends in GB disordering and related sintering (and potentially a wide range of other GB-controlled) properties. Numerical experiments have been conducted for Mo-Ni-*X* and W-Ni-*X* systems to identify the key thermodynamic parameters that

control the GB disordering behaviors. Subsequently, the model and computation methods have been applied to W-Ni-*M* (*M* = Fe, Nb, Ti, Cr, Zr and Co) and Mo-Si-B-*M* (*M* = Ni, Co and Fe) systems. It has been demonstrated that the computed GB λ diagrams can predict some useful trends in the relative effectiveness of various sintering aids.

In addition to the derivation and validation of the model for $N \geq 3$ systems, a further contribution of the current work is the derivation of a set of equations to use CALPHAD-derived data to estimate interfacial energies, which represent a more consistent and accurate approach than those used in prior studies of binary alloys [7, 29, 36, 37], where the same set of CALPHAD based parameters can be used in both bulk and interfacial thermodynamic computations is a self-consistent manner.

In general, it is important to develop GB diagrams for multicomponent alloys, where the Edisonian approach is no longer valid to select the optimal combination of multiple alloying elements. Practically, multicomponent GB λ diagrams can be used to understand the interactions of multiple alloying elements at GBs, thereby developing co-alloying strategies to control GBs. It should be emphasized that GB λ diagrams are not yet rigorous GB “phase” (complexion) diagrams with well-defined transition lines/curves. Nonetheless, multicomponent GB λ diagrams can be used to forecast some useful trends in GB segregation and disordering, representing an important step towards a long-range scientific goal of developing interfacial “phase” diagrams as a general materials science tool, which can be

used to help accelerating materials design, as well as achieving predictive fabrication by design, in the spirit of the Materials Genome Initiative [3, 29, 37].

Chapter 2, in part, is a reprint of the material "Developing GB diagrams for multicomponent alloys" as it appears in Acta Materialia, Naixie Zhou and Jian Luo, 2015, 91, 202-216. The dissertation author was the primary investigator and author of this paper. All calculations and data analysis were performed by the author except for some of the sintering data.

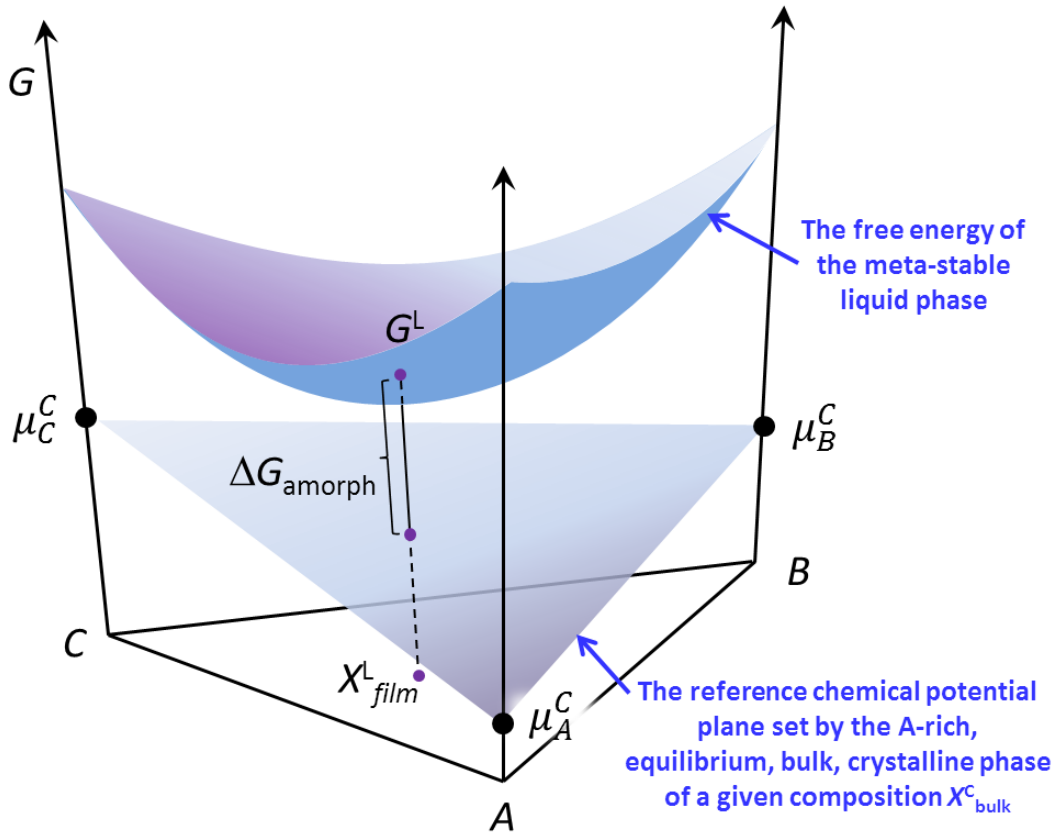

Figure 2.1 Schematic illustration of in a hypothetic ternary A-B-C system.

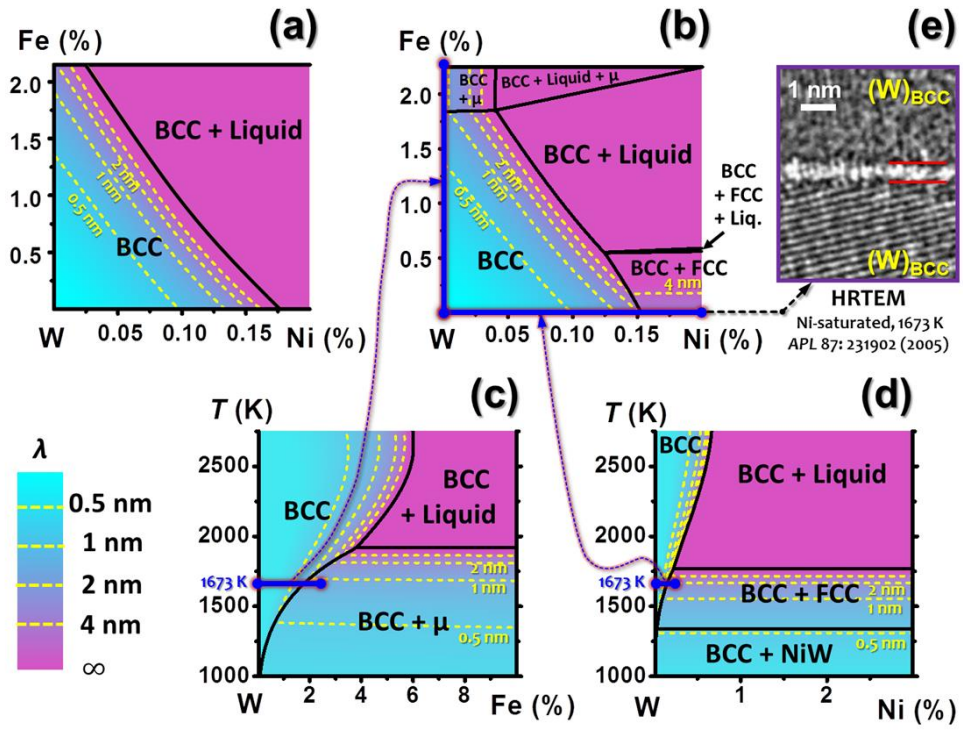

Figure 2.2 Schematic illustration of the two-step procedure to construct an isothermal section of a ternary GB λ-diagram for W-Ni-Fe at 1673 K. (a) First, $\lambda(\mathbf{X}_{bulk}^{BCC})$ values are computed and plotted at a function of bulk composition of the BCC phase without considering the precipitation of any secondary crystalline phase. (b) Subsequently, the precipitation of other equilibrium secondary phases (FCC and μ-FeW in this specific case), which limit the bulk chemical potentials and λ values in two- and three-phase coexistence regions, are considered. The corresponding binary GB λ diagrams for (c) W-Fe and (d) W-Ni. (e) A HRTEM image showing a nanoscale quasi-liquid IGF, adapted from Ref. [15] with permission.

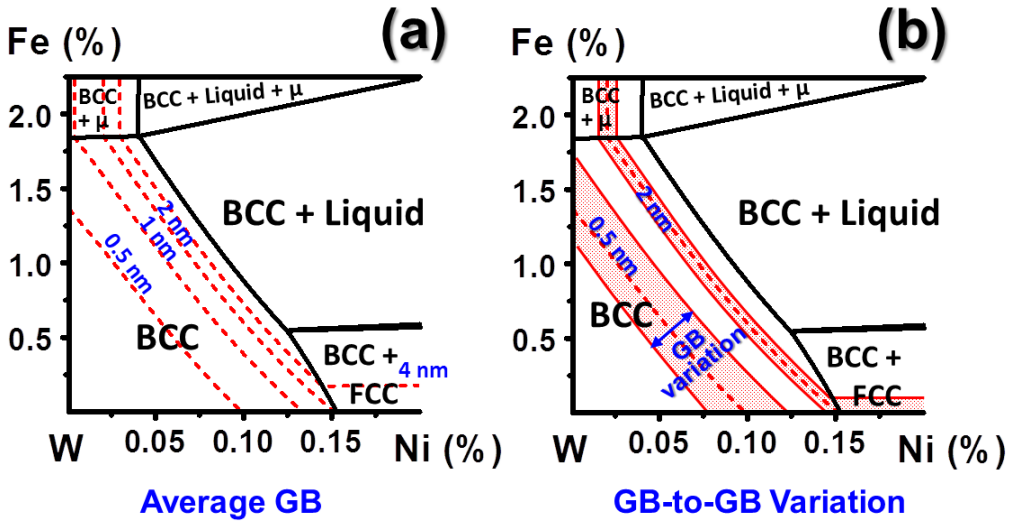

Figure 2.3 (a) An uncolored computed GB λ diagram for the average general GBs in W-Ni-Fe at 1673 K and (b) the corresponding estimated GB-to-GB variations. Panel (a) shows four lines of constant λ (λ = 0.5, 1, 2 and 4 nm), while panel (b) only displays two bands that correspond to λ = 0.5 and 2 nm, respectively, for clarity.

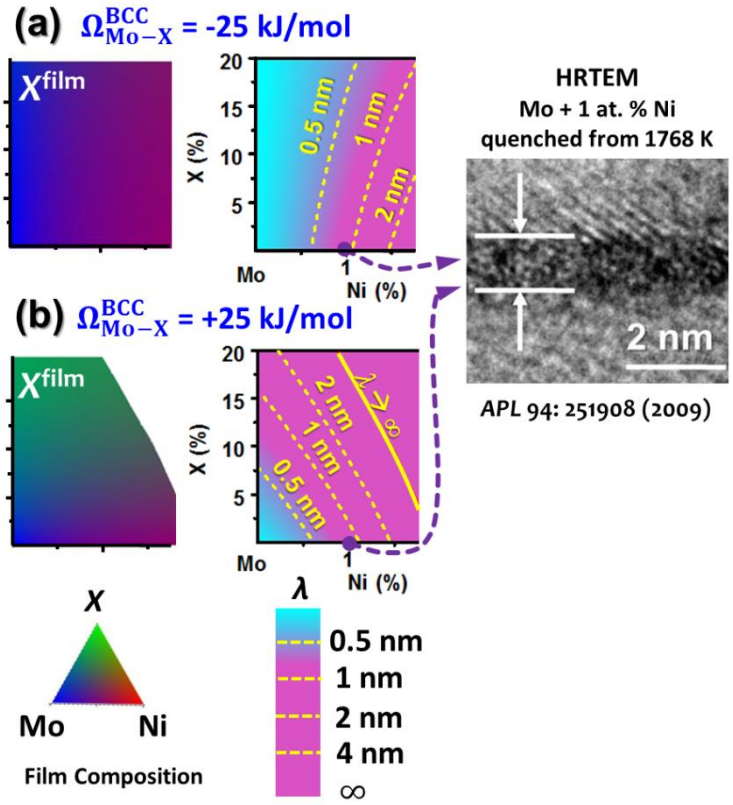

Figure 2.4 Computed GB λ diagrams suggesting that adding an alloying element X that has a negative (positive) pair-interaction parameter with Mo can inhibit (promote) GB disorder. The HRTEM image is adapted from Ref. [19] with permission.

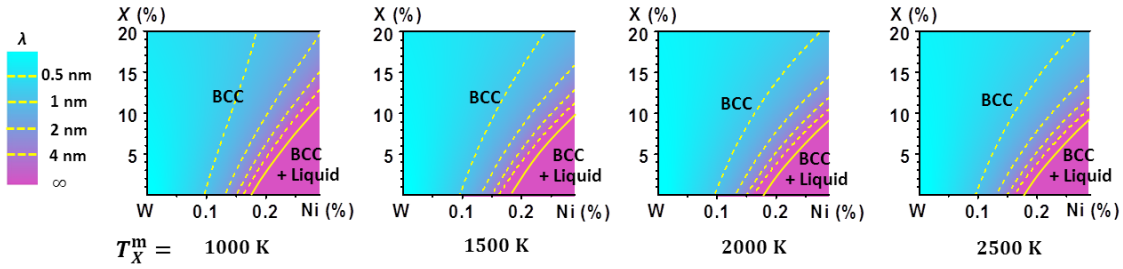

Figure 2.5 Computed GB λ diagrams for W-Ni-X systems at 1673 K showing that the melting temperature of X (T_X^m) has little impact on GB disordering in the W rich region. In this set of numerical experiments, X was assumed to form ideal solutions with W and Ni for simplicity.

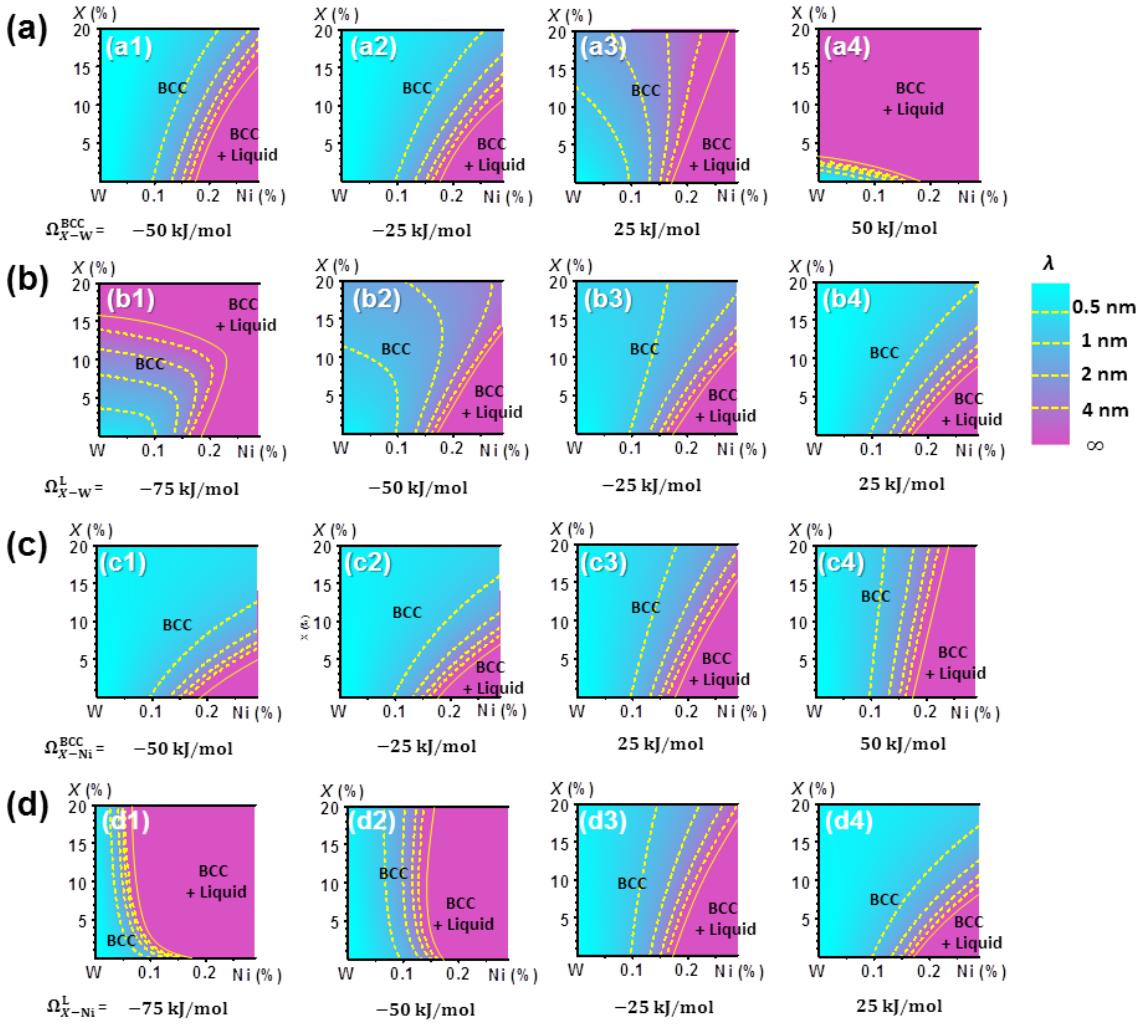

Figure 2.6 The effects of varying (a) $\Omega^{BCC}_{W\text{-}X}$, (b) $\Omega^{L}_{W\text{-}X}$, (c) $\Omega^{BCC}_{Ni\text{-}X}$ and (d) $\Omega^{L}_{Ni\text{-}X}$ on the computed GB λ diagrams for W-Ni-*X* systems at 1673 K. These calculations assumed that T^{m}_{X} = 2000 K and *X* forms ideal solutions with W and Ni other than one regular solution, for which the Ω value is labeled below the diagram.

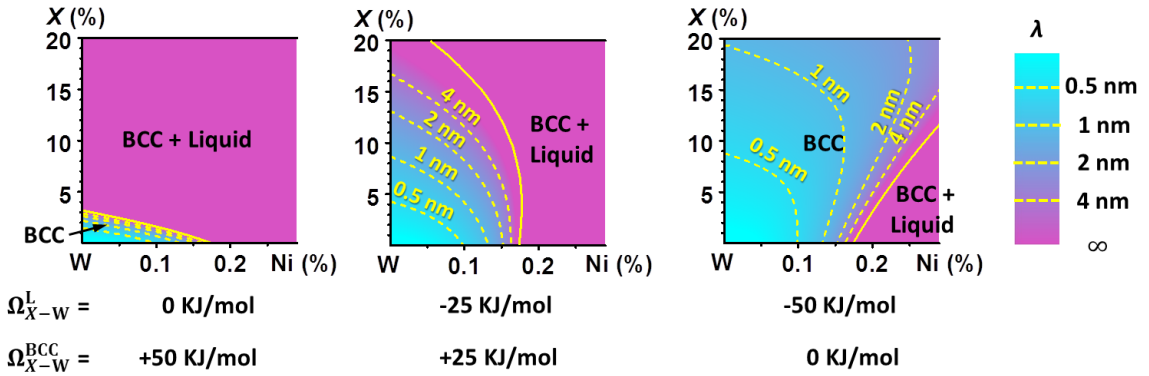

Figure 2.7 The effects of varying (a) $\Omega^{BCC}_{W\text{-}X}$, (b) $\Omega^{L}_{W\text{-}X}$, (c) $\Omega^{BCC}_{Ni\text{-}X}$ and (d) $\Omega^{L}_{Ni\text{-}X}$ on the computed GB λ diagrams for W-Ni-*X* systems at 1673 K. These calculations assumed that T^{m}_{X} = 2000 K and *X* forms ideal solutions with W and Ni other than one regular solution, for which the Ω value is labeled below the diagram.

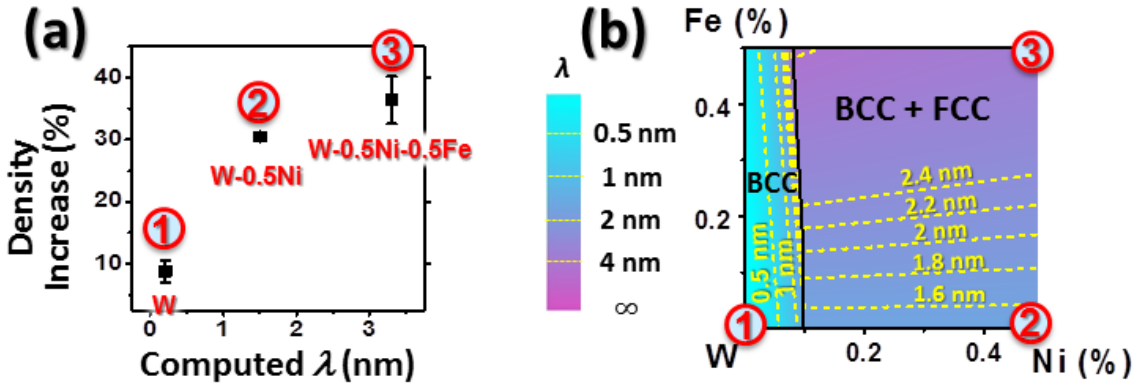

Figure 2.8 (a) The density increases for three specimens (W, W-0.5Ni and W-0.5Ni-0.5Fe at. %) after sintering at 1573 K for two hours *vs.* the computed λ values for these three compositions. Adding 0.5 at. % Ni as a sintering aid significantly boosted the densification of W and adding 0.5 at. % Fe as a co (the second) sintering aid further enhanced the densification. (b) The corresponding computed GB λ diagram for W-Ni-Fe at 1573 K, in which the three selected composition points are labeled.

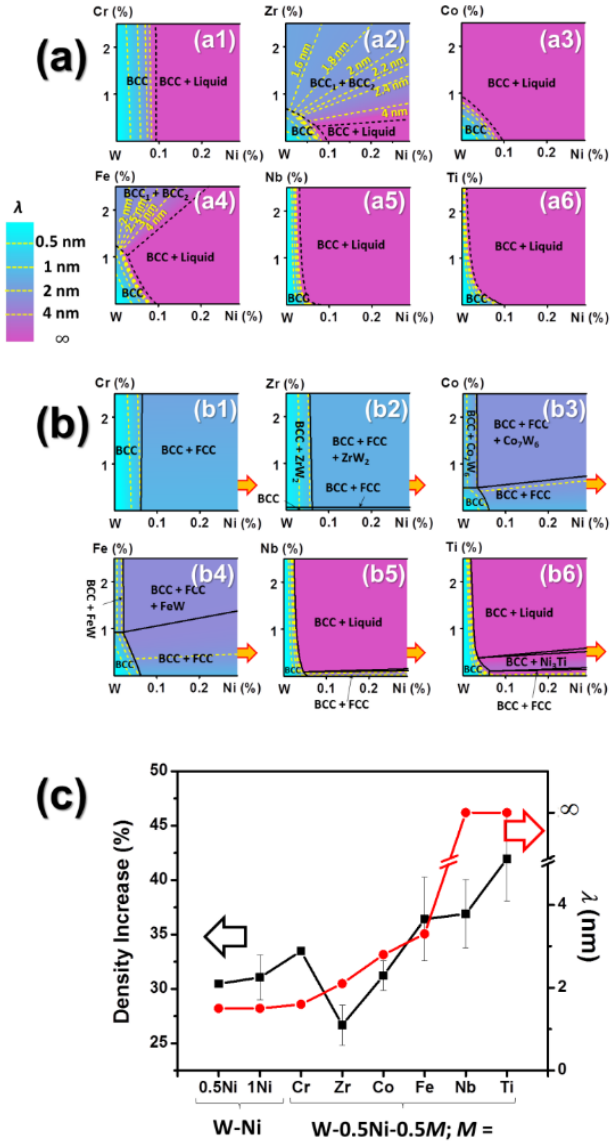

Figure 2.9 Computed GB λ diagrams for the W-Ni-*M* (*M* = Cr, Zr, Co, Fe, Nb and Ti) systems at 1573 K considering (a) only the BCC and liquid phases (*a.k.a.* without considering the precipitation of secondary crystalline phases) and (b) all possible equilibrium phases, respectively. (c) Calculated λ values generally correlate well with the measured density increases after 2-hour sintering at 1573 K for this series of ternary W-0.5Ni-0.5*M* (at. %) alloys, along with binary W-0.5Ni and W-1Ni (at. %) alloys as the references. Noting that the composition points of W-0.5Ni-0.5*M* (at. %) are outside the plotted regions of these GB λ diagrams (that are expanded to 0-0.3 % Ni to clearly show the low concentration regions), but there are little changes in the computed λ values beyond 0.3 at. % Ni.

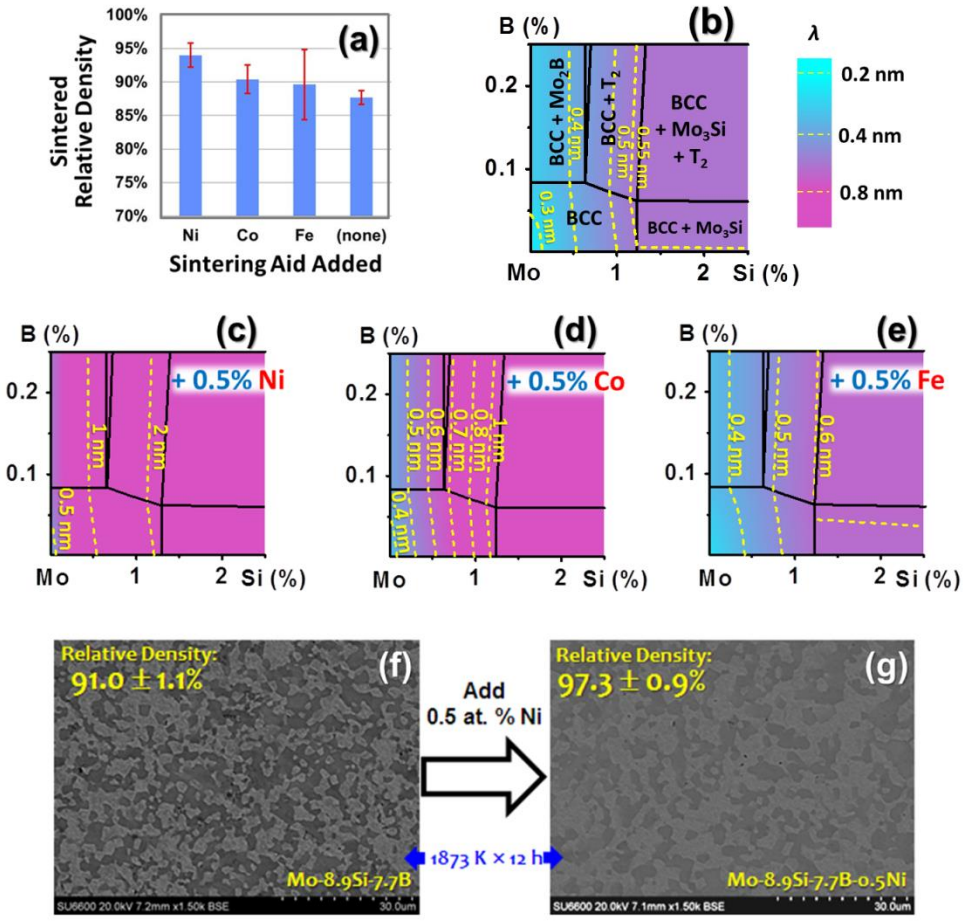

Figure 2.10 (a) The relative effectiveness of adding 0.5 at. % Ni, Co and Fe as sintering aids on the final sintered densities of Mo-Si-B alloys after isothermal sintering at 1873 K for 3 hours (repotted after the data in Ref. [17]). (b) A computed ternary GB *λ* diagram for Mo-Si-B at 1873 K. (c, d, e) The pseudo-ternary sections of GB *λ* diagrams for the quaternary Mo-Si-B-0.5M systems at 1873 K and a fixed atomic fraction of 0.5 at. % *M* (*M* = Ni, Co and Fe) (f, g) Additional (new) experiments showed that adding 0.5 at. % Ni (the most effective sintering aid predicted) substantially increased the densification of Mo-Si-B alloys to achieve >97 % of the theoretical density after 12 hours' sintering at 1873 K.

Table 2.1 The regular solution parameters for W-*M* and Ni-*M* (*M* = Ni, Co, Fe, Zr, Cr, Ti and Nb) at 1573 K from Ref. [80, 81, 84-91]. The datum for $\Omega^{BCC}_{Ni\text{-}Co}$ is not available so that $\Omega^{FCC}_{Ni\text{-}Co}$ is listed instead (denoted by *).

M =	$\Omega^{BCC}_{W\text{-}M}$ (kJ/mol)	$\Omega^{L}_{W\text{-}M}$ (kJ/mol)	$\Omega^{BCC}_{Ni\text{-}M}$ (kJ/mol)	$\Omega^{L}_{Ni\text{-}M}$ (kJ/mol)
Ni	82.0	-0.9	/	/
Co	54.7	-16.7	1.3^{*}	1.3
Fe	41.5	5.8	-1.2	-8.3
Zr	48.2	9.8	-143	-148
Cr	31.5	-70	-1.5	-10.3
Ti	22.8	16.3	-77.2	-95.4
Nb	0	0	-10.3	-90.6

Chapter 3. Calculation and Validation of a GB Complexion Diagram for Bi-doped Ni

A GB (GB) “phase” (complexion) diagram is computed via an Ising (lattice) type statistical thermodynamic model for the average general GBs in Bi-doped Ni. The predictions are calibrated with previously-reported density functional theory calculations and further validated systematically by experiments, including both new and old aberration-corrected scanning transmission electron microscopy characterization results as well as prior Auger electron spectroscopy measurements. This work supports a major scientific goal of developing GB complexion diagrams as an extension to bulk phase diagrams and a useful science tool.

3.1. Introduction

The development of GB complexion diagram as an extension to bulk phase diagrams and a generally-useful materials science tool can help designing and engineering materials’ macroscopic properties controlled by GBs. In previous chapter, bulk CALPHAD methods are extended to multicomponent systems to model coupled GB premelting and prewetting. Subsequently, a class of “GB λ diagrams” are constructed to represent the thermodynamic tendency for general GBs to disorder. In this chapter, we computed a GB complexion diagram for average general GBs in Bi-doped Ni, for which a recent experimental study found ubiquitous formation of a bilayer complexion at virtually all general GBs at 700°C and 1100°C [31]. Furthermore, we constructed complexion diagrams for two

special GBs based on the 0K density functional theory (DFT) calculations reported in two prior studies [105, 106] for assessing both the lattice model and GB-to-GB variations. Subsequently, the computed GB complexion diagram has been validated by both direct AC STEM characterization (including new AC STEM results for a specimen quenched from 1400°C collected in this study and previously-reported results for 700°C and 1100°C [31]) and previously-reported AES analysis of GB segregation [107].

3.2. Method

The GB energy of a binary A-B alloy can be expressed as:

$$\gamma_{GB} = U_{GB}^{XS} - TS_{GB}^{XS} - \sum_i \left(\Gamma^A \mu^A + \Gamma^B \mu^B \right), \tag{25}$$

where U^{xs} is the excess internal energy, S^{xs} are the excess entropy, μ's are bulk chemical potentials, and Γ's are the corresponding GB excesses (adsorption amounts). Similar to the free-energy functions of bulk phases, different functions of γ_{GB} can be written for different GB complexions and their intersections define GB transitions, *e.g.*, the occurrence of a premelting transition with increasing temperature from low or high S^{xs} or an adsorption transition with increasing chemical potential difference from low to high Γ. In this study, we focus on GB adsorption transitions.

Here, we adopt a Wynblatt-Chatain type multilayer adsorption model [45] to formulate an expression of γ_{GB} using an Ising type lattice model (assuming that each lattice point is occupied by either Ni or Bi atoms). The following expression

is derived for a "general" (100) twist GB (to represent the average general $\Sigma\infty$ GBs, for which the fraction of "broken bonds" is set to match that of typical "random" GBs in metals) to represent the average general GBs in Bi-doped Ni:

$$\gamma_{GB} = 2 \cdot min\Big\{0.5(1-P)z_v N[2X_{GB}^1(1-X_{GB}^1)\omega + X_{GB}^1 e_{BiBi} + (1-X_{GB}^1)e_{NiNi}] - N\sum_{i=1}^{+\infty}[X_{GB}^i \Delta E_{els}^i] + N\omega\sum_{i=1}^{+\infty}\left[-z\left(X_{GB}^i - X_{Bulk}\right)^2 + z_v\left(X_{GB}^i - X_{GB}^{i+1}\right)^2\right] + NkT\sum_{i=1}^{+\infty}\left[X_{GB}^i ln\left(\frac{X_{GB}^i}{X_{Bulk}}\right) + (1-X_{GB}^i) ln\left(\frac{1-X_{GB}^i}{1-X_{Bulk}}\right)\right]\Big\} \quad (26)$$

where X_{GB}^i is the fraction of Bi atoms in the *i*-th layer near the GB core, $e_{\text{Ni-Ni}}$ (= -0.73 eV/bond) and $e_{\text{Bi-Bi}}$ (= -0.38 eV/bond) are bonding energies estimated from atomization enthalpies, ω [$= e_{Ni-Bi} - 0.5(e_{Ni-Ni} + e_{Bi-Bi})$] is the regular-solution parameter (estimated to be -0.017 + $1.1\times10^{-5}T$ eV/bond for Ni-Bi from the CALPHAD data [108]), z (= 12) is the total coordination number in FCC, z_v (= 4) is the number of bonds per atom to one adjacent (100) plane (or z_v = 3 for twist (111) GBs), P is the fraction of reconnected bonds that is set as 5/6 to let $\gamma_{GB}^{(0)}/\gamma_{surface}^{(0)}$ = 1/3 to represent an average general GB, and $N = 2.5\times10^{-5}$ mole/m^2 is the number of the lattice sites per unit area. ΔE_{els}^i is the elastic energy in the *i*-th layer, which decreases exponentially with the distance to the GB core (h^i) according to: $\Delta E_{els}^i = \Delta E_{els}^1 \exp\left[-1.01\left(h^i/r_{Bi}\right)^{1.53}\right]$, where r_{Bi} is the atomic radius of Bi and ΔE_{els}^1 (= 0.27 eV/atom for a Bi atom on the FCC Ni lattice) is obtained from the Friedel model [45]. The equilibrium compositional profiles are obtained by minimizing Eq. (26) ($\partial\gamma_{GB}/\partial X_{GB}^i = 0$), leading to a McLean type adsorption equation for each layer:

$$\frac{X_{GB}^{i}}{1-X_{GB}^{i}} = \frac{X_{Bulk}}{1-X_{Bulk}} \exp\left(-\frac{\Delta H_{seg}^{i}}{RT}\right) \quad (27)$$

where ΔH_{seg}^{i} is the adsorption enthalpy in the *i*-th layer and its expression can be found in Ref. [45]. For given bulk composition (chemical potentials μ's) and temperature (*T*), the equilibrium GB compositional profile and GB energy can be obtained from Eq. (26) and Eq. (27) by minimizing γ_{GB} numerically via an iteration method. Then, the GB excess of solute can be calculated via: $\Gamma = 2N\sum_i (X_{GB}^{i} - X_C)$.

3.3. Results and discussion

Multiple complexions with different compositional profiles can satisfy Eq. (27) for a give set of μ's and *T*; in such a case, the compositional profile that produces the minimum γ_{GB} represents the equilibrium complexion and others are metastable. If two complexions have the same minimum γ_{GB}, a GB transition can occur between them and it is first-order if first derivatives of γ_{GB} are discontinuous at the intersection.

Fig. 3.1 displays computed normalized GB energy ($\gamma_{GB}/\gamma_{GB}^{(0)}$) and adsorption ($\Gamma$) *vs.* bulk composition (X_{Bulk}) curves for Bi-doped Ni at three different temperatures. Here, $\gamma_{GB}^{(0)}$ is computed to be ~1.26 J/m^2 for the average general GBs in pure Ni, which is consistent with experiments (~1 J/m^2) and DFT calculations (1.2-1.4 J/m^2) [105, 109, 110]. At each temperature, the GB undergoes a first-order phase-like (complexion) transformation with increasing bulk composition, from a "clean" GB to a bilayer; here, both the "clean" GB and the bilayer are nominal as the actual GB excess (Γ), which varies with the chemical

potential, is around the nominal value of 0 and 2 monolayers, respectively (Fig. 3.1). These GB transitions are first-order, as indicated by the discontinuities in the slopes in the $\gamma_{GB}/\gamma_{GB}^{(0)}$ *vs.* X_{Bulk} curves and finite jumps in the Γ *vs.* X_{Bulk} curves. The first-order GB transition also occur at 1400°C, but above the solidus line, so that the bilayer is not an equilibrium complexion. It is interesting to further note that the metastable GB transition is nearly continuous at 1400°C (see Fig. 3.1(f)); thus, a metastable critical point may exist above 1400°C (in the supersaturated region).

The lattice type models have several limitations. They do not consider possible structural changes at GBs (by placing all atoms on the lattice) and rely on empirical parameters. Thus, we further compare this model with two prior DFT calculations [105, 106] that consider the detailed atomic structures (for selected special GBs at T = 0K). Fig. 3.2 compares the (γ_{GB} - $\gamma_{GB}^{(0)}$) *vs.* chemical potential difference curves for two general twist GBs calculated using the lattice model and CALPHAD data with two independent DFT calculations [105, 106] for one twist GB and two tilted GBs at T = 0K. There are several differences between the lattice model and DFT calculations. First, the relaxed bilayer structures obtained by DFT is less dense than that of the lattice model. Second, $\Delta\gamma_{GB}^{BL}$ at $\Delta\mu$ = 0 is higher for DFT results because of the lower Γ. Third, the Bi chemical potentials in the NiBi compound obtained from the CALPHAD and DFT are somewhat different (noting that the CALPHAD data were fitted with reference to the bulk compound so that the relative chemical potentials are likely more important/relevant here). Finally,

the lattice model is designed to represent the average general GBs, whereas DFT calculations were conducted for two intermediate-energy special tilt GBs: Σ5 (210) and Σ5 (310) and one low-energy twist GB: Σ3 (111), for which bilayers are not stable as expected [31, 105, 106]. Nonetheless, the comparison shows that the relative stabilities of the "clean" *vs.* bilayer complexions at the average general GBs represented the lattice model are between the two DFT calculations for Σ5 (210) and Σ5 (310) tilt GBs [105, 106], which can be more clearly evident in the computed GB complexion diagrams shown in Fig. 3.2(c) and will be elaborated subsequently.

We should also note that the difference between two DFT calculations represents the anisotropy of complexion transitions. Calculations using the lattice model, however, represent "average" general GBs. In fact, computed $\Delta\gamma$ *vs.* $\Delta\mu$ curves are almost identical for two types of general twist GBs (Fig. 3.2(a)), both of which were selected to represent average general GBs, implying the robustness of this lattice model.

Furthermore, we have computed the GB transition lines and plot them in the bulk Ni-Bi phase diagram to construct a GB complexion diagram for Bi-doped Ni, as shown in Fig. 3.2(c). In addition, we used the DFT results (obtained for T = 0K) reported in two prior studies [105, 106] to calculate the complexion transition lines at finite temperatures using the following approximated thermodynamic relationship: $X_{\text{clean}\rightarrow\text{BL}} \approx X_{\text{solvus}}\cdot\exp(-\Delta\mu_{\text{BL-NiBi}}/\text{R}T)$, where the X_{solvus} is the solvus composition calculated by CALPHAD and $\Delta\mu_{\text{BL-NiBi}}$ is the chemical potential

difference calculated by DFT at T = 0K; this equation assumes that the Ni-Bi forms a regular solution and $\Delta\mu_{BL\text{-}NiBi}$ is constant independent of temperature.

The computed GB complexion diagram in Fig. 3.2(c) shows the stability regions for two complexions – a nominally "clean" complexion and a bilayer complexion – separated by first-order GB transition lines. All the calculated transition lines by different methods and/or for different GBs follow the same trends. The transition line calculated from the lattice model and CALPHAD data (to represent the average general GBs) is between those for the two special tilt GBs calculated based on the 0K DFT data. This suggest that (1) the lattice model calibrates well with DFT calculations and (2) there are significant GB-to-GB variations (*e.g.*, for the average general GBs and different special GBs) in the specific positions of the transition lines, as shown in Fig. 3.2(c), which are well expected.

Our prior study has already demonstrated via AC STEM high-angle annular dark-field (HAADF) imaging that bilayers form ubiquitously at solid-liquid coexistence (along the solidus line) at 700°C and 1100°C [31]. In this study, the lattice model (Fig. 3.1 and Fig. 3.3) further suggested that bilayer should vanish at T > ~1300°C along the solidus line for general GBs. To verify this prediction, we conducted an additional experiment to anneal a Ni polycrystalline specimen in direct contact with an equilibrium Bi-Ni liquid at 1400°C and subsequently quenched it to preserve its high-temperature GB configuration. The TEM specimens were prepared by a focused ion beam and characterized with AC

STEM. Electron backscattering diffraction was used to make sure the selected GB is a general GB. Here, we adopted the same experimental procedure as that in the prior study [31], except for a specimen annealed and quenched at/from a higher temperature of 1400°C. The HAADF STEM image, as shown in the top-right corner of Fig. 3.3, verified the prediction of the computed GB complexion diagram, *i.e.*, the bilayer vanished.

The occurrence of a first-order GB transition from nominally clean GBs to nominal bilayers is also consistent with a prior AES study of GB segregation by Chang and Huang [107], who found that a first-order GB transition occurred at ~400°C in Ni + 90 wt. ppm Bi (*i.e.*, $X_{Bi} \approx 0.0026\%$) specimens, which falls almost exactly on the calculated transition line in the complexion diagram shown in Fig. 3(a), although the observed transition temperature was higher than that predicted in Fig. 3.3(a) for specimens with a higher Bi content (meaning that the slope of the GB transition line suggested by that AES study was higher) [107]. Overall, the agreements between the computed GB complexion diagram for the general GBs (Fig. 3.3(a)) and various experiments (both STEM and AES) are satisfactory.

3.4. Conclusion and summary

In summary, we have computed a complexion diagram for the average general GBs in Bi-doped Ni using a lattice model and CALPHAD data. The computed results are critically assessed with two earlier reports of 0K DFT calculations. The computed GB complexion (phase) diagram has been systematically validated with experiments, including direct AC STEM

characterization (both previously reported data for specimens quenched from 700°C and 1100°C [31] and a new experiment on a specimen quenched from 1400°C) and an early AES study of GB segregation [107]. In addition to the earlier development GB λ-diagrams that can forecast the trends in GB disordering and related sintering behaviors at high temperatures [7-10, 29, 35], this study constructed a more rigorous GB complexion diagram with well-defined transition lines that can be verified by experiments. Future research should be conducted to compute and validate other GB complexion diagrams to realize a potentially-transformative scientific goal of constructing more GB complexion diagrams as a new materials science tool.

Chapter 3, in part, is a reprint of the material "Calculation and validation of a GB complexion diagram for Bi-doped Ni" as it appears in Scripta Materialia, Naixie Zhou, Zhiyang Yu, Yuanyao Zhang, Martin P. Harmer, and Jian Luo, 2017, 130, 165-169. The dissertation author was the primary investigator and author of this paper. All experiments and data analysis were performed by the author except for the sample preparation and TEM characterization data.

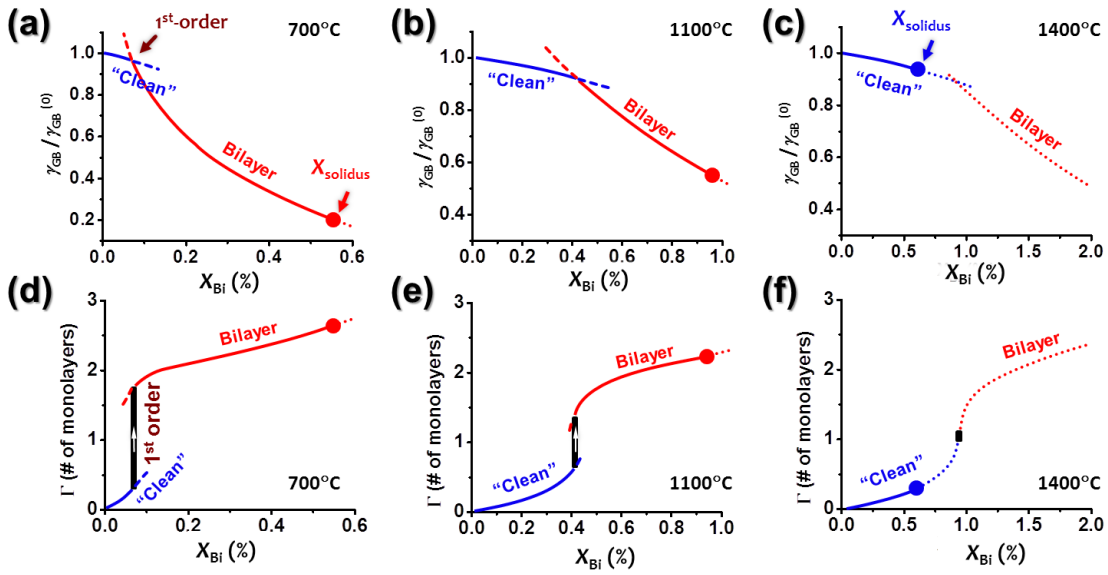

Figure 3.1 Calculated normalized GB energy ($\gamma_{GB}/\gamma_{GB}^{(0)}$) *vs.* bulk Bi composition (X_{Bi}) curves for Bi-doped Ni at (a) 700°C, (b) 1100°C, and (c) 1400°C, respectively, and the corresponding computed GB excesses of the solute (Γ's) at (d) 700°C, (e) 1100°C, and (f) 1400°C, respectively. GB complexion transitions occur when $\gamma_{GB}/\gamma_{GB}^{(0)}$ *vs.* X_{Bi} curves for the "bilayers" (red lines) and the "clean" GBs (blue lines) intersect. The first-order transitions correspond to the abrupt increases (finite jumps) of absorption in (d)-(f) or the associated discontinuities in the slopes in (a)-(c). The metastable regions of the complexions are represented by dashed lines. The dotted lines in (c) and (f) represent the oversaturated (metastable) region beyond the bulk solidus composition (that would occur only if the formation of the liquid phase was inhibited). Noting that the metastable GB transition is nearly continuous at 1400°C, as shown in (f), so that a metastable critical point may exist above 1400°C..

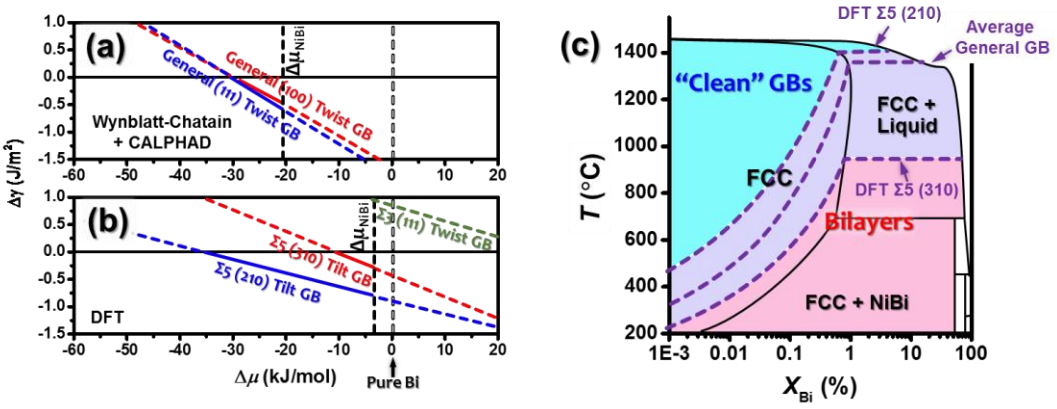

Figure 3.2 Comparison of computed relative GB energies ($\Delta\gamma = \gamma_{GB}^{bilayer} - \gamma_{GB}^{(0)}$) of the Bi-based bilayers at Ni GBs as functions of Bi chemical potential $\Delta\mu_{Bi}$ at T = 0K using (a) a Wynblatt-Chatain type lattice model for two general twist GBs to represent the average general GBs and (b) DFT calculations for three special GBs in two prior studies: a Σ5(210) tilt GB and a Σ3(111) twist GB from Ref. [105] as well as a Σ5(310) tilt GB from Ref. [106], and the computed GB complexion diagram of Bi-doped Ni in (c) for average general GBs using a lattice model and CALPHAD data and two special Σ5 GBs calculated based on previously-reported DFT data [105, 106] (the approximated approach described in text). In the complexion diagrams, black solid lines represent bulk phase boundaries and purple dashed lines indicate the calculated first-order GB transition lines from "clean" to "bilayer" complexions. The difference between these calculated transition lines in (c) corresponds to the calculation error and GB variations.

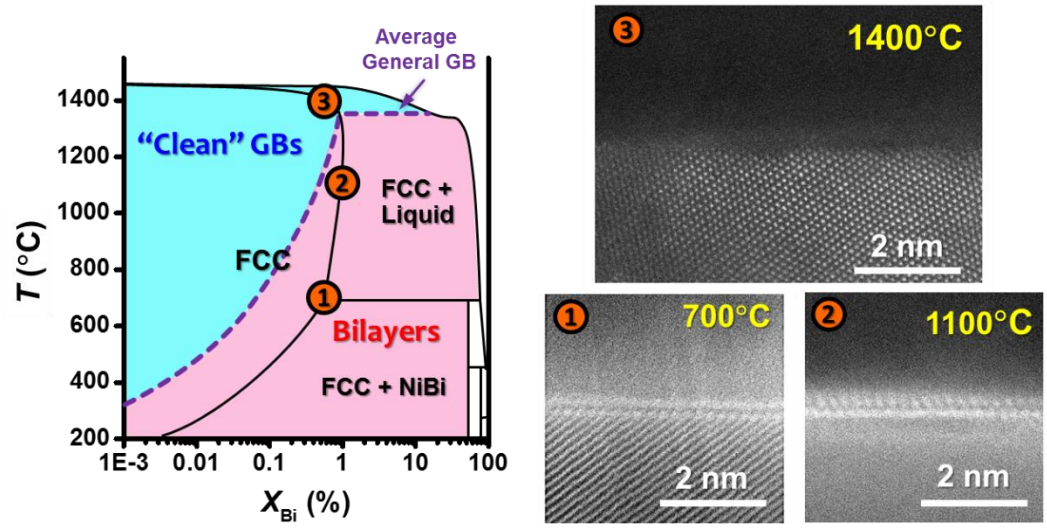

Figure 3.3 Computed GB complexion diagram for Bi-doped Ni for average general GB using a lattice model and CALPHAD data plotted with STEM images that verified the diagram. Black solid lines represent bulk phase boundaries and purple dashed lines indicate the calculated first-order GB transition lines from "clean" to "bilayer" complexions. The STEM specimens correspond to three different processing conditions on the diagram that are labeled by number 1,2,3.

Chapter 4. Systematics of GB Adsorption Transitions

A systematics of GB adsorption transitions is derived for Using an Ising type lattice GB model. A normalized segregation strength is defined to represent the effects of mixing energy, solute strain and differential bonding energies as well as the misorientation for symmetrical twist boundaries, which is shown to be a dominant factor in controlling adsorption transition behaviors. Various types of GB adsorption transitions are represented in three-dimensional spaces of the normalized segregation strength, reduced temperature, and chemical potential difference. For a strong segregation system with a large normalized segregation strength, a series of layering transitions occur at low temperatures; these first-order transitions end at GB roughing temperatures, above which the adsorption transitions become continuous. For a weak segregation system with a small normalized segregation strength, the layering transitions lump into thin-thick (prewetting) transitions without well-defined quantum numbers, analogous to the Cahn critical-point wetting model. The derivation of this systematics of high-temperature GB adsorption transitions, which exhibit phenomenological similarities to the cases of multilayer adsorption of inert gas molecules on the surfaces of attractive substrates, enriches the classical GB segregation/adsorption theory.

4.1. Introduction

GB adsorption undergo transitions, is one important physical phenomenon. Various lattice type GB statistical models were developed to describe GB

adsorption as a function of temperature and bulk concentration as discussed in Chapter 1. In 1957, McLean first proposed a classical GB adsorption model [54] in analogy to the Langmuir surface adsorption model [111]. His model considers fixed adsorption sites per unit area (monolayer region) at a GB and the model also assumes ideal interactions between components in both bulk and GBs. Hondros and Seah [41] extended McLean model by including the adsorbate-adsorbate interaction at GBs uses analogues of the surface adsorption theories by Fowler-Guggenheim [112], and the model suggests the existence of first order adsorption transition in systems with strong adsorbate-adsorbate attraction at GBs. Wynblatt and Chatain simulated solid state prewetting/wetting transition using a more sophisticated GB adsorption model [44, 45] that considers multilayer adsorption sites at GBs and more realistic regular solution interactions. More recently, Rickman formulated a Ising type lattice gas GB model [47] in analogy to classical multilayer lattice gas type surface adsorption model [113], by which, he simulated a series of first order layering adsorption transitions in Cu-Ag system. While prior theories or modeling studies mostly focus on describing one particular type of GB transitions, this study aims to establish a systematics of GB adsorption transitions that include wetting, prewetting, layering, and roughening, as well the transitions among different behaviors, and further describe the GB adsorption transition behaviors systematically in a small set of normalized parameters.

4.2. Ising type lattice gas GB model

In an Ising type lattice gas model, the adsorption near a symmetrical twist GB (with an arbitrary twist angle, to represent a general boundary) in a binary A-B system can be described on a set of lattice sites, each of which is represented by a variable n_k = 0 (for the occupation of a solvent atom A) or 1 (for that of a solute atom B). Since a solute atom near the GB core has a different bonding environment and (typically larger) free volume, it can have different (e.g., lower) energy (enthalpy) from that inside the bulk, which is characterized by a GB potential V_k. The total energy of the system in a respective microstate can be expressed as:

$$E = \mathcal{H} - N_B \Delta\mu = 0.5\sum_k \sum_{l \neq k} J_{kl} + \sum_k \left(V_k - \Delta\mu\right) n_k \tag{28}$$

where $\mathcal{H}$ is the Hamiltonian of the GB system, $N_B = \sum_k n_k$ is the total number of solutes, and $\Delta\mu = \mu_B - \mu_A$ is the chemical potential difference between solute and solvent, k and l label the lattice sites, and J_{kl} is the pairwise interaction. For simplicity, it is assumed that the GB potential V_k only depends on the distance between the site and the central/twist plane at the GB core; an Ising type pair interaction is adopted where $J = \omega$ for two different nearest neighboring species ($n_k \neq n_l$) and $J = 0$ otherwise.

For a tilted GB, under Bragg-Williams approximation, Eq. (28) can be written as:

$$\overline{\Omega} = 2N \sum_i \left[\overline{J_i} - \overline{S}_i T - X_i \left(\Delta\mu - V_i \right) \right] \tag{29}$$

where *N* is the lattice per unit area, the prefactor 2 corresponds to the summation of two sides of the symmetric GB, $\overline{J_i}$ is the average total pair interaction energy per atom on *i*th GB layer, $\overline{S_i}$ is *i*th layer's average mixing entropy per atom and X_i is *i*th layer's average solute composition (also can be viewed as the possibility of one GB site on *i*th layer occupied by a solute atom). The average total pair interaction energy on *i*th GB layer is:

$$\overline{J_i} = \omega(\mathrm{z}-2z_v)(1-X_i)X_i + 0.5z_v\omega\left[(1-X_{i-1})X_i + X_{i-1}(1-X_i) + (1-X_{i+1})X_i + X_{i+1}(1-X_i)\right] \tag{30}$$

where *z* and the number is the total coordinate number per atom, z_v is the number of out layer bonds (bonds with one of the adjacent layer) and *N* is the number of site per unit area. In eq. (30), the first term corresponding to the interaction between atoms within the same layer and the second term within the square brackets corresponds to the interactions between adjacent layers. Eq. (30) can be rearranged as

$$\overline{J_i} = z\omega(1-X_i)X_i + 0.5z_v\omega\left(X_i - X_{i+1}\right)^2 + 0.5z_v\omega\left(X_i - X_{i-1}\right)^2 \tag{31}$$

where the first term is the interaction energy for GB layers with uniform composition at X_i and the rest terms are the extra energy due to through layer compositional gradient.

The ideal mixing in the configure entropy is:

$$\overline{S_i} = -k_B\left[X_i \ln X_i + (1-X_i)\ln(1-X_i)\right] \tag{32}$$

By combining eq. (29-32), we could rewrite eq. (29) into:

$$\overline{\Omega} = 2N\sum_i \left\{ z\omega(1-X_i)X_i + z_v\omega\left(X_i - X_{i+1}\right)^2 + k_B T\left[X_i \ln X_i + (1-X_i)\ln(1-X_i)\right] - \left(\Delta\mu - V_i\right)X_i \right\} \tag{33}$$

We note that the model derived is similar to Rickman's GB model [47] which is developed based on cubic lattice while Rickman's model also considers low angle GB composed by discrete dislocations (Read-Shockley type GB model) in which GB potential may only be translational invariant along dislocation lines.

In Eq. (33), $\overline{\Omega}$ is the grand potential referenced to a "clean" GB, which is essentially the GB energy reduction due to adsorption:

$$\gamma_{GB} - \gamma_{GB}^{(0)} = \overline{\Omega} + 2i_{\max}N\left(\mu_A - \mu_A^{(0)}\right) \tag{34}$$

where γ_{GB} and $\gamma_{GB}^{(0)}$ is the GB energy with adsorption/segregation and GB energy of pure solvent respectively, $2i_{max}N$ is the total number of atoms in the system and $\mu_A^{(0)}$ is the chemical potential of pure solvent.

At a given temperature T and bulk composition X_{bulk} (that defines the equilibrium chemical potentials), the equilibrium composition profile, that corresponds to the minimum in Eq. (33) or (34) with respect to the boundary condition, can be obtained by $\partial\overline{\Omega}/\partial X_i = 0$, leading to a set of McLean type segregation equations:

$$\frac{X_i}{1-X_i} = \frac{X_{bulk}}{1-X_{bulk}}\exp\left(-\frac{\Delta H_i^{seg}}{k_B T}\right) \tag{35a}$$

$$\Delta H_i^{seg} = V_i + 2z\omega\left[\left(X_{bulk} - X_i\right) + 2z_v z^{-1}\left(X_i - X_{i+1} - X_{i-1}\right)\right] \quad (35b)$$

where ΔH_i^{seg} is the segregation energy and we note that $X_0 = X_1$ because the 0-th layer is the 1-st GB layer on the other side for symmetric GBs. For convenience, $v(i) \equiv V_i/V_1$ is introduced to describe the decaying of GB potential with i increase where V_1, as the first layer GB potential, represents the magnitude of the potential, specifically $v(1) = 1$ and $v(\infty) = 0$.

All energetic terms in Eq. (35) are normalized with respect to the mixing energy $z\omega$: the thermal energy $k_B T$ is normalized to T/T_C where $T_C = z\omega/2k_B$ is the critical temperature of phase separation and $\Delta\mu$ is normalized to $\Delta\mu/z\omega$. A unit less quantity namely normalized segregation strength is further introduced as:

$$\phi_{seg} \equiv -2V_1/z\omega \quad (36)$$

where the prefactor 2 counts both sides of the symmetric GB. ϕ_{seg} reflects the relative tendency of segregation against phase separation and it also represents the overall effects of the interactions between the components as reflected by the mixing energy zω, the bonding energies' difference between the components in the pure state and the solute strain energy term arising from size differences between solute and solvent atoms, and the GB anisotropy [44, 45]. ϕ_{seg} considering these effects can be quantitatively formulated using Wynblatt-Chatain model. For example, for a (100) twisted GB in FCC system, it can be derived that:

$$\phi_{seg} \approx -0.4\sin^{1/4}\left(\frac{\Delta\theta}{2}\right)\left[\tfrac{1}{2} z_v \Delta e_{bond} + \beta\Delta E_{el}^{\infty}\right]\left(z\omega\right)^{-1} \quad (37)$$

where $\Delta\theta$ is the misorientation angle of GBs, Δe_{bond} stand for the differential bonding energy between solute and solvent, β is a constant and ΔE_{el}^{∞} is the solute strain energy.

4.3. Lattice gas model for more general interfacial segregation/adsorption modeling.

As Fig. 4.1 shows, the lattice gas GB model is isomorphic to other lattice gas interfacial models used in physical absorption or surface segregation. Here we specify the major similarities and differences among lattice gas models for GB segregation, surface segregation and physical absorption:

1) Lattice gas model for physical absorption considers only one component and the lattice sites are described with occupied or empty state. Liquid phase and gas phase are characterized by the average occupation density of lattice sites. GB and surface segregation model consider binary systems and lattice sites also have two states which are solvent occupied or solute occupied state. Solvent rich phase and solute rich phase are described by low and high average composition respectively. An analogy can be made between solute rich state in GB (or surface) segregation with liquid state in physical absorption which both correspond to average *n* close to 1.

2) There is only one type of interaction between atoms for physic absorption while for GBs (or surface) there are three types of atom interactions (interactions between solute-solute, solute-solvent and solvent-solvent). The attractive interactions between adatoms in lattice gas physical absorption model play a

similar role as the repulsive interactions between solute-solvent atoms in lattice gas GB model, though the absolute magnitude of interaction should be much smaller for adatoms than chemical bonding in solid phase.

3) The physic origins of interfacial potentials are different for physical absorption on substrate and interface segregation in solid phase. The adatom-substrate interactions are real interactive forces (e.g. van der Waals forces or electrostatic force) for physical absorption while GB (or surface) potentials are produced indirectly from the GB and bulk regions' difference of bonding condition and elastic properties, therefore the magnitude of the interfacial potentials V and the decaying functional of potentials v should be different for gas absorption and GB (or surface) segregation, also we may expect the surface potential will be larger than GB potential since surface has more broken bonds than GB.

Due to the similarity in the mathematic expressions of these three models, the results presented for lattice gas GB model will able to be generalized to the phenomenon in physical absorption and surface segregation.

4.4. Comparison of the Wynblatt-Chatain GB model and the lattice gas model

Segregation isotherms by a lot of existing lattice based GB segregation models can be resolved to a common form as eq. (36) while the model differences are reflected in the model parameters choosing and formalisms of GB potential functional as Table 4.1 summarized. In this study, we choose Wynblatt-Chatain model's GB potential formalism for numeric calculations of GB complexion

thermodynamics. In the following part, a detailed derivation will be demonstrated for the extraction of GB potential from Wynblatt and Chatain model [44].

Wynblatt and Chatain have derived previously the free energy of GBs through a similar scheme as the lattice gas GB model [44]. The major difference between lattice gas GB model and Wynblatt-Chatain model is that Wynblatt and Chatain considered non-zero bonding energies between same type of atoms and a fraction the bonds crossing the GB plane are assumed to be broken. GB energy expression according to the Wynblatt-Chatain formulism then can be derived for a symmetric twisted GB with J_{max} = 1 (bonds length will not exceed layer thickness) as [44, 114]:

$$\gamma_{GB} = \min\left\{\begin{array}{l}(P-1)z_v N\left[2X_1(1-X_1)\omega + X_1 e_{BB} + (1-X_1)e_{AA}\right] + 2N\sum_i X_i \Delta E_{el}^i \\ -2zN\omega \sum_i (X_i - X_\infty)^2 + 2z_v N\omega \sum_i (X_i - X_{i+1})^2 \\ +2Nk_B T\sum_i \left[X_i \ln(\frac{X_i}{X_\infty}) + (1-X_i)\ln\left(\frac{1-X_i}{1-X_\infty}\right)\right]\end{array}\right\} \quad (38)$$

where P is the fraction of crossing GB bonds which remain connected. ΔE_{el}^i is the strain energy that can be release by switching a bulk solute with a solvent at i-th GB layer and ΔE_{el}^i decreases exponentially with the distance to the GB core (h^i) according to: $\Delta E_{el}^i = \Delta E_{el}^1 \exp\left[-1.01\left(h^i / r_B\right)^{1.53}\right]$ where r_B is the atomic radius of B; ΔE_{el}^1 is given by the Friedel model. Using the relationship that: $\gamma_{GB}^{(0)} = (P-1)z_v N e_{AA}$, we could rewrite eq. (38) into:

$$\gamma = \gamma_{GB}^{(0)} + (P-1)z_v N\left[2X_1(1-X_1)\omega + (e_{BB}-e_{AA})\right]X_1 + 2N\sum_i X_i \Delta E_{el}^i$$
$$+2N\sum_{i=1}\left\{z\omega(1-X_i)X_i + z_v\omega\left(X_i - X_{i+1}\right)^2 + k_BT\left[X_i \ln X_i + (1-X_i)\ln(1-X_i)\right]\right\} \quad (39)$$
$$-2Ni_{\max}\left\{\left[k_BT\ln(\tfrac{X_\infty}{1-X_\infty}) + z\omega(1-2X_\infty)\right]X_i + k_BT\ln\left(1-X_\infty\right) + {X_\infty}^2 z\omega\right\}$$

Eq. (39) essentially adopt the same formulism of eq. (35) by the relations:

$$\begin{cases} V_{i=1} = \frac{1}{2}(P-1)z_v(e_{BB}-e_{AA}) + \Delta E_{el}^1 + (P-1)z_v(1-X_1)\omega \\ V_{i>1} = \Delta E_{el}^i \end{cases} \quad (40a)$$

$$\Delta\mu = k_BT\ln(\tfrac{X_\infty}{1-X_\infty}) + z\omega(1-2X_\infty) \quad (40b)$$

$$\mu_{solvent} - \mu_{solvent}^{(0)} = k_BT\ln\left(1-X_\infty\right) + {X_\infty}^2 z\omega \quad (40c)$$

Thus it can be seen that the Wynblatt-Chatain model is mathematically equivalent to lattice gas GB model with all the effects of strain energy and broken bonds crossing the GB plane summarized within the GB potential. It should be noted that the first layer GB potential (the third term of eq. 40a) is dependent on the X_1. Since the atomization enthalpy of elements (e_{nn}) is usually one to two magnitude larger than the mixing enthalpies (ω), the composition dependent term is here omitted in the quantification of normalized segregation strength ϕ_{seg} in this study:

$$\phi_{seg} \approx \left[(1-P)z_v(e_{BB}-e_{AA}) - 2\Delta E_{el}^1\right]/z\omega \quad (41)$$

which is a more general form of Eq. (37). According to eq. (41), the differential bonding energy ($e_{BB} - e_{AA}$) only influence V_1 while v_i is mainly determined by the strain energy ΔE_{el}'s fraction in V_1 which is defined as $f_{strain} = \Delta E_{el}^1 / V_1$. Fig. 4.2

shows the relationship between f_{strain} and ΔE_{el} by the Wynblatt-Chatain model with which v_i by Rickman's model is also compared.

4.5. Systematics of GB adsorption at 0K

At this point of description, there leaves only three parameters to specify a GB system according to the lattice gas GB model: ϕ_{seg}, v_i and z_v/z, by knowing which GB adsorption and energy as a function of T/T_C and $\Delta\mu/z\omega$ can be solved using Eq. (33) and (35). First, we focus only on the influence of ϕ_{seg} and leave v_i and z_v/z being fixed. The ground states of GB adsorptions at $T = 0$ *K* are analyzed, where exact analytical solutions can be obtained because the thermal energy (effects of mixing entropy) vanishes and GB compositions X_i equal to either 1 or 0. The resultant GB ground states are labeled by a quantum number $n = 0, 1, 2 \ldots$ which is number of layers fully occupied by solutes on one side of a GB, and the absorptions are $\Gamma = 2n$ because of symmetric GBs. The grand potentials for the n^{th} state can be derived from Eq. (33) as:

$$\overline{\Omega}^{(n)}(z\omega)^{-1} = 2z_v z^{-1} - \phi_{seg}\sum_{i=1}^{n} v_i - 2n(z\omega)^{-1}\Delta\mu \qquad (42)$$

where the superscript (n >1) is the quantum number of states and $\overline{\Omega}^{(0)} = 0$ for clean GB state. 0K GB absorption diagram as illustrated in Fig. 4.3 can be solved exactly from Eq. (42) by finding the GB state with minimum $\overline{\Omega}$ as a function of $\Delta\mu$ and ϕ_{seg}. Then GB systems are classified into three types according to their ϕ_{seg} value: strong segregation system (i.e. $\phi_{seg} = 1$), intermediate segregation system (i.e.

$\phi_{seg} = 0.6$) and weak segregation system (i.e. $\phi_{seg} = 0.3$). For strong segregation systems, GBs have a complete sequence of adsorption states from n = 0 to ∞ (∞ also represents the complete wetting condition), following which GBs transit from "clean" state to higher quantum state with the increase of $\Delta\mu$ and become complete wetting at coexistence. The transition between the n^{th} and $(n+1)^{th}$ states (which are noted as $\langle n \leftrightarrow n+1 \rangle$ transition in the rest of the text) occurs when $\overline{\Omega}^{(n)} = \overline{\Omega}^{(n+1)}$:

$$\begin{cases} \Delta\mu^{\langle 0\leftrightarrow 1\rangle}(\mathrm{z}\,\omega)^{-1} = z_v z^{-1} - \frac{1}{2}\phi_{seg} \\ \Delta\mu^{\langle \mathrm{n}\leftrightarrow \mathrm{n}+1\rangle}(\mathrm{z}\,\omega)^{-1} = -\frac{1}{2}\phi_{seg}\nu_{i+1} \end{cases} \tag{43}$$

$\Delta\mu^{\langle n\leftrightarrow n+1\rangle}$ increases with the decrease of ϕ_{seg} because GBs of weaker segregation strength requires more chemical driving force to form layered adsorptions. In lower ϕ_{seg} region, GB systems enters intermediate segregation strength region, which are distinguished by an incomplete layering transition sequence: [0, n, n+1… ∞] (n > 1). In such cases, the 0^{th} state transits to the n^{th} state directly (in the absence of the 1^{st} to $(n\text{-}1)^{th}$ states) if $\phi_{seg} < \phi_{seg}^{\langle 0\leftrightarrow n\rangle}$ where the subscript denotes the vanishing of 1^{st} to $(n\text{-}1)^{th}$ states. $\phi_{seg}^{\langle 0\leftrightarrow n\rangle}$ can be solved by letting $\overline{\Omega}^{(0)} = \overline{\Omega}^{(n-1)} = \overline{\Omega}^{(n)}$:

$$\phi_{seg}^{\langle 0\leftrightarrow n\rangle} = 2z_v z^{-1}\left[\sum_{i=1}^{n-1}\nu_i - (n-1)\nu_n\right]^{-1} \tag{44}$$

and the direct $\langle 0 \leftrightarrow n\rangle$ transition chemical potential can be solved from $\overline{\Omega}^{(0)} = \overline{\Omega}^{(n)}$ as:

$$\Delta\mu^{\langle 0\leftrightarrow n\rangle}(\mathrm{z}\,\omega)^{-1} \approx n^{-1}z_v z^{-1} - \frac{1}{2}n^{-1}\phi_{seg}\sum_{i=1}^{n}\nu_i \tag{45}$$

For weak segregation strength systems, GBs remain clean at all chemical potentials at 0K because the intrinsic driving force of segregation is too weak to drive the layered complexion states' formation. The occurrence of such condition should satisfy that $\overline{\Omega}^{(n)}\Big|_{n=1,2..\infty} > \overline{\Omega}^{(0)}$, therefore the critical value $\phi_{seg}^{\langle 0\leftrightarrow\infty\rangle}$ under which GB is clean at 0K can be solved by letting $\overline{\Omega}^{(\infty)}\Big|_{\Delta\mu=0} = 0$ as:

$$\phi_{seg}^{\langle 0\leftrightarrow\infty\rangle} = 2z_v z^{-1}\left(\sum_{i=1}^{\infty} v_i\right)^{-1} \tag{46}$$

4.6. Systematics of GB adsorption transitions at finite temperature

Using Wynblatt-Chatain model's formulism of GB potentials, we calculated GB adsorptions as a function of X_{bulk} and T for a strong segregation system with ϕ_{seg} =1 and a weak segregation system with ϕ_{seg} = 0.4 as shown in Fig. 4.4. In the calculation, we considered for a FCC (100) twist GB and employed eq. (37) as GB potential functional. For the modeled system's parameters, we use z = 12, z_v = 4 GB, P is set to be 5/6 to represent a "general GB" in the following calculation so that the GB energy is 1/3 of the surface energy for a pure element. GB potential decaying function is set to be:

$$v_i = f_{strain}\exp[-1.21(i-1)^{1.53}] \tag{47}$$

which is derived according to Friedel model using a hypothetic lattice constant 3.61 angstrom.

The strong segregation system inhabits the adsorption transition behaviors at 0 K showing three sequential layering adsorption transitions, which are

associated with sharp increases of GB absorptions, transitions to higher adsorption (i.e. 4^{th}) states are not shown for convenience in Fig. 4.4 because these transitions occur at the compositions very close to the edge of miscibility gap. These adsorption transitions are prewetting transitions, through which GBs become complete wetting at coexistence with the increase of X_{bulk}. The transition lines extend to critical temperatures T_{crit}, above which the first order adsorption transitions become continual. The transition behaviors in this case echo the prior Rickman's modeling work [47]. Unlike the strong segregation case possessing series of layered adsorption states, the weak segregation GB system only has one single thin-thick transition and the equilibrium adsorptions before and after the transition are not integral number of monolayers. Specifically, the transition line intersects with the miscibility gap at the wetting temperature $T_w \sim 0.4T_c$, below which GB is always clean at all composition while above which GB become complete wetting within the miscibility gap. Such transition behaviors are similar to the solid state prewetting/wetting phenomenon modeled by Wynblatt and Chatain [44] and also analogous to the Cahn's critical wetting model [46].

In Fig. 4.5, we further demonstrate a complete systematics of GB complexion transition using a 3-D type GB transition diagram constructed by combining series of calculated 2-D GB diagrams. In the 3-D diagram, GB transition hyper surfaces separating discrete adsorption states are plotted with the line of complete wetting and lines of critical points. With the 3-D GB transition diagram, a complete adsorption behaviors evolution map according to ϕ_{seg} variation can be

captured. For strong segregation systems with large ϕ_{seg} , i.e. ϕ_{seg} = 1, GB adsorption increases stepwisely with the increase of $\Delta\mu$ through layering transitions and the GB states have a complete sequence of quantum number. Also, GB is always wet at coexistence. With the decreasing of ϕ_{seg} , the $\langle 0 \leftrightarrow 1 \rangle$ transition lines shift towards the direction of $\Delta\mu$ increase and the stable region of 1st GB state shrinks and when $\phi_{seg} = \phi_{seg}^{\langle 1 \leftrightarrow 2 \rangle}$, the $\langle 0 \leftrightarrow 1 \rangle$ transition and the $\langle 1 \leftrightarrow 2 \rangle$ transition merges together to form a direct $\langle 0 \leftrightarrow 2 \rangle$ transition and 1st GB state is no longer stable. Correspondingly, at $\phi_{seg}^{\langle 0 \leftrightarrow 2 \rangle}$ which defines the onset of medium segregation strength system, the $\langle 1 \leftrightarrow 2 \rangle$ transition surface starts to intersect with the $\langle 0 \leftrightarrow 1 \rangle$ transition surface on the 3-D GB diagram. With further reduction of ϕ_{seg} , the 2nd GB state stable region shrinks until $\langle 0 \leftrightarrow 2 \rangle$ and $\langle 2 \leftrightarrow 3 \rangle$ transitions coalesce into a direct $\langle 0 \leftrightarrow 3 \rangle$ transition at $\phi_{seg} = \phi_{seg}^{\langle 0 \leftrightarrow 3 \rangle}$. When $\phi_{seg} < \phi_{seg}^{\langle 0 \leftrightarrow 3 \rangle}$, there is only one transition, which intersects with the coexistence boundary at T_w = 0K when $\phi_{seg} = \phi_{seg}^{\langle 0 \leftrightarrow \infty \rangle}$ where $\phi_{seg}^{\langle 0 \leftrightarrow \infty \rangle}$ defines the occurrence of weak segregation systems. Below $\phi_{seg}^{\langle 0 \leftrightarrow \infty \rangle}$, the GB adsorption behavior is analogous to the description of Cahn's theory of critical wetting and T_w raises with further reducing ϕ_{seg} . On the 3-D transition diagram, all transition lines shift towards lower $\Delta\mu$ at higher T suggesting that GB adsorption states' formation is driven by both thermal energy and chemical energy. Interestingly, all transitions' T_{crit} are weakly dependent on the variation of ϕ_{seg} as all $T_{crit}^{\langle 0 \leftrightarrow n \rangle}$ (n ≥ 1) are around 0.7T_m and all

$T_{crit}^{\langle n\leftrightarrow n+1\rangle}$ are close to 0.4T_m in these calculations. T_{crit} can be solved from Landau theory of phase transitions, which states that first order transition become second order if $\left(\frac{\partial^2\overline{\Omega}}{\partial\varphi^2}\right)\geq 0$ at transition point where φ is the order parameter. Let φ be Γ, we can solve T_{crit} approximately by letting $\min\left(\frac{\partial^2\overline{\Omega}}{\partial\Gamma^2}\right)\Big|_{T_{pwc}} = 0$ and assuming Γ ≈ 2[(n-1)+X_n] as:

$$\begin{cases} T_{crit}^{\langle 0\leftrightarrow n\rangle} \approx \left[1-z_v z^{-1}\right]T_c & (n=1) \\ T_{crit}^{\langle n\leftrightarrow n+1\rangle} \approx \left[1-2z_v z^{-1}\right]T_c & (n>1) \end{cases} \quad (48)$$

Based on Eq. (12), ϕ_{seg} =1 are estimated to be $T_{crit}^{\langle 0\leftrightarrow 1\rangle}$ = 0.67T_c and $T_{crit}^{\langle 1\leftrightarrow 2\rangle}$ = 0.33 T_c which are close to the numeric results shown in Fig. 4.6(b). With the obtained systematics of GB transition, the distinct observations of layering GB transition and prewetting/wetting GB transitions in prior studies [44, 47] can be well united into this coherent 3-D transition diagram with their major differences summarized into the variation of single factor ϕ_{seg}. We also note that the derived GB systematics is also analogous to the systematics of inert gas molecules' adsorption on the surfaces of attractive substrates [113].

4.7. More factors influencing the systematics of GB transitions

In the previous calculations, the broken bonds fraction P is fixed so ϕ_{seg} is determined by differential bonding energy (e_{aa} – e_{bb}) and strain energy ΔE_{el}. If we consider GBs in a certain binary system with fixed (e_{aa} – e_{bb}) and ΔE_{el}, the bonding

conditions of different GBs can also cause the variation of ϕ_{seg} hence result in the anisotropy of GB segregation. According to Wynblatt-Chatain model, the functional relation between twist angle $\Delta\theta$ and broken bond fraction *P* for a twisted (100) GB of FCC system is expressed as:

$$(1-P) \approx 0.18 \sin^{1/4}\left(2\Delta\theta\right) \tag{49}$$

and ΔE_{el} is also proportional to the GB free volume which is linear to broken bonds ratio:

$$\Delta E_{el}^{1} = \beta(1-P)\Delta E_{el}^{\infty} \tag{50}$$

where β is an adjustable proportionality constant and ΔE_{el}^{∞} is the total solute atom's strain energy in the bulk. Combining eq. (49) and (50) with eq (7s), ϕ_{seg} can be rewritten as a function of $\Delta\theta$ as Eq. (37). Eq. (37) shows that changing ϕ_{seg} by increasing twist angle $\Delta\theta$ is equivalent to increasing the sum of $(e_{BB} - e_{AA})$ and ΔE_{el}^{∞}. Fig. 4.8 and 4.9 compared GB complexion diagrams of at same ϕ_{seg} but different $\Delta\theta$, $(e_{BB} - e_{AA})$ and ΔE_{el}^{∞} which shows that all GB behaviors well follow the systematics of GB transitions as a function of ϕ_{seg} as discussed in the main text. Specifically, low $\Delta\theta$ and high $\left(e_{BB} - e_{AA}\right)$ or ΔE_{el}^{∞} GBs have the same GB diagram as high $\Delta\theta$ and low $\left(e_{BB} - e_{AA}\right)$ or ΔE_{el}^{∞} GBs when their ϕ_{seg} equal, suggesting that low misorientation GBs with strongly segregating solutes could have the same adsorption behavior as high misorientation GBs with weakly

segregating solute when two cases share the same ϕ_{seg}. Therefore, ϕ_{seg} is able to represent not only the intrinsic segregation tendency of solutes but also the effect of GB anisotropy.

In addition to ϕ_{seg}, the range of GB potential (which is characterized by the GB potential decaying function v_i) also influences the GB adsorption transition behaviors. In order to demonstrate the influence of GB potential range, we further compared two series of GB complexion diagrams derived using long range GB potential and short range GB potential separately. As shown in Fig. 4.10, the key characteristics of GB adsorption behaviors are similar as discussed previously. But with long range GB potential (larger v_i), the stable chemical potential window of 2nd and 3rd states are much wider than short range GB potential case (smaller v_i), in which only 2nd has a narrow stable region beside the coexistence line and no obvious stable region of the 3rd state can be observed. Such observation based on numeric results are consistent with Eq. (43)'s analytic description, implying that changing GB potential range (v_i) will only influence the transitions between $n \geq 1$ GB states.

Similar to v_i, z_v/z can also change the wetting temperature, transition chemical potential and roughing temperature as described by Eq. (43-47). In Fig. 4.8, GB complexion behaviors for GBs with different lattice structures are compared. Two cases were compared: the first case is (100) twisted GB in FCC with $z_v/z = 1/3$ and FCC and Cubic systems with $z_v/z = 1/6$. The transition line position and the transition critical temperatures are different for two cases. Such

difference is consistent with the analytic expressions derived in the main text which shows the quantitative relationship between z_v/z, ϕ_{seg},v_i, $\Delta\mu^{(transition)}$ and T_{crit}. But the general trend of GB transition systematics is independent of the choice of v_i, z_v/z that high ϕ_{seg} systems have series of layering transitions and low ϕ_{seg} systems adopt one prewetting transition. Therefore, ϕ_{seg} can be concluded as the dominant factor controlling the GB absorption behaviors in the lattice type GB systems.

4.8. Summary and conclusion.

In summary, using a lattice type Ising GB model, we examined the systematic transition behaviors of GBs. A normalized segregation strength ϕ_{seg} is introduced to represent the overall effects of strain, differential bonding energies, the misorientation of symmetrical twist boundaries as well as the mixing energy. By varying ϕ_{seg} , we constructed 3-D GB transition GB in three-dimensional spaces of the ϕ_{seg} , T/T_m and $\Delta\mu$. The 3-D transition diagram shows that strong segregation systems with large ϕ_{seg} undergoes series layering transitions while in weak segregation systems with a small ϕ_{seg} , the layering transitions merges into thin-thick (prewetting) transitions. Specifically, a series of analytic expressions are derived to quantitatively describe the transition as a function of ϕ_{seg} , T/T_m and $\Delta\mu$. Such systematics can also be practically useful, with which, real materials' GB transitions tendency can be predicted conveniently by estimating ϕ_{seg} quantitatively. For example, solutes with high cohesive energy difference and high

atomic size difference such as Ni-Bi, Cu-Bi, Cu-Ag systems have strong intrinsic segregation tendency and they adopt ϕ_{seg} > 1 typically for average GBs and expected to form layered GB complexions according to the 3-D GB diagrams. This is generally consistent with experiments observations and atomic modeling [31, 32, 52]. Additionally, the derived systematics of GB transitions is able to cover different GB adsorption behaviors studied in prior studies, also it exhibits phenomenological similarities to various the cases of multilayer adsorption of inert gas molecules on the surfaces of attractive substrates, enriches the classical GB segregation/adsorption theory.

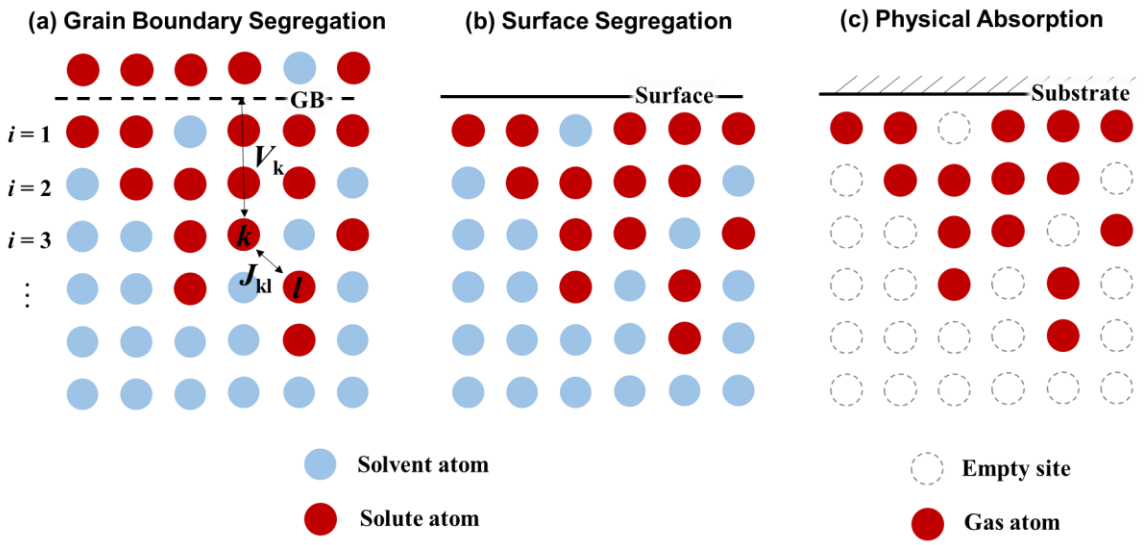

Figure 4.1 Schematics of the interface segregation and absorption modeled by lattice gas type model. V_k represents the interfacial potential, *k* and *l* are *k*th and *l*th lattice site with J_{kl} denoting the interaction between the two sites.

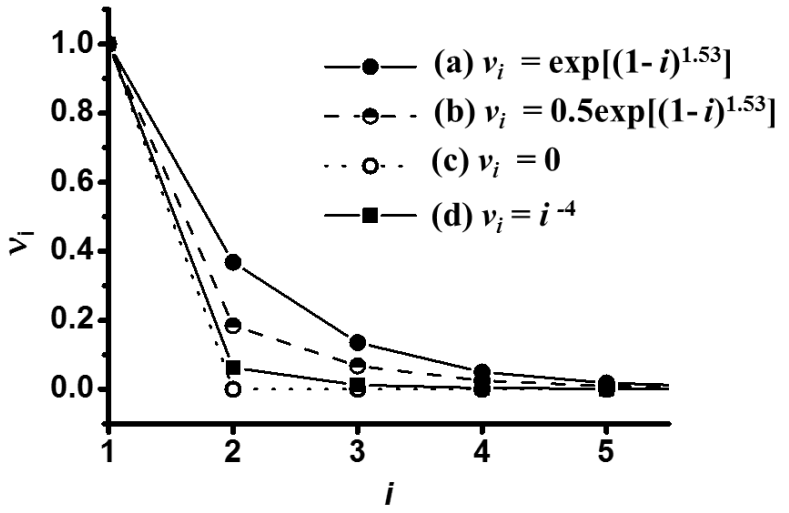

Figure 4.2 Comparison of GB potential decaying functions (v_i). Lines (a) to (c) correspond to the functional according to Wynblatt-Chatain model at different strain energy fraction (f_{strain} = 1, 0.5, 0) values and line (d) $v_i = i^{-4}$ is from Rickman's model.

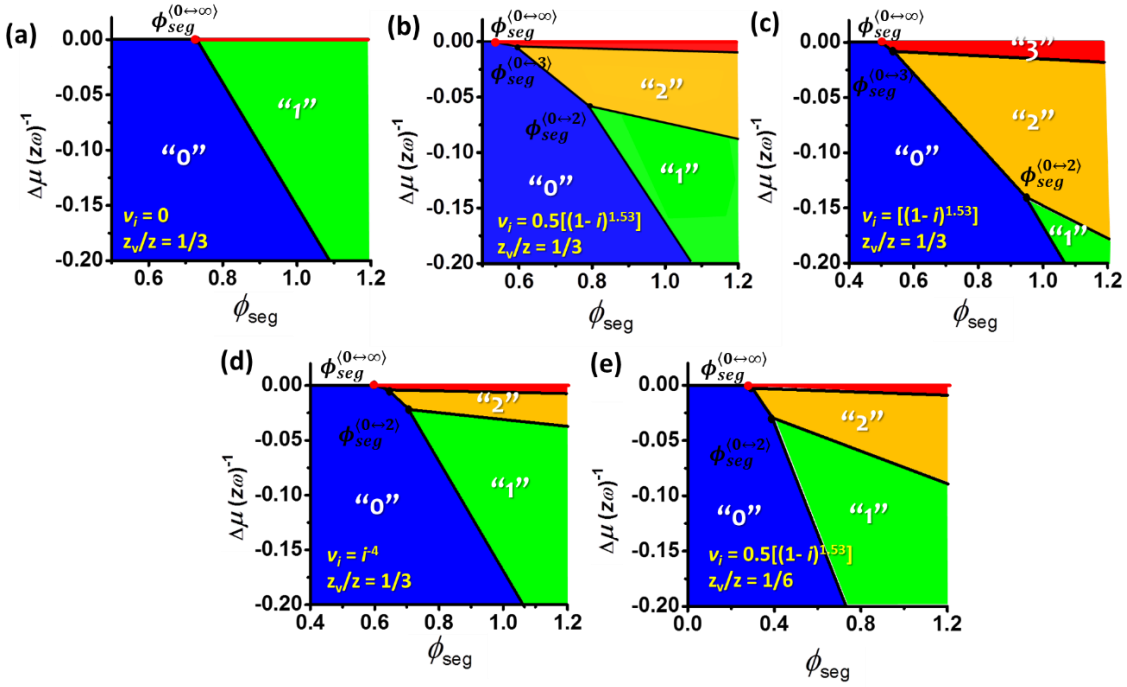

Figure 4.3 Comparison of complexion diagrams at $T \rightarrow 0$ K for GBs with different GB potential decaying functions v_i and out-layer bonds ratio z_v/z. The diagrams are shown in the axis of normalized segregation strength ϕ_{seg} and normalized chemical potential difference $\Delta\mu(z\omega)^{-1}$. n denotes the quantum number of GB complexion.

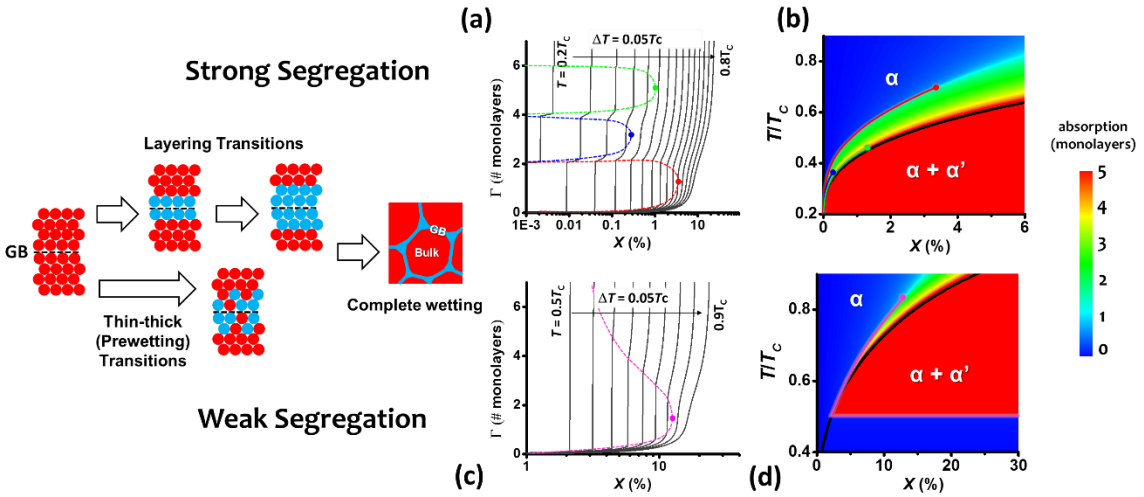

Figure 4.4 Comparison of calculated GB adsorption transitions for a typical strong (ϕ_{seg} = 1) and a typical weak segregation system (ϕ_{seg} = 0.4). In the calculation, the GB potential decaying functional is set as $v_i = 0.5\exp[-1.24(i\text{-}1)^{1.53}]$. The left panel is the schematics of GB adsorption state formation sequence upon increase bulk composition. (a) and (c) are the calculated absorption vs composition at different temperatures where the dash lines corresponding to the GB absorption states before and after GB transition. Those transitions become continual above the roughening temperature T_{crit} plotted with solid dots. (b) and (d) are the calculated absorption transition diagram at the axis of X and T, in which GB transition lines are illustrated with colored lines and bulk phase boundaries are drawn with black lines.

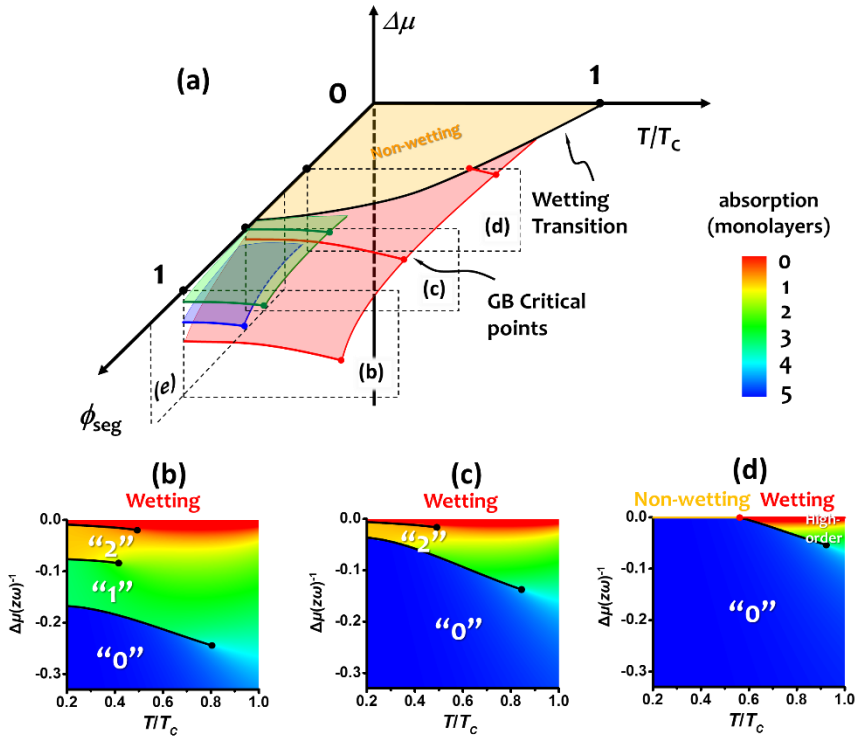

Figure 4.5 GB adsorption diagram in the axis of $\Delta\mu$, T, ϕ_{seg} assembled from serious of 2-D $\Delta\mu$, T, which is plotted with its cross-sections along the ϕ_{seg} axis. In the calculation, the GB potential decaying functional is set as $v_i = 0.5\exp[-1.24(i-1)^{1.53}]$. In (a), $\Delta\mu = 0$ plane at is the bulk coexistence boundary below which is solvent rich single phase domain, the three GB transition hyper surfaces are colored in red, blue and green to represent $\langle 0,1\rangle$, $\langle 1,2\rangle$ and $\langle 2,3\rangle$ transitions respectively and the edges of those transition surfaces plotted with colored lines correspond to the critical points of these transitions, near the origin is the nonwetting region within which GBs are always clean at all chemical potentials. (b-d) are the cross-sections of 3-D GB diagrams along ϕ_{seg} direction that correspond to the 2-D complexion diagrams of $\phi_{seg} = 1$, $\phi_{seg} = 0.7$, $\phi_{seg} = 0.3$ respectively. (e) is the 0 K cross section of 3-D GB diagram that is already demonstrated in Figure. 4.2.

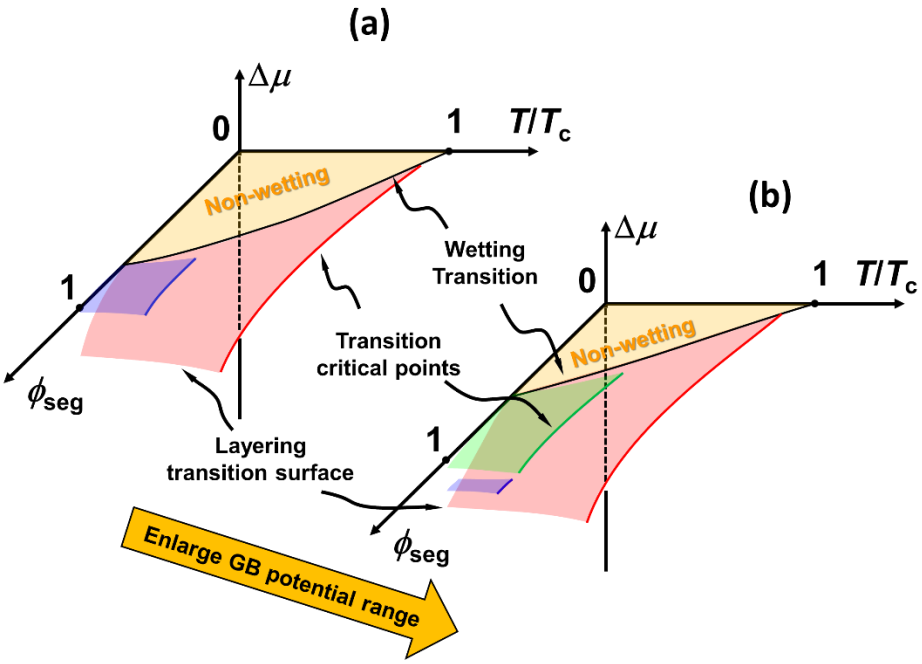

Figure 4.6 Comparison of 3-D GB diagrams of same ϕ_{seg} systems with different GB potential range (which is controlled by GB potential decaying functional v_i). Change of the GB potential range is realized by varying factor f in $v_i = f\exp[-1.24(i-1)^{1.53}]$. (a) is the case with $f = 0$ where GB potential is limited to only the nearest GB layer, (b) is the case with $f = 1$ (please refer to Fig. 3a for f = 0.5).

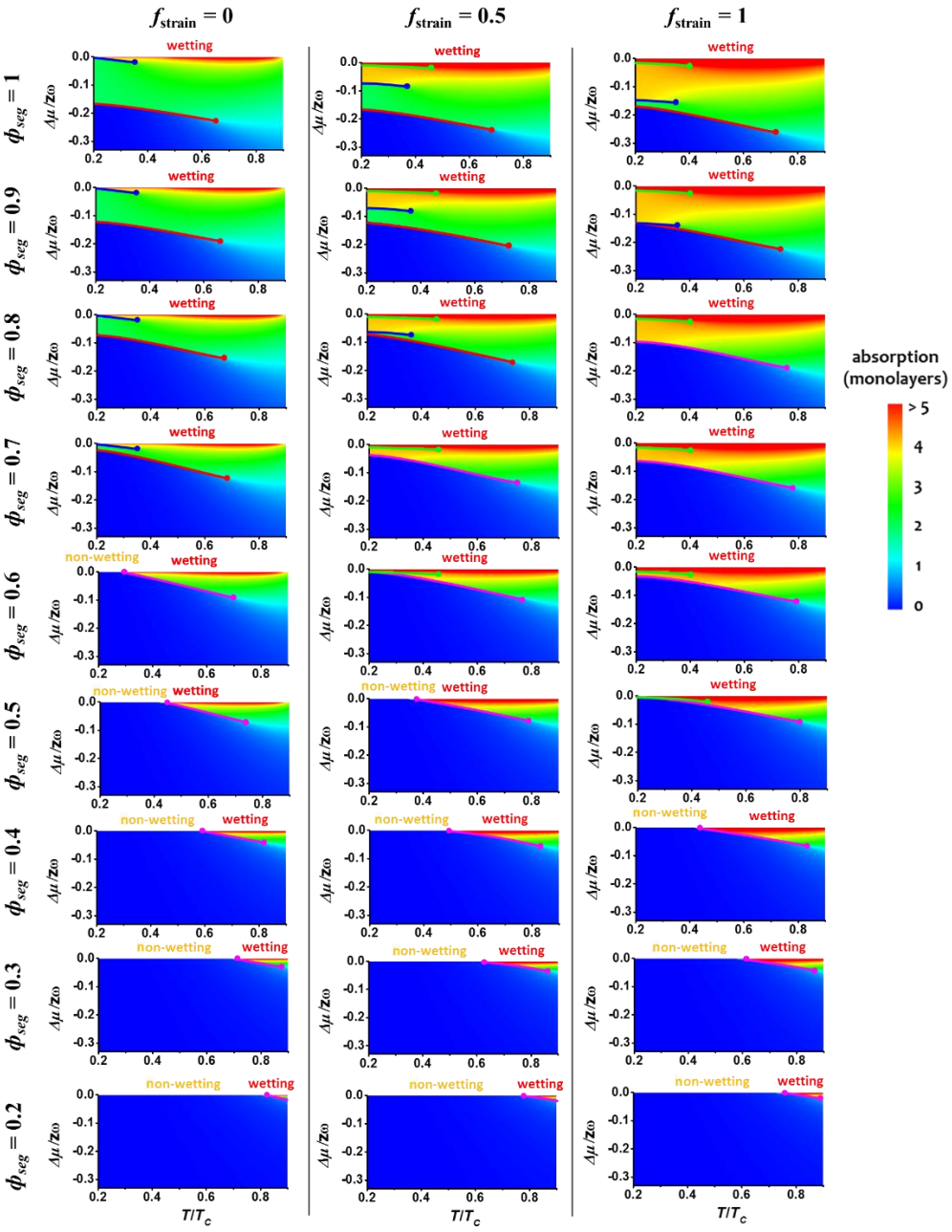

Figure 4.7 Comparison of computed GB complexion diagrams for normalized segregation strength (ϕ_{seg} from 0.2 to 1) where segregation is driven by different solute strain energy fraction (f_{strain} = 0, 0.5 and 1).

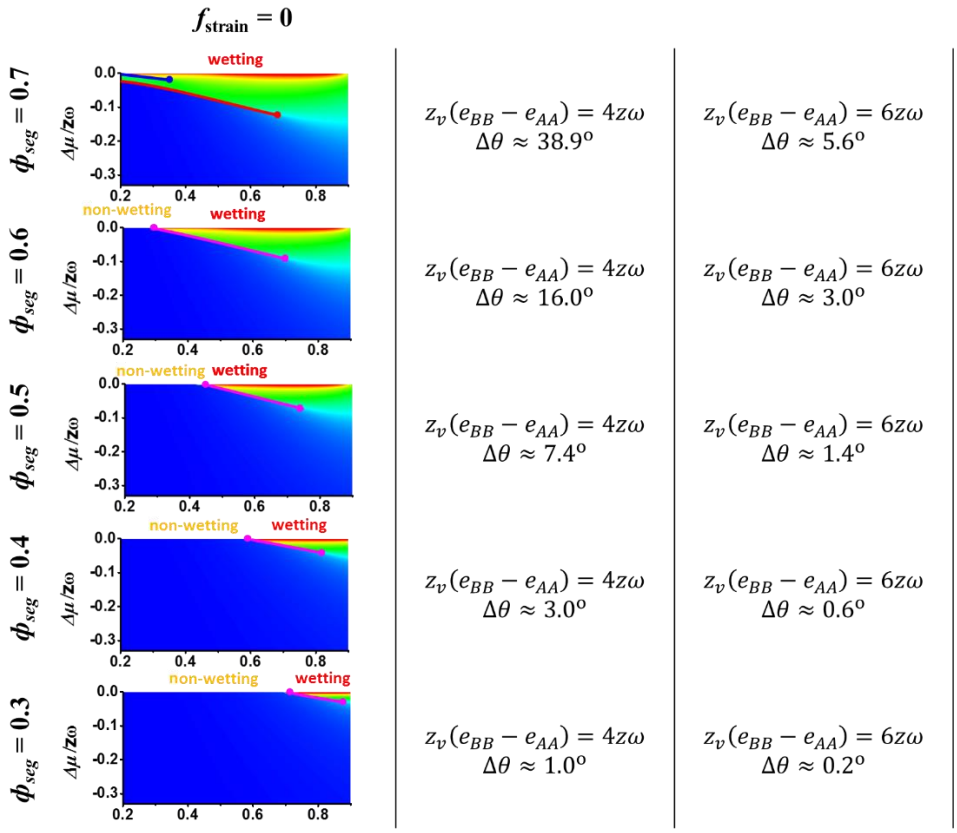

Figure 4.8 GB diagrams shared by two different cases: one has low misorientation angles $\Delta\theta$ and high differential bonding energy Δe_{ii} (e_{bb}- e_{aa} = 6$z\omega$/z_v), while the other has high $\Delta\theta$ but low Δe_{ii} (e_{bb}- e_{aa} = 4$z\omega$/z_v).

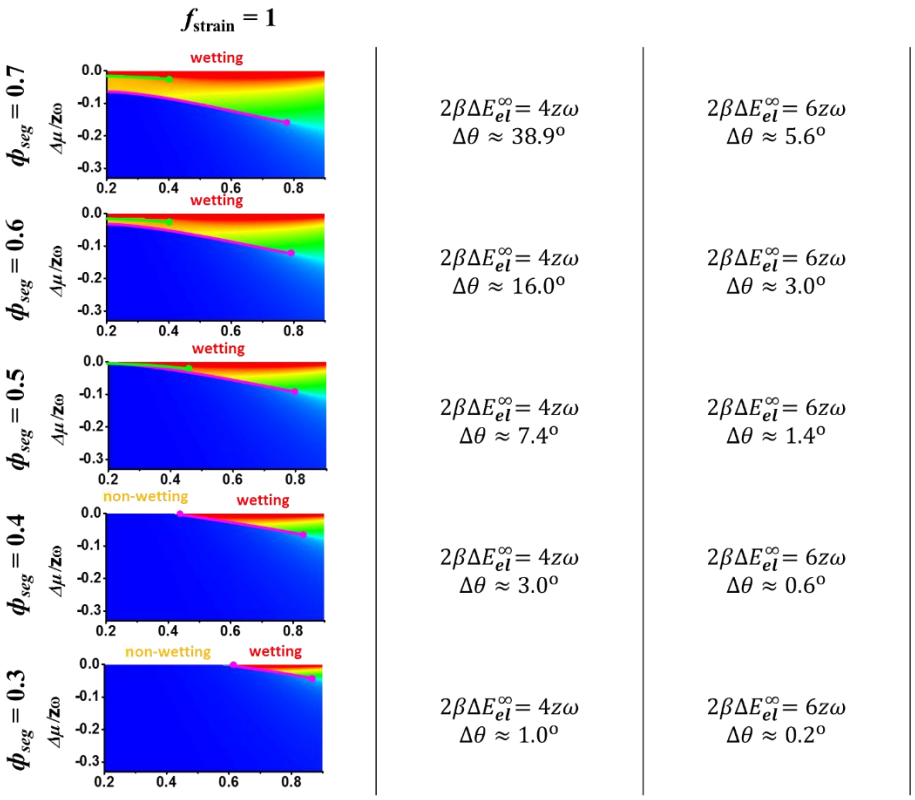

Figure 4.9 GB diagrams shared by two different cases: one has low misorientation angles $\Delta\theta$ and high solute strain energy ΔE_{el}^{∞} ($\beta\Delta E_{el}^{\infty} = 3z\omega/z_v$), while the other has high $\Delta\theta$ but low ΔE_{el}^{∞} ($\beta\Delta E_{el}^{\infty} = 2z\omega/z_v$).

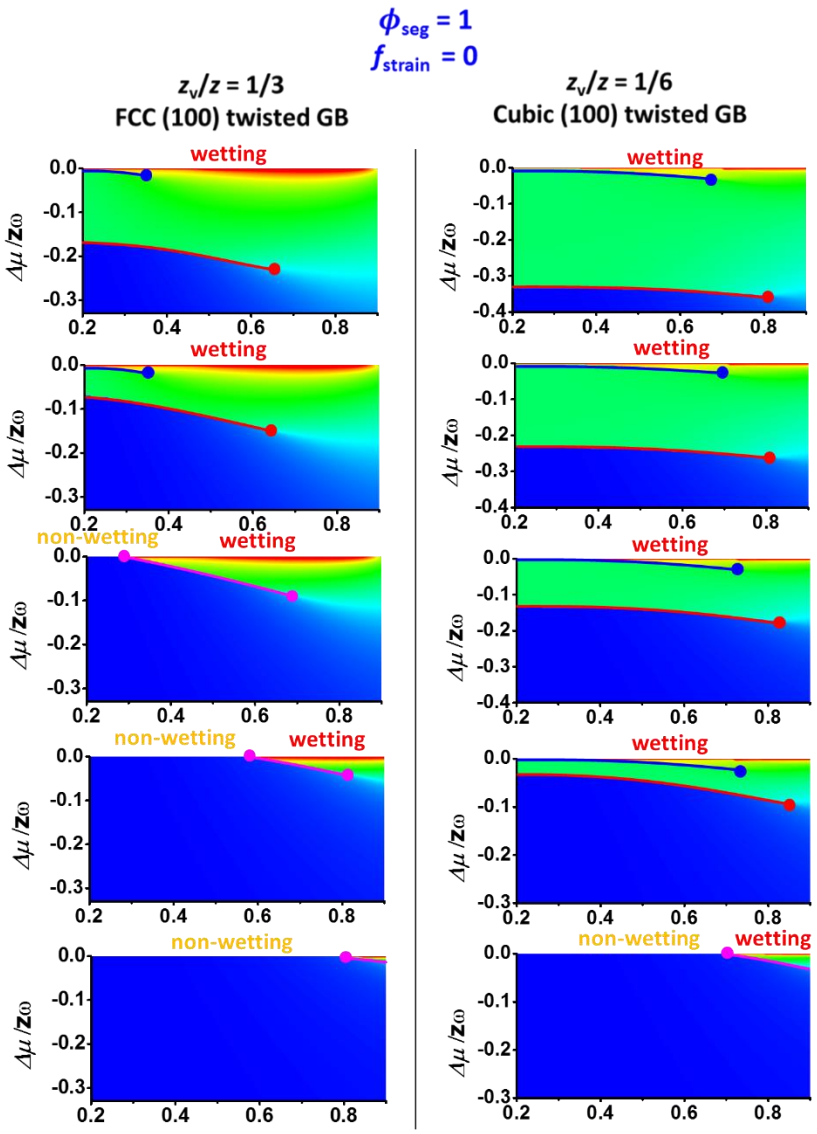

Figure 4.10 Calculated GB complexion diagrams for different GB structures which correspond to different out-layer bond ratio (z_v/z).

Table 4.1 Comparison of key parameters adopted by different lattice type GB models

	z_v/z	ω	i_{max}	v_i
Mclean[54]	0	0	=1	/
Fowler-Guggenheim[112]	0	$\neq 0$	=1	/
Wynblatt-Ku[45, 115]	> 0	$\neq 0$	=1	/
Wynblatt-Chatain[44]	> 0	$\neq 0$	> 1	$f\exp[A(1-i)^{1.53}]$ *
The Rickman[47]	1/6	$\neq 0$	> 1	i^{-4}

z_v/z is the ratio of bonds connecting one adjacent layer divided by total coordinates. ω is the regular solution parameter. i_{max} is the farthest GB layer sequence considered by the model. v is the GB potential decaying function.

* f and A are constants which can be quantified from lattice geometry and strain energy fraction at GB potential. Exact expression can be found in ref. [44, 55]

Chapter 5. Stabilization of Nanocrystalline Alloys at High Temperatures via Utilizing High-Entropy GB Complexions

Bulk computational thermodynamics are extended to model binary poly/nanocrystalline alloys by incorporating GB energies computed by a multilayer adsorption model. A new kind of stability diagram for equilibrium-grain-size poly/nanocrystalline alloys is developed. Computed results for Zr-doped Fe are validated by prior experiments and provide new physical insights regarding stabilization of nanoalloys and its relation to solid-state amorphization. This work supports a major scientific goal of extending bulk computational thermodynamics methods to interfaces and nanomaterials and developing relevant thermodynamic stability diagrams as extensions to bulk phase diagrams, which can be useful new tools for the “Materials Genome” initiative.

5.1. Introduction

In 1993, Weissmüller [116, 117] reported a theory of thermodynamic stabilization of nanocrystalline alloys, and this theory was further elaborated by Kirchheim *et al.*[64, 118]. It was proposed that the thermodynamic driving force for grain growth can be reduced by reducing GB energy (γ_{GB}) via GB segregation (*a.k.a.* adsorption). A nanocrystalline alloy can be stabilized as the effective γ_{GB} approaches zero. Subsequent experiments have been conducted to seek for stabilized nanocrystalline alloys in Fe-Zr [66, 119], Pd-Zr [120], and other systems [121-123]. In these systems, the “stable” nanocrystalline alloys typically represent *metastable states* in supersaturated regions occurring when precipitation is

hindered kinetically; this is consistent with Kirchheim's analysis [64]. Recently, Schuh and co-workers developed a "Regular Nanocrystalline Alloy" model and analyzed systems with positive pair-interaction parameters [59, 62, 124]. Saber *et al.* refined this model by incorporating both chemical and elastic segregation enthalpies [125], which was also an extension of their earlier model of ferrous alloys [126]; both models used a simplified monolayer/bilayer version of the Wynblatt-Ku type segregation formulism [45]. This work further combines CALPHAD analysis with a more realistic Wynblatt-Chatain type multilayer segregation (complexion) model [45] to simulate stable, metastable and unstable regions of polycrystalline binary alloys systematically for multiple phase fields, providing new quantitative insights regarding the competitions and underlying relations among precipitation, stabilization of nanoalloys, and solid-state amorphization.

A further scientific goal of this study is to develop new thermodynamic stability diagrams (as extensions to bulk phase diagrams) as novel materials design tools. In a boarder content, phase diagrams, along with CALPHAD methods [127], are arguably amongst the most useful tools for materials design. It is now well-established that the thermodynamic stability of an interface or a nanoscale system that has a large amount of interfaces can drastically differ from that of a bulk material. As an example, nanoparticles can often melt at hundreds of degrees below the bulk melting temperature [128]; along this line, Tanaka *et al.* extended CALPHAD methods to compute phase diagrams for nanoparticles of binary alloys [129, 130]. In another relevant study, researchers demonstrated that nanometer-

thick, impurity-based, liquid-like films can be stabilized at grain boundaries (GBs) well below the bulk solidus lines [6, 8, 10]; further studies extended the bulk CALPHAD methods to predict the stability of such liquid-like intergranular films (which can be considered as an “interfacial phase” and named as “complexion” to differentiate them from bulk phases [2, 4, 26, 27, 31, 131]) and such GB diagrams are proven useful for forecasting activated sintering and designing sintering protocols [7, 29, 36, 37]. This series of recent studies collectively point us to a potentially-transformative research direction of extending bulk CALPHAD methods to interfaces and nanomaterials with a large amount of interfaces; some research efforts in this area are also reviewed by Kaptay [132]. This work represents another such new endeavor of modeling equilibrium-grain-size poly/nanocrystalline alloys by incorporating GB energies in thermodynamic modeling.

It is important to differentiate two possible types of thermodynamic stability diagrams that may be developed for nanomaterials. The first type of diagrams represent the shrifts in phase boundaries given a constraint of artificially-fixed sizes (*e.g.*, particle or grain sizes); Tanaka *et al.*’s studies of binary nanoparticles [129, 130] belong to this type. The current study aims to develop the second type of stability diagrams to model the thermodynamic stability of equilibrium-grain-size poly/nanocrystalline alloys without imposing pre-selected (kinetically-determined) grain sizes. Fe-Zr is selected as our modeling system because the existence both thermodynamic data [133] and experimental results [66, 119, 134], and our goal is to develop models and methods that can be extended to other systems. In the current (first) study, we model a binary poly/nanocrystalline alloy (of equiaxed

grains) for which experimental data exist for validation; our ultimate goal is further extend the methods to multicomponent alloys, where they can have more impacts (similar to bulk CALPHAD methods).

5.2. Modeling methods

At constant pressure and temperature, the molar free energy of a polycrystalline binary alloy A-B (A = Fe and B = Zr for our specific case) can be written as:

$$G_m = (1 - X)\mu_A + X\mu_B + \overline{A_{GB}}\gamma_{GB}, \quad (51)$$

where X is the overall composition (atomic fraction) of the solute B, μ_A and μ_B are chemical potentials, $\overline{A_{GB}}$ is the GB area per mole of atoms, and γ_{GB} is the GB energy. When the grain size is small, the overall composition (X) differs from the bulk/crystal composition (X_C, inside the grain) because of GB segregation; the mass conservation law specifies:

$$X \approx X_C + \overline{A_{GB}}\Gamma\ , \quad (52)$$

where Γ is the GB excess of solute. Recent observations of the increased apparent solubility of dopants in nanocrystalline ZnO [135] and steels [136, 137] is likely due to that X can be substantially greater than X_C for nano-grained materials. Under the condition of a kinetically-limited (fixed) grain size, the changed solubility can also be partially related a shift in the X_C value (in equilibrium with the secondary phase) due to the added $\overline{A_{GB}}\gamma_{GB}$ term in Eq. (52); this effect should be modeled by the first type of stability diagrams (with per-selected grain sizes) discussed above, which is beyond the scope of this letter.

In this study, we adapt the Wynblatt-Chatain multilayer segregation (complexion) model [45] to consider general twist GBs in a BCC alloy which was described by Eq. (26) and Eq. (27) in Chapter 1 and 3; we assume J_{max} = 1 or all broken bonds exist in the first layer since we adopt a general twist (110) GB to represent the general GBs in Fe. The calculation parameters are set as: e_{FeFe} = -1.07 eV/bond and e_{ZrZr} = -1.56 eV/bond, which are estimated from atomization enthalpies [138]; the energetic difference between the HCP and BCC phase for Zr is corrected by using CalPhaD data [133]), $\omega[\equiv e_{AB} - 0.5(e_{AA} + e_{BB})]$ is the pair-interaction parameter (estimated to be -0.025 eV/bond for Fe-Zr from the CalPhaD data [133]), z is the total coordinate number (z = 8 for BCC), z_v is the coordination number above the plane (z_v = 2 for a BCC twist (110) GB), p (the fraction of reconnected bonds) is set to be 5/6 to represent a "general GB" so that the GB energy is 1/3 of the surface energy for a pure element, the elastic energy in the i-th layer is expressed as: $\Delta E_{els}^{i} = \Delta E_{els}^{1} \exp\left[-1.01\left(h^i/r_B\right)^{1.53}\right]$, where h^i is the distance to the GB core and r_B is the atomic radius of B; ΔE_{els}^{1} is given by the Friedel model [45], which is calculated to be 0.96 eV/atom for Fe-Zr. The equilibrium GB adsorption profile can be obtained using Eq. (27). Eq. (27) along with the adsorption profile $(X_{GB}^{i})_{i = 1, 2, \ldots}$ that minimizes Eq. (26), can be solved efficiently via an iterative method. The GB excess of solute is given by: $\Gamma \approx 2N \sum_i (X_{GB}^{i} - X_C)$.

5.3. Results and discussion

Fig. 5.1 shows several computed normalized GB energy ($\gamma_{GB}/\gamma_{GB}^{(0)}$) and GB excess of solute (Γ) vs. bulk composition (X_C) curves. Here, $\gamma_{GB}^{(0)}$, the GB energy for pure Fe, is computed from Eq. (26) to be ~1 J/m^2, which is consistent with the measured value [139]. In a binary alloy, GB adsorption reduces GB energy according to the Gibbs isothermal: $d\gamma_{GB} = -\Gamma_A d\mu_A - \Gamma_B d\mu_B \approx -\Gamma d(\mu_B - \mu_A)$. The double lines in Fig. 5.1 and Fig. 5.2 represent metastable states ($X_C > X_{soluvs}$) occurring when the precipitation is hindered.

We use X^*, Γ^*, μ_A^*, and μ_B^* to denote the conditions that the effective γ_{GB} is reduced to zero, which are labeled by the open crosses in Fig. 5.1 and Fig. 5.2. Beyond this point ($X_C > X^*$), a negative γ_{GB} represents an unstable state (indicated by dotted lines in Fig. 5.1 and Fig. 5.2), which should lead to a spontaneous increase in the GB area ($\overline{A_{GB}}$) with solute segregation that decreases X_C to a fixed value of X^* for a closed system. Consequently, an *equilibrium* grain size can be achieved with the effective γ_{GB} being kept at ~ 0 [64, 118, 121]. This equilibrium grain size can be estimated by plugging X^* and Γ^* into Eq. (26) and adopting an approximation for grain size for equiaxed grains ($d \approx 3\bar{V}/\overline{A_{GB}}$, where $\bar{V}$ is the molar volume), as:

$$d_{eq} \approx \frac{3\bar{V}\cdot\Gamma^*}{X - X^*} \tag{53}$$

Rewriting Eq. (53) for the polycrystalline alloy with an equilibrium grain size ($\gamma_{GB} = 0$) produces:

$$\bar{G}_{eq.\ grain\ size} = (1 - X)\mu_A^* + X\mu_B^*. \tag{54}$$

The free-energy curve for this equilibrium-grain-size alloy is represented by the

purple double line in Fig. 5.2, which is a tangent line that touches the free-energy curve of the A-rich α phase at X^*; with increasing X, this alloy exhibits a decreasing equilibrium grain size (proportional to $1/(X - X^*)$) and this line ends at an solid-state amorphization limit, which corresponds to the condition that d_{eq} approaches the atomic size.

In this study, we combine the Wynblatt-Chatain multilayer GB segregation (complexion) model [45] with an analysis for the Fe-Zr binary system [133]. To systematically represent the computed results, we plot lines of constant normalized GB energies and equilibrium grain sizes in the bulk phase diagram in Fig. 5.3 for the Zr-doped Fe system.

As shown in Fig. 5.3, GB segregation reduces γ_{GB} (the driving force of grain growth) systematically. Beyond the solvus line, γ_{GB} can be further reduced if the precipitation of the secondary phase ($Fe_{23}Zr_6$ *etc.*) is kinetically hindered; these metastable states are represented by dashed lines in Fig. 5.3. The effective γ_{GB} vanishes at $X = X^*$ ($\approx$ 0.002 at. % at ~600 K and $\approx$ 0.2 at. % at $T_{eutectoid}$, respectively, as shown in Fig. 5.3). Beyond this line, a metastable polycrystalline alloy with an equilibrium grain size has lower energies than the unstable BCC phase (as schematically illustrated in Fig. 5.2), and computed equilibrium grain sizes (using Eq. (54)) are plotted in Fig. 5.3. For a strong segregation system (like Fe-Zr) where X^* is small and Γ^* is almost a constant (Fig. 5.1), the temperature-dependence of d_{eq} becomes insignificant in the nano region (d_{eq} < 100 nm) according to Eq. (5); a more significant temperature-dependence is expected for a weaker segregation system. We should emphasize that these dashed lines in Fig. 5.3 only represent

the metastable states under the conditions that the precipitation is hindered; if the precipitation of $Fe_{23}Zr_6$ is allowed, the three horizontal lines in the two-phase region of Fig. 5.3 represent the true equilibrium states.

The bulk phase diagram shown in Fig. 5.3 was computed using the bulk CALPHAD data from Ref. [133]. In this case, there is no shrift in the bulk phase boundaries at the thermodynamic equilibria (because the equilibrium grain size is infinity at all equilibrium bulk phase boundaries. It is important to note that this case is different from prior studies of modeling nanoparticles with pre-selected particle sizes [129, 130].

The computed Fig. 5.3 compares favorably with two independent sets of prior experiments. Darling *et al.* reported that a Fe + 4 at. % Zr alloy made by high-energy ball milling exhibited a “stable” XRD grain size of 20-30 nm after annealing at 800 °C [66]; later they also showed that a TEM grain size of ~52 nm was retained in a ball milled Fe + 4 at. % Zr nanoalloy after annealing at 900 °C [119]. This is consistent with the computed result of ~ 30 nm at this condition (Fig. 5.3). The computed Fig. 5.3 also suggests an amorphization limit at ~ 50 % of Zr. This is also consistent with the solid-state amorphization of $Fe_{50}Zr_{50}$ multilayers reported in another prior study [140]; this agreement not only supports our model but also reveals the underlying relation between two phenomena – stabilization of nanocryalline alloys and solid-state amorphization – both occurring in the Fe-Zr system only if the precipitation is kinetically hindered (even though we recognize the existence of a more accurate model for solid-state amorphization [134]).

5.4. Conclusions

In summary, we have extended bulk computational thermodynamic methods to model binary equilibrium-grain-size poly/nanocrystalline alloys by incorporating GB energies computed by a Wynblatt-Chatain multilayer GB complexion model [45]. This letter also reports a framework to combine a bulk CALPHAD analysis with a GB segregation (complexion) model using an explicit (simple) approach. In future studies, new interfacial thermodynamic models that consider complex GB complexions [2, 4, 26, 27, 31, 131] beyond the classical GB segregation types can be further developed and incorporated. A key contribution of the current study is the development of a new kind of thermodynamic stability diagrams equilibrium-grain-size alloys. In particular, a new stability diagram is computed for Zr-doped Fe (as our model system) and validated with multiple prior experiments. In addition to earlier studies of developing phase diagrams for binary nanoparticles [6, 8, 10] and GB diagrams [7, 29, 36, 37], the success of this study represents a further step towards realizing a major scientific goal of developing stability diagrams for interfaces and nanoscale systems as extensions of bulk phase diagrams, which can be used as general tools to accelerate materials design in the spirit of the Materials Genome initiative.

Chapter 5, in part, is a reprint of the material "Developing thermodynamic stability diagrams for equilibrium-grain-size binary alloys" as it appears in Materials Letters, Naixie Zhou and Jian Luo, 2014, 115, 268-271. The dissertation author was the primary investigator and author of this paper. All calculations and data analysis were performed by the author.

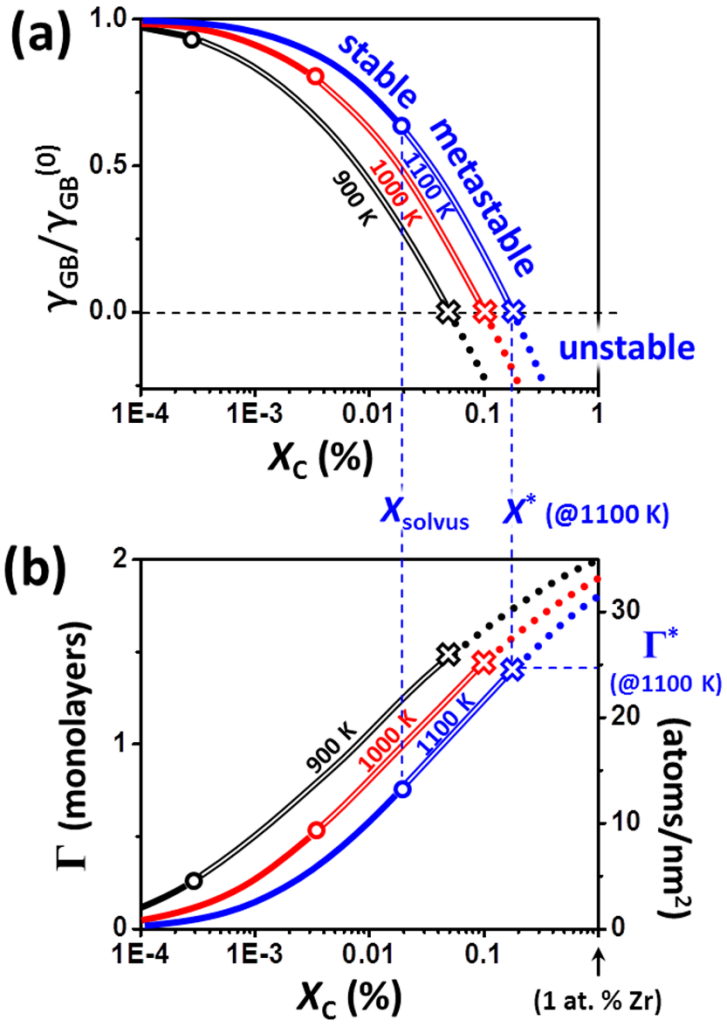

Figure 5.1 Computed (a) normalized GB energy ($\gamma_{GB}/\gamma_{GB}^{(0)}$) and (b) GB excess of the solute (Γ) vs. bulk composition (X_C) curves for Zr-doped Fe. The stable, metastable, and unstable regions, respectively, are represented by the solid, double, and dotted lines, respectively.

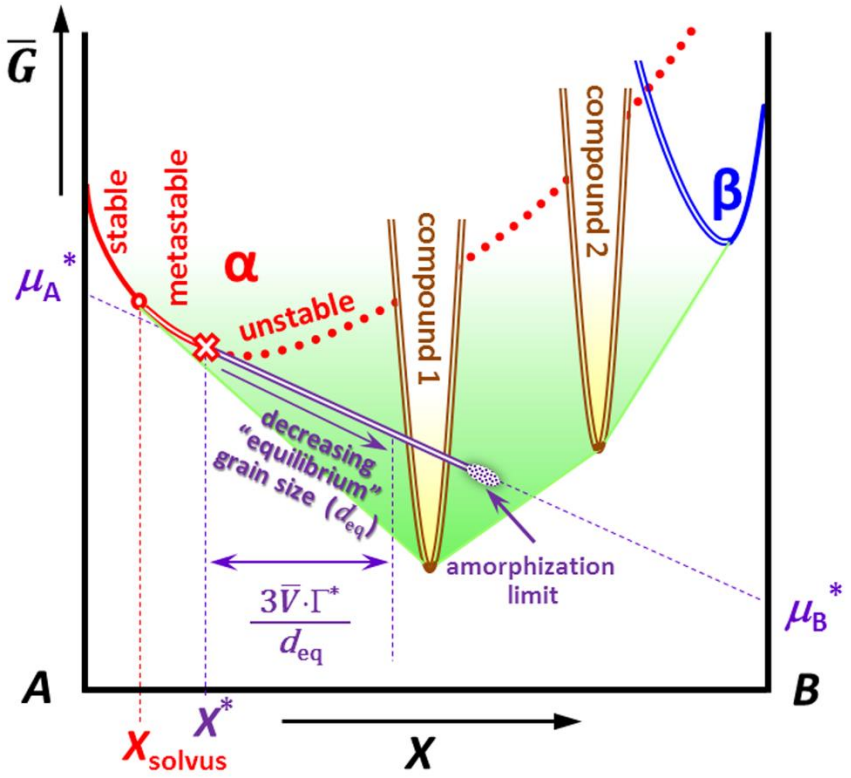

Figure 5.2 Schematic illustration of molar free energy vs. composition curves for a binary A-B alloy. If the precipitation of the B-enriched secondary phase(s) is kinetically hindered, a metastable α phase can form at X > X solvue (represented by the red double line); the metastable α phase becomes unstable at $X > X^*$ (represented by the red dotted line); in this region, a metastable polycrystalline alloy will form with an "equilibrium" grain size (d_{eq}), which is represented by a tangent line that starts at $X = X^*$; for this equilibrium-grain-size alloy, d_{eq} is inversely proportional to $(X - X^*)$, and this line ends at an amorphization limit when d_{eq} approaches the atomic size.

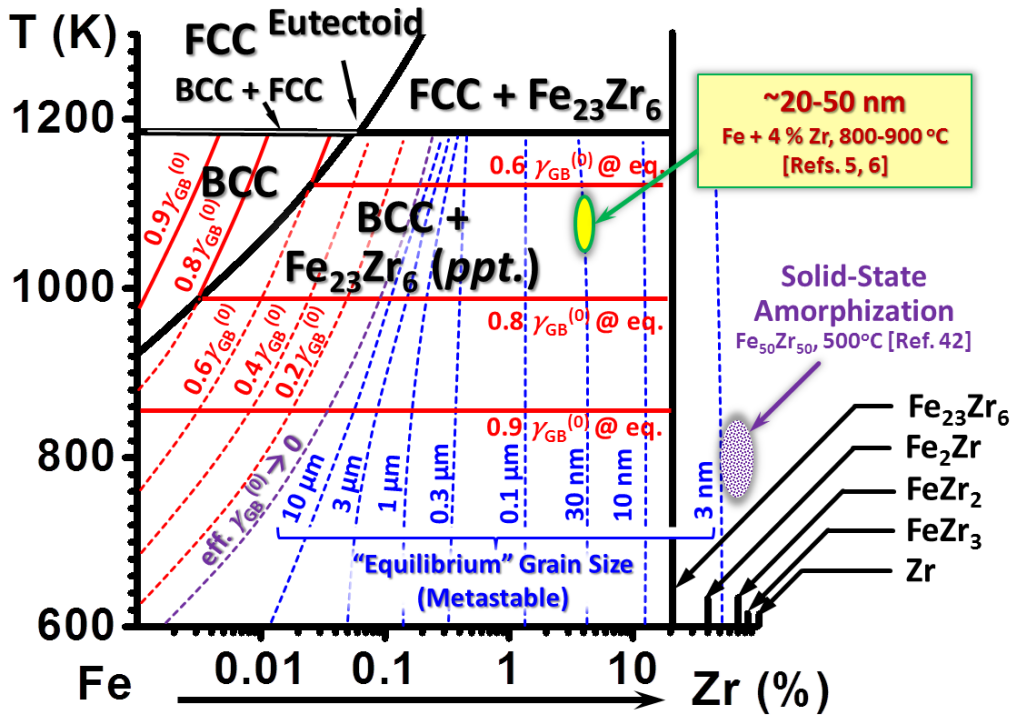

Figure 5.3 Computed lines of constant normalized GB energies and *equilibrium* grain sizes are plotted in the bulk phase diagram of Fe-Zr; the *x*-axis is logarithmical overall composition (atomic percentage of Zr) and only two phase fields are completely shown. The equilibrium states are represented by solid lines and the metastable states are represented by dashed lines. The bulk phase diagram was also computed; the BCC and FCC two-phase region is very narrow so that the two phase boundary lines appear to overlap at this scale. Noting that the composition is plotted in logarithmical scale so that the computed solvus line intersects with (instead of asymptotically approaching) the temperature axis.

Chapter 6. Developing Thermodynamic Stability Diagrams for Equilibrium-Grain-Size Binary Alloys

Multicomponent alloying can be utilized to enhance the thermal stability of nanocrystalline alloys. The GB energy can be reduced significantly via both bulk and grain-boundary high-entropy effects with increasing temperature at/within the solid solubility limit, thereby reducing the thermodynamic driving force for grain growth. Moreover, GB migration can be hindered by sluggish kinetics. To test these new theories, numerical experiments were conducted; subsequently, several nanoalloys, including a Ni-based alloy ($Ni_{80}Mo_{6.6}Ti_6Nb_6Ta_{1.4}$) and Ni-containing high-entropy alloys ($Ni_{29}Fe_{23}Co_{23}Cr_{23}Zr_2$ and $Ni_{25}Fe_{23}Co_{23}Cr_{23}Mo_2Nb_2Zr_2$), were designed and fabricated to demonstrate outstanding thermal stabilities that outperform the Ni-based binary nanocrystalline alloys.

6.1. Introduction

Although nanocrystalline metals can exhibit superior properties such as high strength and hardness [141-144], their applications are often hindered by the extreme susceptibility to grain growth. For example, nanocrystalline Al, Sn, Pb, and Mg are subjected to grain growth even at room temperature [145-147]. There are two general approaches to stabilize nanocrystalline materials against grain growth [121, 122, 148, 149]. First, kinetic stabilization by the solute-drag effects and/or Zener (particle) pinning can slow down GB (GB) migration [150-152], which become less effective at high temperatures. Second, thermodynamic stabilization

can be achieved by reducing the GB energy (γ_{GB}) via solute segregation (*a.k.a.*GB adsorption) to reduce the thermodynamic driving force for grain growth. Specifically, Weismuller originally proposed that an “equilibrium” grain size can be reached when the effective γ_{GB} vanishes [60, 61]. Yet, Kirchheim [64] showed that the equilibrium-grain-size binary nanocrystalline alloys generally represent metastable states in supersaturated regions if (and only if) the precipitation is hindered kinetically. In such cases, the kinetic inhibition of the precipitation also becomes more difficult with increasing temperature, triggering abrupt grain growth. These challenges motivate the present study to develop and test new theories and strategies to enhance the thermal stability of nanocrystalline alloys at high temperatures via utilizing high-entropy GB complexions (where the term “complexion” refers to an interfacial “phase” that is thermodynamically two-dimensional [3]).

Experimentally, stabilization of nanocrystalline alloys (nanoalloys) have been achieved in several binary systems, including Pd-Zr [73], W-Ti [59], Fe-Zr [65, 66], and Cu-Zr [153] (where the primary phases are underlined). Li *et al.* also showed that addition of 1-4 at.% Hf could further enhance the thermal stability of the binary Fe-Zr alloys [72]. Specifically, an electrodeposited $Ni_{79}W_{21}$ nanoalloy was found to be stable up to 600-700 °C [154], which represents the best reported result for Ni-based nanoalloys. To test the proposed new strategies, this study demonstrated the stabilities of a Ni-based alloy ($Ni_{80}Mo_{6.6}Ti_6Nb_6Ta_{1.4}$) and two Ni-containing high-entropy alloys ($Ni_{29}Fe_{23}Co_{23}Cr_{23}Zr_2$ and

$Ni_{25}Fe_{23}Co_{23}Cr_{23}Mo_2Nb_2Zr_2$) up to ~1000 °C, representing a noteworthy improvement from the binary Ni-based nanoalloys reported previously.

6.2. High entropy effect on GB energy reduction

The Gibbs adsorption theory states:

$$d\gamma_{GB} = S^{XS}dT - \sum_i \Gamma_i d\mu_i \quad (55)$$

where S^{XS} (entropy) and Γ_i (adsorption) are the GB excess quantities, T is temperature, and μ_i is the chemical potential of the i-th element. Eq. (55) implies that the GB energy (γ_{GB}) can be reduced by segregation at a constant T and this effect can be enhanced for multicomponent (high-entropy) GBs under certain conditions. We should note that generally $\left(\partial\gamma_{GB}/\partial T\right)_{P,X_i} > 0$ for a specimen of a constant bulk composition (X^i_{Bulk}) due to thermally-induced desorption. We propose that a high-entropy GB effect can be achieved for a saturated specimen (in equilibrium with precipitates), when the bulk composition moves long the solvus line, where the solutes' bulk chemical potentials are pinned by the precipitates so that $\left(\partial\gamma_{GB}/\partial T\right)_{P,\, X^i_{Bulk}\ \text{on solvus}} \approx \left(\partial\gamma_{GB}/\partial T\right)_{P,\,\mu_i} = -S^{XS}$; thus, γ_{GB} can be reduced with increasing temperature for a high-entropy GB with positive and large S^{XS} [155]. however, realization of this strategy for a Ni-based alloy with common segregating elements like Zr, Nb, Ta, Mo, and W would require adding a substantial amount of total non-FCC alloying elements that often leads to a large amount of precipitates and/or formation of ordered phases, which complicates the explanation. Thus, we

propose two new strategies via using a bulk high-entropy effect (that can occur in conjunction with the GB high-entropy effect) and sluggish kinetics in this study.

As one new strategy to stabilize nanoalloys at high temperatures, we propose that the coupling between bulk high-entropy effects (*e.g.*, high-entropy matrix NiFeCoCr) and the effect of including one (or more) strong GB segregating element(s) (*e.g.*, Zr) can effectively reduce γ_{GB} as the driving force for grain growth, and this effect can occur concurrently with the high-entropy GB effect proposed in Ref. [155] (*e.g.*, introducing additional GB segregating elements like Nb and Mo) to enhance one another. This bulk high-entropy effect is consequence of a competition between GB segregation and bulk precipitation. Specifically, precipitation limits GB segregation. The mixing entropy can effectively lower the free energy of the bulk high-entropy phase with respect to precipitates, thereby increasing the solid solubility of individual segregating elements to allow more reduction in γ_{GB} within the solubility limit.

To examine the above hypotheses, we conducted numerical experiments using a statistical thermodynamic model for multicomponent GB adsorption [155] that is a generalization of the binary Wynblatt-Chatain model [156]. we also adopted a few simplifications (discussed below) to focus on investigating the bulk and GB entropy effects. The GB energy of an *N*-component alloy can be expressed as:

$$\gamma_{GB} = U_{GB}^{XS} - TS_{GB}^{XS} - \sum_i \Gamma_{GB}^i \mu_{Bulk}^i \tag{56}$$

The first two terms in Eq. (56) are the contributions from both excess internal (bonding and strain) energy and excess entropy (noting that the interfacial excess volume is zero in the Gibbs definition). In the third term, μ_i is the bulk chemical potential and Γ_i is the corresponding GB adsorption amount (interfacial excess of solute) of the *i*-th component (*i* = 1, 2, 3…*N*).

Extended from the binary Wynblatt-Chatain model [44], this model considers the bonding and strain energies, as well as the configurational entropies. For simplicity, we consider a general twist GB (with $J_{max} = 1$ in the Wynblatt-Chatain model) and the GB adsorption is limited to the two layers at the GB core (on the both sides of the core of the twist GB). The internal energy contribution can be expressed as:

$$U_{GB}^{XS} = -Qz_v n\sum_i X_{GB}^i e_{ii} + zn\sum_i \left(X_{GB}^i - X_{Bulk}^i\right)e_{ii} - 2n\sum_i X_{GB}^i \Delta E_{strain}^i + U_{GB}^{(\mathrm{int})}, \qquad (57)$$

where *Q* is the fraction of the broken bonds at the GB core, *z* is the total coordinates (number of bonds per atom), z_v is the number of bonds per atom between two adjacent layers, *n* is the atomic density (number of atoms per unit area in one atomic layer; noting that there two atomic layers at the core of a twist GB), X_{GB}^i and X_{Bulk}^i are GB and bulk compositions, respectively, e_{ii} is the (self) bonding energy the *i*-th component, ΔE_{strain}^i is the strain energy of the *i*-th component in the bulk. The last term in Eq. (56) represents the (non-ideal) interaction energies among different components, which vanishes for an ideal solid solution. The excess configurational entropy can be expressed as:

$$S_{GB}^{XS} = -2nk\sum_i (X_{GB}^i \ln X_{GB}^i - X_{Bulk}^i \ln X_{Bulk}^i), \quad (58)$$

where *k* is the Boltzmann constant. The adsorption of the *i*-th component is given by:

$$\Gamma_i = 2n(X_{GB}^i - X_{Bulk}^i). \quad (59)$$

The bulk chemical potential of the *i*-th component is:

$$\mu_i^{Bulk} = \mu_i^0 + kT \ln X_{Bulk}^i + \mu_i^{(\text{non-ideal})}, \quad (60)$$

where $\mu_i^0 = 0.5ze_{ii}$ and $\mu_i^{(\text{non-ideal})}$ is the interaction energy (resulted from non-ideal mixing). Combining Eqs. (57)-(60), the GB energy for a multicomponent alloy can be derived as:

$$\gamma_{GB} = -Qz_v n\sum_i X_{GB}^i e_{ii} - 2n\sum_i X_{GB}^i \Delta E_{strain}^i + 2n\sum_i kTX_{GB}^i \ln\left(\frac{X_{GB}^i}{X_{Bulk}^i}\right) + \gamma_{GB}^{(\text{non-ideal mixing})}, \quad (61)$$

where $\gamma_{GB}^{(\text{non-ideal mixing})}$ represents the contribution from non-ideal mixing. Assuming *i* = 1 is the matrix element, Eq. (S6) can be rewritten as:

$$\gamma_{GB} = \gamma_{GB}^{(0)} - 2n\sum_{i\neq 1} X_{GB}^i \Delta h_{ads.(i\to 1),0} + 2n\sum_i kTX_{GB}^i \ln\left(\frac{X_{GB}^i}{X_{Bulk}^i}\right) + \gamma_{GB}^{(\text{non-ideal mixing})}, \quad (62)$$

where $\gamma_{GB}^{(0)}$ $(= -nQz_v e_{11})$ represents the GB energy of the pure component 1 without any adsorption. In Eq. (62), $\Delta h_{ads.(i\to 1),0} \equiv Qz_v n\sum_i (e_{ii} - e_{11}) + \Delta E_{strain}^i$, which is introduced to represent the GB adsorption (*a.k.a.* segregation) enthalpy (where "0" in the subscript denotes ideal mixing) and is the main driving force for GB

adsorption/segregation. Here, $\Delta h_{ads.(i\to 1),0} \equiv \Delta H_{ads.(i\to 1),0} / N_A$, where N_A is the Avogadro constant, representing the enthalpic change associated with moving one atom of the *i*-th component from the bulk to the GB (via swapping it with one atom of component 1 at GB). A McLean-Langmuir type GB adsorption equation can be derived, via letting $\partial\gamma_{GB} \Big/ \partial X^{i}_{GB} = 0$, as:

$$\frac{X^{i}_{GB}}{X^{1}_{GB}} = \frac{X^{i}_{Bulk}}{X^{1}_{Bulk}} \exp\left(-\frac{\Delta h_{ads.(i\to 1),0} + \Delta h^{i\to 1}_{\text{non-ideal mixing}}}{kT} \right) \tag{63}$$

Subsequently, the equilibrium GB composition and corresponding GB energy can be calculated from Eq. (62) and Eq. (63).

To illustrate the bulk high-entropy effect (that is distinct from the GB high entropy effect shown in Fig. 6.1 in Ref. [155]), we first conducted numerical experiments using a symmetrical system consists of 1-5 matrix elements (M_1, M_2, M_3, M_4, and M_5) and one segregating element (S) where all elements mix ideally (so that $\gamma^{(\text{non-ideal mixing})}_{GB}$ = 0 and $\Delta h^{i\to 1}_{\text{non-ideal mixing}}$ = 0, which is a simplification that allow us to focus on the bulk and GB entropic effects instead of the potentially complex non-ideal interactions of different components). Specifically, we adopt the following parameters for computing the results shown in Fig. 6.2(a).

- the bonding energy $|e_{MM}|$ = 0.45 eV (z_v = 4) and Q = 1/6;
- the GB sites density n = 6.4 atoms/nm^2;
- the matrix-type elements do not segregate;

- the adsorption (segregation) energy for the element *S* is set as: $\Delta h_{ads.(S\to M_i),0} \equiv \Delta H_{ads.} / N_A$ = 0.9 eV/atom (similar to the typical segregation enthalpies of Zr in Ni or Fe);
- a 1:1 stoichiometric line compound *MS* can precipitate with $\Delta H_{ppt.} = \Delta H_{ads.} + 4$ kJ/mol (that is at the lower end of the typical range of $\Delta H_{ppt.} - \Delta H_{ads.} = 10 \pm 6$ kJ/mol [S3]); and
- all specimens are saturated with the segregating element *S* at all temperatures (in equilibrium with *S*-enriched precipitates), *i.e.*, the composition of the (main) solid-solution phase moves along the equilibrium bulk solvus line.

Moreover, we assumed that the precipitation energy obeys the following empirical relationship [157] for computing Fig. 6.2(b):

$$\Delta H_{ppt.} = \Delta H_{ads.} + 10 \ \text{kJ/mol} \tag{64}$$

The inset of Fig. 6.2(a) shows that the solid solubility can be increased in the ternary system M_1-M_2-*S*, as compared with two binary subsystems, M_1-*S* and M_2-*S*. Subsequently, Fig. 6.2(a) shows that increasing *N* (the number of matrix elements M_i) results in more reduction in γ_{GB} and makes $d\gamma_{GB}/dT$ more negative to reduce the thermodynamic driving forces for grain growth at high temperatures.

The same generalized Wynblatt-Chatain model was used to compute Fig. 6.2(b) for a multicomponent system with bonding and segregation energies to represent those of the real Ni systems, where we ignored the interactions among

different elements to simplify the calculations (while still capturing the important trends). The bonding energy was assumed to be $|e_{ij}|$ = 0.68 eV/atom so that the "clean" GB energy is identical to the measured $\gamma_{GB}^{(0)}$ = 0.93 J/m^2 [109]. The $\Delta h_{ads.(M\rightarrow Ni),0}$ values were estimated by considering both strain energies (estimated by the Friedel model) and bonding/interfacial energies (estimated from the atomization enthalpies). The estimated $\Delta h_{seg}^{\varepsilon+\gamma}$ are listed in Table 6.1. Fig. 6.2(b) suggests that a $Ni_{29}Fe_{23}Co_{23}Cr_{23}Zr_2$ alloy will have substantially lower γ_{GB}, as compared with both a binary counterpart ($Ni_{93}Zr_7$) and the conventional high-entropy counterpart ($Ni_{25}Fe_{25}Co_{25}Cr_{25}$); here, only Zr is a strong segregating element (Supplementary Table 6.1). Fig. 6.2(b) further suggests that adding two additional segregating elements, Nb and Mo, can further reduce γ_{GB} for a $Ni_{25}Fe_{23}Co_{23}Cr_{23}Mo_2Nb_2Zr_2$ alloy via a GB high-entropy effect, in addition to the bulk high-entropy effect to reduce γ_{GB}; this GB high-entropy effect is evident by the kink in the γ_{GB} *vs.* temperature curve in the Fig. 6.(b), below which more reduction in γ_{GB} and more negative $d\gamma_{GB}/dT$ are a result that both Zr and Nb are saturated so that the bulk composition moves along a ternary solvus line to produce a GB high-entropy effect, as suggested in Ref. [155]. Subsequently, these four alloys discussed above were fabricated and examined; the experiments (discussed in detail later) supported the theories and modeling results.

Furthermore, Fig. 6.2(b) shows the computed γ_{GB} *vs.* temperature curves for several cases, where the bonding and segregation energies were selected to represent the real Ni based alloys.

6.3. High entropy effect on GB kinetics

An additional scheme/strategy to stabilize nanoalloys is to utilize kinetic effects, which is often coupled with the thermodynamic effects. Multicomponent segregation at GBs may maximize the solute-drag effects, which can be further enhanced through a so-called high-entropy “sluggish kinetics” effect [158, 159]. First, a multicomponent alloy with different atomic sizes and bonding characteristics usually has local sites with a wider distribution of metastable energy levels (than those in unary and binary alloys). On one hand, when an atom jumps into a low-energy site, it can be trapped. On the other hand, if the site has a high energy, the atom has a higher chance to hop back to its original site so it does not contribute to diffusion effectively [29]. The combination of both scenarios may (on average) slow down the diffusion, as being demonstrated in the modeling of bulk diffusion in CoCrFeMnNi [160]; we believe that similar mechanisms may also slow down the migration of high-entropy GBs. Second, the diffusion rates of different elements in a GB with multicomponent adsorbates are different. Since the GB migration needs collective and cooperative diffusion of all adsorbates [161], grain growth may be pinned by the slowest segregating element. Similar sluggish kinetics effects have been demonstrated via diffusion-couple experiments in AlCoCrFeNi alloys [162]. Furthermore, Zener pinning can also play an important role to hinder the grain growth [163] and a multicomponent alloy may have more chances for effective Zener pinning by multiple (and different) precipitates that form at different temperatures. Finally, it is important to note that high-entropy GBs may also exhibit fast (instead of sluggish) kinetics in some other cases or under certain

conditions. As one example of such possibilities, multicomponent segregation can promote GB disordering at high temperatures, which can in turn drastically increase interfacial kinetics (and potentially trigger abnormal grain growth [164]).

6.4. Experiments and discussion

To test the proposed theories and strategies, nanoalloys were prepared via mechanical alloying. High-purity powders were well blended and sealed into a grinding vial in Ar atmosphere before high energy ball milling (HEBM; using a SPEX 8000D miller) for 20 hours. Hardened steel grinding vials and balls were used. The ball-to-powder mass ratio was 5:1, with 1 wt. % stearic acid as processing control agent. The mechanically-alloyed specimens were annealed in Ar + 5% H_2 atmosphere at 600 ºC, 900 ºC and 1000 ºC, respectively, for different durations (5 and 20 hours). The specimens were examined by X-ray diffraction (XRD) and transmission electron microscopy (TEM).

XRD (Fig. 6.3) showed that all specimens contain primarily an FCC phase, albeit the presence of small fractions of secondary phases in some cases. The grain sizes estimated by the Scherrer equation are presented in Table 6.2, which have been verified by direct TEM measurements for selected specimens (Fig. 6.5).

The $Ni_{29}Fe_{23}Co_{23}Cr_{23}Zr_2$ nanoalloy exhibited a stable grain size of ~19 nm after annealing at 600 °C and ~43 nm after annealing at 900 °C, which outperformed the binary counterpart $Ni_{93}Zr_7$ (Table I), as well as $Ni_{79}W_{21}$, the most stable binary Ni nanoalloy reported in literature [154] (Fig. 6.4). Moreover, a conventional high-entropy $Ni_{25}Fe_{25}Co_{25}Cr_{25}$ nanoalloy (for benchmarking) did not

exhibit a stable nanoscale grain size at 900 °C (Table 6.2), showing that a pure high-entropy matrix is not sufficient for stabilizing nanoalloys at high temperatures. Finally, the $Ni_{25}Fe_{23}Co_{23}Cr_{23}Mo_2Nb_2Zr_2$ alloy, which may be benefited from both bulk and GB high-entropy effects (Fig. 6.2(b)), exhibited even better high-temperature stabilities at 900 °C and 1000 °C (Fig. 6.2; Table 6.2). These observed trends are consistent with the thermodynamic modeling results shown in Fig. 6.2(b); however, we wish to note that kinetic stabilization effects should also play important roles in preventing grain growth in all cases.

To further examine the kinetic effects, we designed a $Ni_{80}Mo_{6.6}Ti_6Nb_6Ta_{1.4}$ alloy, where the Ti, Nb, and Ta contents were about 60-70% of the binary solid solubility limits at 900 °C (Table 6.3) while 6.6% Mo (*i.e.*, ~25% of binary solid solubility limit at 900 °C) was adopted to keep 80% of Ni. The Ti, Nb, and Ta contents in this alloy were about 60-70% of the binary solid solubility limits at 900 °C (Table 6.2), while 6.6% Mo (*i.e.*, ~25% of the binary solid solubility limit at 900 °C) was adopted to keep 80% of Ni. Thus, the thermodynamic effects on reducing GB energy should be less significant comparing with other cases. For this $Ni_{80}Mo_{6.6}Ti_6Nb_6Ta_{1.4}$ alloy, the computed GB composition from the simple McLean segregation model (that considers only the strain energy as the segregation driving force) contained equal fractions of each of five elements at T = 1000 °C so that the excess GB entropy should be large; however, we recognize that the real GB composition can differ significantly from that is estimated by the simple McLean model with strain energy only (or any other simple models) and the GB composition

should vary with temperature significantly (so it is infeasible to predict the optimal composition). Nonetheless, this composition represented a good example to test the kinetic effects. Our experiment demonstrated that the grain sizes were measured by XRD to be 16 nm, 36 nm, and 45 nm, respectively, for the $Ni_{80}Mo_{6.6}Ti_6Nb_6Ta_{1.4}$ specimens annealed at 600 °C, 900 °C, and 1000 °C, respectively (Table 6.2), representing a substantial improvement to binary nanoalloys (Fig. 6.4) and being in par with what have been achieved for the $Ni_{25}Fe_{23}Co_{23}Cr_{23}Mo_2Nb_2Zr_2$ nanoalloy (Table 6.2). We do recognize that it is almost impossible to know how much the stabilization is in fact due to kinetics (*vs.* thermodynamics); in most cases (including this instance), the stabilization should be a result of combined thermodynamic and kinetics effects.

We also characterized selected specimens with TEM (Fig. 6.5), where the grain sizes of the $Ni_{25}Fe_{23}Co_{23}Cr_{23}Mo_2Nb_2Zr_2$ and $Ni_{80}Mo_{6.6}Ti_6Nb_6Ta_{1.4}$ alloys annealed at 900 °C were measured to be 43 ± 13 and 32 ± 9 nm, respectively, which are in good agreement with the XRD measurements (Table 6.2). In comparison, the grain size of the binary $Ni_{93}Zr_7$ alloy was measured to be 189 ± 61 nm by TEM. The dark-field TEM images in Fig. 6.5 also show that the grains are homogeneous without any abnormally-large grains. The histograms of grain size distributions are shown in Fig. 6.5.

6.5. Conclusion

In summary, this study proposed and tested several new theories and strategies to utilize high-entropy GB complexions to enhance the thermal stability

of nanocrystalline alloys at high temperatures. First, we demonstrated, via numerical experiments, that GB energies could be reduced via bulk and/or GB high-entropy effects at/within the solid solubility limit to reduce the thermodynamic driving force for grain growth at high temperatures. Moreover, grain growth can be hindered by the high-entropy sluggish kinetics at GBs. To test these new theories, several nanoalloys were designed and fabricated to demonstrate outstanding thermal stabilities. Specifically, Fig. 6.3 compares our results with the reported grain sizes for nanocrystalline pure Ni [58] and $Ni_{79}W_{21}$ [154]. For pure Ni, the grains started to coarsen at 300-400 ºC. When Ni was alloyed with W, the coarsening temperature was improved to 600-700 ºC [71]. In this study, we successfully stabilized a Ni-based $Ni_{80}Mo_{6.6}Ti_6Nb_6Ta_{1.4}$ alloy and a Ni-containing high-entropy $Ni_{25}Fe_{23}Co_{23}Cr_{23}Mo_2Nb_2Zr_2$ alloy up to 1000 ºC via an innovative use of high-entropy GB complexions thru both thermodynamic and kinetic effects. This study provides a new pathway to stabilize nanocrystalline alloys at high temperatures, which can also be applied a broad range of other materials.

Chapter 6, in part, is a reprint of the material " Stabilization of nanocrystalline alloys at high temperatures via utilizing high-entropy GB complexions" as it appears in Scripta Materialia, Naixie Zhou, Tao Hu, Jiajia Huang, and Jian Luo, 2016, 124, 160-163. The dissertation author was the primary investigator and author of this paper. All experiments and data analysis were performed by the author except for the TEM characterization data.

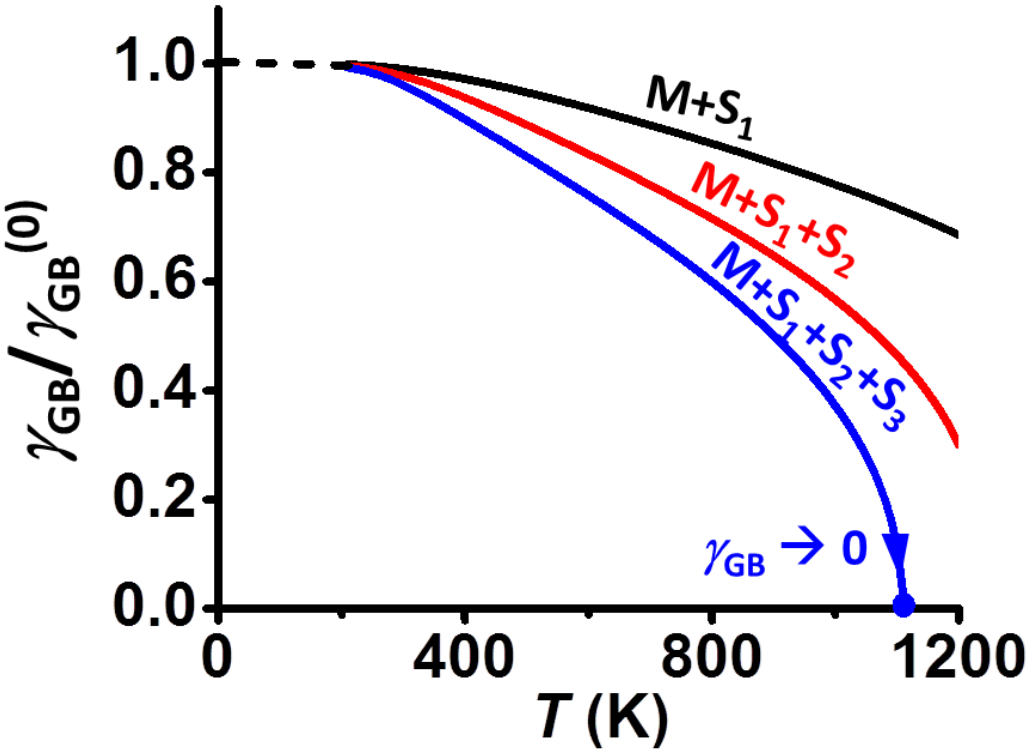

Figure 6.1 Illustration of a proposed new opportunity of utilizing "high-entropy GB complexions" to stabilize nanocrystalline alloys. Computed normalized GB energy *vs.* temperature curves along the bulk solvus lines (*i.e.*, for equilibrium saturated specimens on the "tips" of multicomponent solvus lines) for a regular solution with one, two, and three segregating solutes (S_1, S_2, and S_3) with identical adsorption enthalpies and pair-interaction parameters with the matrix element *M*. This numerical experiment demonstrates that it is theoretically possible to use GB adsorption of multiple solutes to achieve effective zero GB energy to stabilize nanocrystalline alloys at a true (instead of metastable) thermodynamic equilibrium (without going into the super-saturation region via kinetic inhibition of precipitation) at high temperatures. High-entropy GB complexions may also stabilize nanocrystalline alloys via two other (one thermodynamic and one kinetic) mechanisms discussed in text.

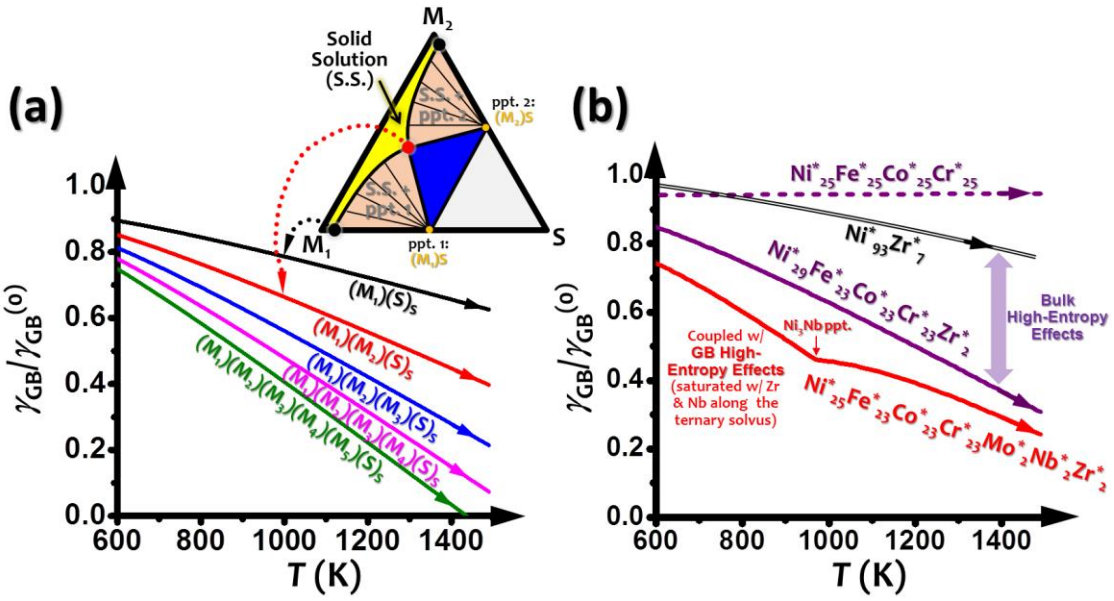

Figure 6.2 (a) The computed $\gamma_{GB}/\gamma_{GB}^{(0)}$ *vs.* temperature curves along the bulk solvus curves for symmetrical ideal solutions of 1-5 matrix elements (M_i) and one segregating element (S). The subscript "$_S$" denotes that all specimens are saturated with element S at all temperatures (in equilibrium with S-enriched precipitates). The inset is an isothermal section of a ternary phase diagram, where the binary and ternary compositions on the solvus (labeled by the black and red dots) correspond to the specimen compositions for calculating the first two (black and red) curves. (b) The computed $\gamma_{GB}/\gamma_{GB}^{(0)}$ *vs.* temperature curves for several "Ni-like" alloys. Here, the superscripts "*" are used acknowledge that the calculations were conducted by using a lattice model with segregation enthalpies and bonding energies to represent real alloys, but with simplifications, to capture the most important trends. The model and parameters are described in the Supplementary Materials.

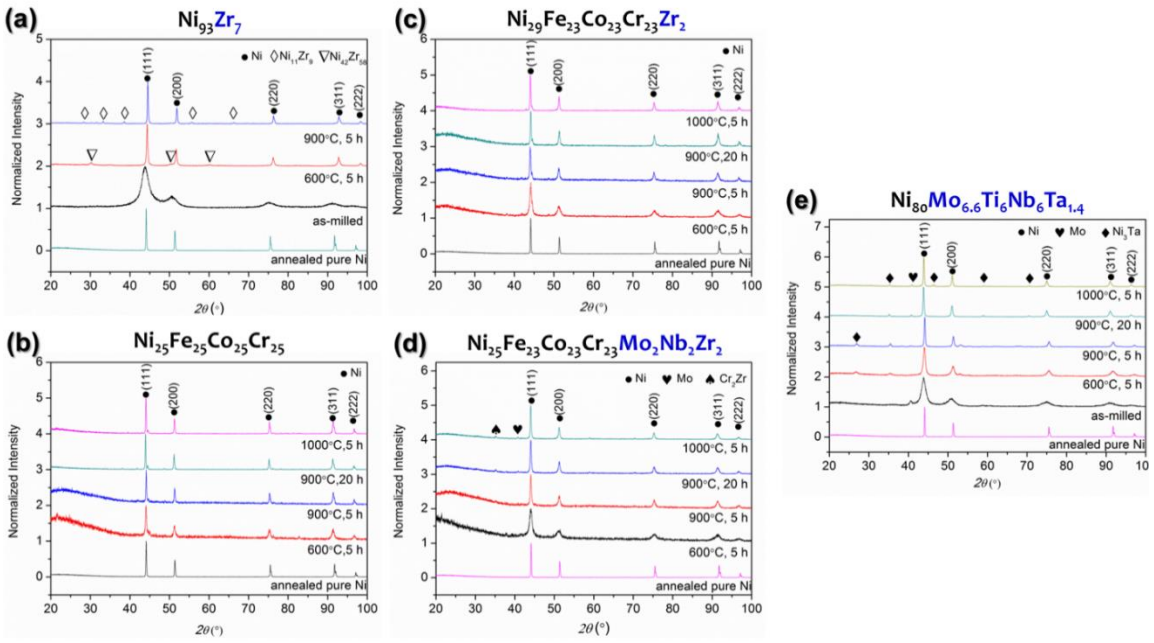

Figure 6.3 XRD patterns of as-milled alloys and specimens after annealing at different temperatures for various durations (labeled in the figures) for **(a)** $Ni_{93}Zr_7$, **(b)** $Ni_{25}Fe_{25}Co_{25}Cr_{25}$, **(c)** $Ni_{29}Fe_{23}Co_{23}Cr_{23}Zr_2$, **(d)** $Ni_{25}Fe_{23}Co_{23}Cr_{23}Mo_2Nb_2Zr_2$, and **(e)** $Ni_{80}Mo_{6.6}Ti_6Nb_6Ta_{1.4}$. The XRD pattern for the pure Ni annealed at 900 °C for 5 hours is also included as a benchmark. All specimens contain primarily an FCC phase, while minor amounts of precipitated secondary phases can be found in some cases.

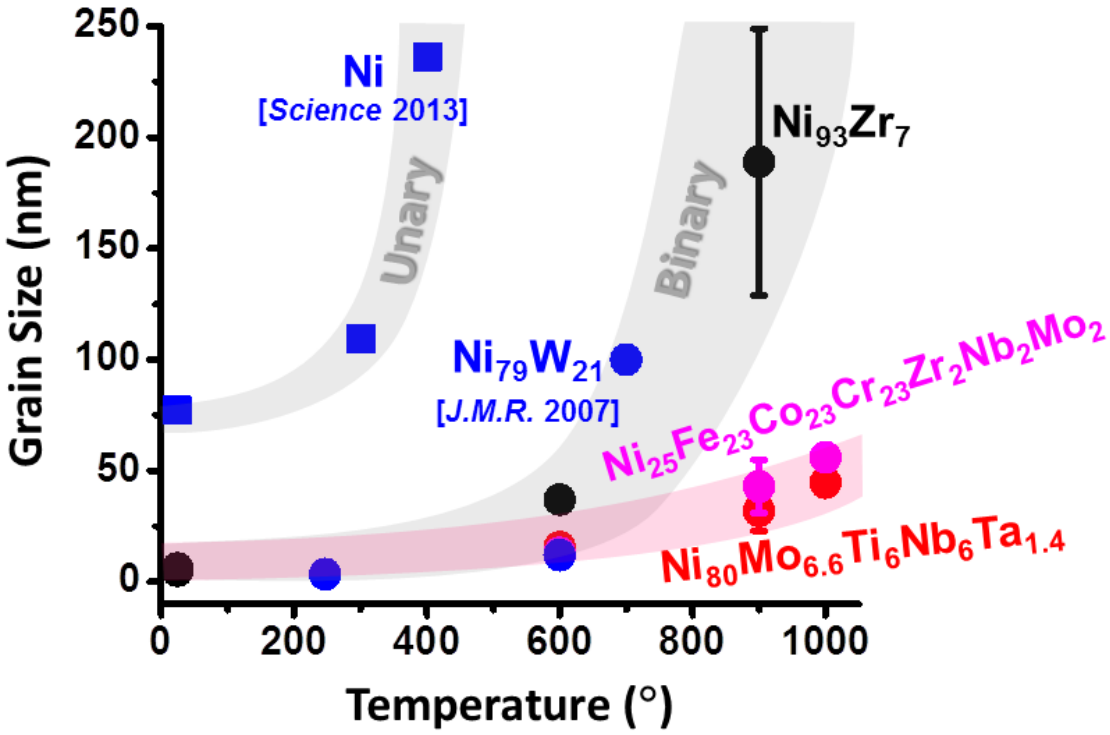

Figure 6.4 Measured grain sizes *vs.* annealing temperatures curves for the $Ni_{93}Zr_7$, $Ni_{25}Fe_{23}Co_{23}Cr_{23}Mo_2Nb_2Zr_2$, and $Ni_{80}Mo_{6.6}Ti_6Nb_6Ta_{1.4}$ alloys made in this study, along with the curves for pure Ni [164] and $Ni_{79}W_{21}$ [153] (representing the most stable binary Ni-based nanoalloy reported) from literature for comparison.

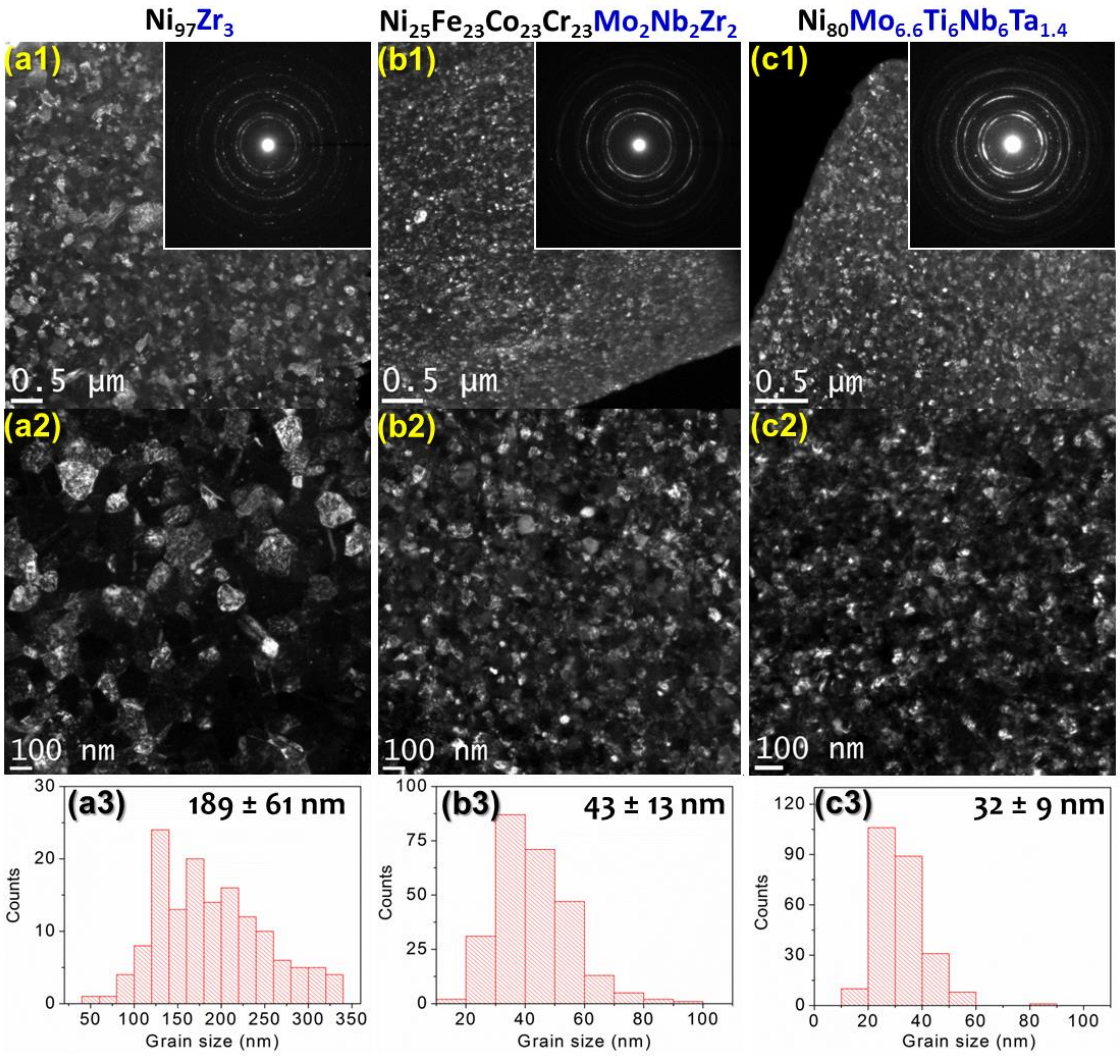

Figure 6.5 Dark-field TEM images (at a low magnification and a high magnification for each case) and the grain size histograms of three selected alloys after annealing at 900 °C for 5 hours, including: (a1), (a2) and (a3) for $Ni_{93}Zr_7$; (b1), (b2) and (b3) for $Ni_{25}Fe_{23}Co_{23}Cr_{23}Mo_2Nb_2Zr_2$; and (c1), (c2) and (c3) for $Ni_{80}Mo_{6.6}Ti_6Nb_6Ta_{1.4}$. The insets in (a1), (b1) and (c1) are selected area electron diffraction patterns.

Table 6.1 Estimated $\Delta h_{seg}^{\varepsilon+\gamma}$ (*i.e.*, $\Delta h_{ads.(M\rightarrow Ni),0}$ in Eq. (62) and Eq. (63), where *M* = Fe, Co, Cr, Mo, Nb, and Zr) for various elements in Ni.

	Fe	**Co**	**Cr**	**Mo**	**Nb**	**Zr**
$\Delta h_{seg}^{\varepsilon+\gamma}$ **(eV/atom)**	0.00	0.03	0.01	0.15	0.34	0.93

Table 6.2 Measured grain sizes of various specimens.

Composition	Grain Size Measured by XRD (and TEM), nm		
	600 °C	900 °C	1000 °C
$Ni_{93}Zr_7$	25	>60 (189)	coarse
$Ni_{25}Fe_{25}Co_{25}Cr_{25}$	43	coarse	coarse
$Ni_{29}Fe_{23}Co_{23}Cr_{23}Zr_2$	19	43	>60
$Ni_{25}Fe_{23}Co_{23}Cr_{23}Mo_2Nb_2Zr_2$	12.5	36 (43)	56
$Ni_{80}Mo_{6.6}Ti_6Nb_6Ta_{1.4}$	16	36 (32)	45

Table 6.3 Comparison of the solid solubility limits of Mo, Ti, Nb, and Ta in Ni and the selected composition of this $Ni_{80}Mo_{6.6}Ti_6Nb_6Ta_{1.4}$ alloy.

	Mo	**Ti**	**Nb**	**Ta**
Solid Solubility in Ni at 900 °C	~27%	~10%	~10%	~2%
Selected Composition	6.6%	6%	6%	1.4%

Chapter 7. Summary and future work

The existence of GB complexion in polycrystalline systems can influence a wide spectrum of interface dominated materials macroscopic properties. Various GB thermodynamic models have been developed and used in prediction the formation of GB complexion formations in binary metallic systems and GB complexion diagrams were calculated using these models. However, binary systems commonly represent ideal systems, while real alloys usually include multiple types of components added intentionally or received unintendedly during the manufacturing process, therefore understanding the role of many-component interaction and its effect on GB complexion formation is practically useful. One of the focus of this research is to develop GB complexion models for many-component systems by extending existed GB models and then construct GB complexions diagrams considering many-component interactions.

In the first Chapter, a quantitative interfacial thermodynamic model has been developed for computing GB λ diagrams for multicomponent alloy systems to predict GB disordering and related sintering properties. The model computations have been applied to W-Ni-*M* (*M* = Fe, Nb, Ti, Cr, Zr and Co) and Mo-Si-B-*M* (*M* = Ni, Co and Fe) systems. The calculations and experiments demonstrated that the calculated GB λ diagrams can forecast some useful trends in the relative effectiveness of various sintering aids. Multicomponent GB λ diagrams can help developing co-alloying strategies to control GBs as well as selecting the optimal

combination of multiple alloying elements, where the Edisonian approach is no longer efficient.

The second goal of this research is to understand the underlying thermodynamic mechanism and the dominant factor controlling the layered GB complexion formations in metallic systems. In Chapter 3, we computed a GB complexion diagram with well-defined transition lines using a lattice model and CALPHAD data for Bi-doped Ni system. The computed results are compared with 0K DFT calculation results and the experiments results in two earlier report, as well as direct AC STEM characterizations. Future research should be conducted to compute and validate other GB complexion diagrams to realize a potentially-transformative scientific goal of constructing more GB complexion diagrams as a new materials science tool. In Chapter 4, using a lattice type Ising GB model similar to the lattice model, the systematic transition behaviors of GBs are discussed. A normalized segregation strength ϕ_{seg} is developed based on the thermodynamic modeling to represent the overall effects of strain, differential bonding energies, the misorientation of symmetrical twist boundaries as well as the mixing energy. 3-D GB transition diagrams are developed by calculating GB adsorptions in the three-dimensional spaces of the ϕ_{seg} , T/T_m and $\Delta\mu$, which demonstrates a continuous transformation of GB segregation behaviors according to the variation of GB's intrinsic properties. We also derived a series of analytic expressions of GB transition as a function of ϕ_{seg} , T/T_m and $\Delta\mu$. The systematics of GB complexion transition in this study exhibits phenomenological similarities to various the cases

of multilayer adsorption of inert gas molecules on the surfaces of attractive substrates, which enriches the classical GB segregation/adsorption theory. As the model used in this study doesn't consider the possible change of GB structures, future study can be conducted to include the effect of GB structural disordering.

This final goal of this thesis is to apply the GB thermodynamic theories to the development of novel thermodynamic framework of predicting equilibrium grain size of nanocrystalline alloys. In Chapter 5, A thermodynamic frame work is established based on the combination of a multilayer GB segregation model and CALPHAD method to predict the thermodynamic stability of binary nanocrystalline alloys. Using that framework, a useful diagram showing the regimes of stable and metastable nanocrystalline states is developed for Zr doped Fe system, which successfully predicted the equilibrium stable grain size of nanocrystalline Fe-Zr alloys. In future studies, new interfacial thermodynamic models that consider complex GB complexions beyond the classical GB segregation types can be further developed and incorporated. Further, to establish a new strategy of using many-component high entropy GBs to improve the thermal stability nanocrystalline alloys beyond the range that binary doping could achieve, we proposed and tested several new theories and strategies to utilize high-entropy GB complexions to enhance the thermal stability of nanocrystalline alloys at high temperatures. We demonstrated, via numerical experiments, that GB energies could be reduced via bulk and/or GB high-entropy effects at/within the solid solubility limit to reduce the thermodynamic driving force for grain growth at high temperatures. Moreover, grain growth can be hindered by the high-entropy sluggish kinetics at GBs. Using

these strategies and principles, we successfully designed and synthesized a thermal stable nanocrystalline Ni-based $Ni_{80}Mo_{6.6}Ti_6Nb_6Ta_{1.4}$ alloy and a thermal stable nanocrystalline Ni-containing high-entropy $Ni_{25}Fe_{23}Co_{23}Cr_{23}Mo_2Nb_2Zr_2$ alloy. The study provides a new pathway to stabilize nanocrystalline alloys at high temperatures, which can also be applied a broad range of other materials.

References

[1] M. Tang, W.C. Carter, R.M. Cannon, Physical Review Letters 97(7) (2006) 075502.

[2] M. Tang, W.C. Carter, R.M. Cannon, Phys Rev B 73(2) (2006) 024102.

[3] P.R. Cantwell, M. Tang, S.J. Dillon, J. Luo, G.S. Rohrer, M.P. Harmer, Acta Materialia 62 (2014) 1-48.

[4] W.D. Kaplan, D. Chatain, P. Wynblatt, W.C. Carter, Journal of Materials Science 48 (2013) 5681-5717.

[5] S.J. Dillon, M.P. Harmer, J. Luo, JOM 61 [12] (2009) 38-41.

[6] J. Luo, Critical Reviews in Solid State and Material Sciences 32(1-2) (2007) 67-109.

[7] X. Shi, J. Luo, Phys Rev B 84(1) (2011) 014105.

[8] X. Shi, J. Luo, Applied Physics Letters 94(25) (2009) 251908.

[9] V.K. Gupta, D.H. Yoon, H.M. Meyer III, J. Luo, Acta Materialia 55 (2007) 3131-3142.

[10] J. Luo, V.K. Gupta, D.H. Yoon, H.M. Meyer, Applied Physics Letters 87 (2005) 231902.

[11] W. Liu, W. Pan, J. Luo, A. Godfrey, G. Ou, H. Wu, W. Zhang, Nature Communications 6 (2015) 8354.

[12] J. Huang, J. Luo, Phys. Chem. Chem. Phys. 16 (2014) 7786-98.

[13] A. Kayyar, H.J. Qian, J. Luo, Appl. Phys. Lett. 95(22) (2009) 221905.

[14] H.J. Qian, J. Luo, Y.M. Chiang, Acta Mater. 56(4) (2008) 862-873.

[15] H. Qian, J. Luo, Acta Materialia 56 (2008) 4702-4714.

[16] J. Luo, Y.-M. Chiang, Annual Review of Materials Research 38 (2008) 227-249.

[17] H.J. Qian, J. Luo, Applied Physics Letters 91(6) (2007) 061909.

[18] J. Luo, M. Tang, R.M. Cannon, W.C. Carter, Y.-M. Chiang, Mater. Sci. Eng. A 422 (2006) 19-28.

[19] J. Luo, Y.-M. Chiang, R.M. Cannon, Langmuir 21 (2005) 7358-65.

[20] J. Luo, Y.-M. Chiang, Acta Mater. 48(18-19) (2000) 4501-4515.

[21] J. Luo, H. Wang, Y.-M. Chiang, Journal of the American Ceramic Society 82 (1999) 916.

[22] M. Baram, D. Chatain, W.D. Kaplan, Science 332 (2011) 206-209.

[23] M. Baram, W.D. Kaplan, J. Mater. Sci. 41(23) (2006) 7775-7784.

[24] S.J. Dillon, M.P. Harmer, Acta Materialia 55 (2007) 5247-5254.

[25] S.J. Dillon, M.P. Harmer, Journal of the European Ceramic Society 28(7) (2008) 1485-1493.

[26] S.J. Dillon, M. Tang, W.C. Carter, M.P. Harmer, Acta Materialia 55(18) (2007) 6208-6218

[27] M.P. Harmer, Journal of the American Ceramic Society 93(2) (2010) 301-317.

[28] S. Ma, P.R. Cantwell, T.J. Pennycook, N. Zhou, M.P. Oxley, D.N. Leonard, S.J. Pennycook, J. Luo, M.P. Harmer, Acta Materialia 61(5) (2013) 1691-1704.

[29] J. Luo, Journal of the American Ceramic Society 95(8) (2012) 2358-2371.

[30] J. Luo, Applied Physics Letters 95(7) (2009) 071911.

[31] J. Luo, H. Cheng, K.M. Asl, C.J. Kiely, M.P. Harmer, Science 333(6050) (2011) 1730-1733.

[32] A. Kundu, K.M. Asl, J. Luo, M.P. Harmer, Scripta Materialia 68 (2012) 146-149.

[33] S. Ma, K. Meshinchi Asl, C. Tansarawiput, P.R. Cantwell, M. Qi, M.P. Harmer, J. Luo, Scripta Materialia 66(5) (2012) 203-206.

[34] D. Raabe, M. Herbig, S. Sandlöbes, Y. Li, D. Tytko, M. Kuzmina, D. Ponge, P.P. Choi, Current Opinion in Solid State and Materials Science 18(4) (2014) 253-261.

[35] N. Zhou, J. Luo, Acta Materialia 91 (2015) 202-216.

[36] J. Luo, X.M. Shi, Applied Physics Letters 92 (2008) 101901

[37] J. Luo, Current Opinion in Solid State and Materials Science 12(5/6) (2008) 81-88.

[38] X. Shi, J. Luo, Physical Review Letters 105 (2010) 236102.

[39] J. Luo, Journal of Materiomics 1(1) (2015) 22-32.

[40] E.W. Hart, Scripta Metallurgica 2(3) (1968) 179-182.

[41] E.D. Hondros, M.P. Seah, Metallurgical Transactions 8A(9) (1977) 1363-71.

[42] R. Kikuchi, J.W. Cahn, Phys Rev B 21 (1980) 1893-1897.

[43] R. Kikuchi, J.W. Cahn, Phys Rev B 36 (1987) 418

[44] P. Wynblatt, D. Chatain, Materials Science and Engineering a-Structural Materials Properties Microstructure and Processing 495(1-2) (2008) 119-125.

[45] P. Wynblatt, D. Chatain, Metallurgical and Materials Transactions a-Physical Metallurgy and Materials Science 37A(9) (2006) 2595-2620.

[46] J.W. Cahn, Journal of Chemical Physics 66(8) (1977) 3667-72.

[47] J.M. Rickman, H.M. Chan, M.P. Harmer, J. Luo, Surface Science 618 (2013) 88-93.

[48] Y. Mishin, W.J. Boettinger, J.A. Warren, G.B. McFadden, Acta Materialia 57(13) (2009) 3771-3785.

[49] T. Frolov, Y. Mishin, J. Chem. Phys. 143(4) (2015) 044706.

[50] T. Frolov, M. Asta, Y. Mishin, Phys. Rev. B 92(2) (2015) 020103.

[51] T. Frolov, D.L. Olmsted, M. Asta, Y. Mishin, Nature Communications 4 (2013) 1899.

[52] T. Frolov, S.V. Divinski, M. Asta, Y. Mishin, Physical Review Letters 110(25) (2013) 255502.

[53] J. Gibbs, reprinted in JW Gibbs “The Scientific Papers” Vol. I, Dover, NY, 1961.

[54] D. McLean, Grain Boundaries in Metals, Oxford Press, London, 1957.

[55] P. Wynblatt, Z. Shi, Journal of Materials Science 40(11) (2005) 2765-2773.

[56] V.K. Gupta, D.H. Yoon, J. Luo, H.M. Meyer III, Preliminary Results of Activated Sintering Mechanism and Grain Boundary Prewetting/ Premelting in Nickel-doped Tungsten, in: M.Z.H. R. M. Lane, S. Lu (Ed.) Ceramic Nanomaterials and Nanotechnology IV, The American Ceramic Society, 2005, pp. 159-174.

[57] J.G. Dash, A.M. Rempel, J.S. Wettlaufer, Reviews of Modern Physics 78 (2006) 695-741.

[58] X.C. Liu, H.W. Zhang, K. Lu, Science 342(6156) (2013) 337-340.

[59] T. Chookajorn, H.A. Murdoch, C.A. Schuh, Science 337(6097) (2012) 951-954.

[60] J. Weissmüller, Journal of materials research 9(01) (1994) 4-7.

[61] J. Weissmüller, Nanostructured Materials 3(1) (1993) 261-272.

[62] H.A. Murdoch, C.A. Schuh, Acta Materialia 61(6) (2013) 2121-2132.

[63] M. Saber, H. Kotan, C.C. Koch, R.O. Scattergood, Journal of Applied Physics 114(10) (2013) 103510.

[64] R. Kirchheim, Acta Mater. 50(2) (2002) 413-419.

[65] K. Darling, B. VanLeeuwen, C.C. Koch, R.O. Scattergood, Materials Science and Engineering: A 527(15) (2010) 3572-3580.

[66] K.A. Darling, R.N. Chan, P.Z. Wong, J.E. Semones, R.O. Scattergood, C.C. Koch, Scripta Materialia 59(5) (2008) 530-533.

[67] K.A. Darling, L.J. Kecskes, B.G. Butler, Binary or higher order high-density thermodynamically stable nanostructured copper-based titanium metallic systems, and methods of making the same, US, 2015.

[68] T. Frolov, K. Darling, L. Kecskes, Y. Mishin, Acta Materialia 60(5) (2012) 2158-2168.

[69] A. Khalajhedayati, T.J. Rupert, JOM 67(12) (2015) 2788-2801.

[70] C.A. Schuh, T.G. Nieh, H. Iwasaki, Acta Materialia 51(2) (2003) 431-443.

[71] A.J. Detor, C.A. Schuh, Acta Materialia 55(12) (2007) 4221-4232.

[72] L. Li, M. Saber, W. Xu, Y. Zhu, C.C. Koch, R.O. Scattergood, Materials Science and Engineering: A 613 (2014) 289-295.

[73] B.K. VanLeeuwen, K.A. Darling, C.C. Koch, R.O. Scattergood, B.G. Butler, Acta Materialia 58(12) (2010) 4292-4297.

[74] M.A. Tschopp, H.A. Murdoch, L.J. Kecskes, K.A. Darling, JOM 66(6) (2014) 1000-1019.

[75] J.S. Lee, K. Klockgeter, C. Herzig, Colloque De Physique 51 (1990) C1-569.

[76] L.P.H. Jeurgens, Z. Wang, E.J. Mittemeijer, International Journal of Materials Research 100(10) (2009) 1281-1307.

[77] R. Benedictus, A. Böttger, E.J. Mittemeijer, Phys Rev B 54(13) (1996) 9109-9125.

[78] N. Eustathopoulos, M. Nicholas, B. Drevet, Wettabilty At High Temperatures Pergamon, Amsterdam, 1999.

[79] H. Bakker, Enthalpies in Alloys: Miedema's Semi-Empirical Model, Enfield Publishing & Distribution Company1998.

[80] A.F. Guillermet, Z. Metallkde 78(3) (1987) 165-171.

[81] P. Gustafson, CALPHAD: Comput. Coupling Phase Diagrams Thermochem 12(3) (1988) 277-292.

[82] K. Frisk, Calphad 14(3) (1990) 311-320.

[83] E.N. Hodkin, M.G. Nicholas, D.M. Poole, Journal of the Less Common Metals 20(2) (1970) 93-103.

[84] P. Gustafson, MTA 18(2) (1987) 175-188.

[85] A. Guillermet, MTA 20(5) (1989) 935-956.

[86] A.F. Guillermet, Z. Metallkde 78 (1987) 639-647.

[87] A. Bolcavage, U.R. Kattner, Phase Equilibria 17(2) (1996) 92-100.

[88] S.K. Lee, D.N. Lee, CALPHAD: Comput. Coupling Phase Diagrams Thermochem 10 (1986) 61.

[89] N. Wang, C. Li, Z. Du, F. Wang, CALPHAD: Comput. Coupling Phase Diagrams Thermochem 31(4) (2007) 413-421.

[90] S. Jonsson, Z. Metallkde 87 (1996) 784.

[91] P. Bellen, K.C. Hari Kumar, P. Wollants, Z. Metallkde 87(12) (1996) 972-978.

[92] J.I. Jung, N.X. Zhou, J. Luo, Journal of Materials Science 47(24) (2012) 8308-8319.

[93] J.K. Cochran, W.L. Daloz, P.E. Marshall, JOM 63 [12](12) (2011) 44-49.

[94] Y. Yang, Y.A. Chang, Intermetallics 13(2) (2005) 121-128.

[95] Y. Liu, G. Shao, P. Tsakiropoulos, Intermetallics 8(8) (2000) 953-962.

[96] K.E. Spear, M.S. Wang, Calphad 5(2) (1981) 109-113.

[97] M. Heilmaier, M. Kruger, H. Saage, J. Rosler, D. Mukherji, U. Glatzel, R. Volkl, R. Huttner, G. Eggeler, C. Somsen, T. Depka, H.J. Christ, B. Gorr, S. Burk, JOM 61 [7](7) (2009) 61-67.

[98] L. Kaufman, Calphad 3(1) (1979) 45-76.

[99] O. Teppo, P. Taskinen, Mater. Sci. & Techn. 9(3) (1993) 205 - 212.

[100] A. Davydov, U.R. Kattner, JPE 20(1) (1999) 5-16.

[101] C. Soon-Don, Calphad 16(2) (1992) 151-159.

[102] M. Hillert, C. Qiu, JPE 13(5) (1992) 512-521.

[103] B. Hallemans, P. Wollants, J.R. Roos, Z. Metallkd. 85(10) (1994) 676-682.

[104] J. Lacaze, B. Sundman, MTA 22(10) (1991) 2211-2223.

[105] Q. Gao, M. Widom, Phys. Rev. B 90(14) (2014) 144102.

[106] J. Kang, G.C. Glatzmaier, S.H. Wei, Phys. Rev. Lett. 111(5) (2013) 055502.

[107] L.S. Chang, K.B. Huang, Scripta Materialia 51(6) (2004) 551-555.

[108] G. Vassilev, V. Gandova, P. Docheva, Crystal Research and Technology 44(1) (2009) 25-30.

[109] T. Roth, Materials Science and Engineering 18(2) (1975) 183-192.

[110] Y. Masatake, S. Motoyuki, K. Hideo, Journal of Physics: Condensed Matter 16(23) (2004) 3933.

[111] I. Langmuir, Journal of the American Chemical Society 40(9) (1918) 1361-1403.

[112] R.H. Fowler, E.A. Guggenheim, Statistical Thermodynamics, Macmillan, New York, 1939.

[113] R. Pandit, M. Schick, M. Wortis, Phys Rev B 26(9) (1982) 5112-5140.

[114] N. Zhou, J. Luo, Materials Letters 115 (2014) 268-271.

[115] K.A. Darling, B.K. VanLeeuwen, J.E. Semones, C.C. Koch, R.O. Scattergood, L.J. Kecskes, S.N. Mathaudhu, Materials Science and Engineering: A 528(13–14) (2011) 4365-4371.

[116] J. Weissmuller, J. Nanostructured Mater. 3 (1993) 261.

[117] J. Weissmuller, J. Mater. Res. 9(1) (1994) 4-7.

[118] F. Liu, R. Kirchheim, Journal of Crystal Growth 264(1-3) (2004) 385-391.

[119] K.A. Darling, B.K. VanLeeuwen, C.C. Koch, R.O. Scattergood, Materials Science and Engineering a-Structural Materials Properties Microstructure and Processing 527(15) (2010) 3572-3580.

[120] B.K. VanLeeuwen, K.A. Darling, C.C. Koch, R.O. Scattergood, B.G. Butler, Acta Mater. 58(12) (2010) 4292-4297.

[121] C.E. Krill, H. Ehrhardt, R. Birringer, Z. Metallkd. 96(10) (2005) 1134-1141.

[122] C.C. Koch, R.O. Scattergood, K.A. Darling, J.E. Semones, J. Mater. Sci. 43(23-24) (2008) 7264-7272.

[123] C.C. Koch, Journal of Materials Science 42(5) (2007) 1403-1414.

[124] J.R. Trelewicz, C.A. Schuh, Phys. Rev. B 79(9) (2009).

[125] M. Saber, H. Kotan, C.C. Koch, R.O. Scattergood, J. Appl. Phys. 113(6) (2013) 063515.

[126] K.A. Darling, B.K. VanLeeuwen, J.E. Semones, C.C. Koch, R.O. Scattergood, L.J. Kecskes, S.N. Mathaudhu, Materials Science and Engineering a-Structural Materials Properties Microstructure and Processing 528(13-14) (2011) 4365-4371.

[127] U.R. Kattner, JOM 49(12) (1997) 14-19.

[128] Q.S. Mei, K. Lu, Progress in Materials Science 52(8) (2007) 1175-1262.

[129] T. Tanaka, S. Hara, Z. Metallkd. 92(5) (2001) 467-472.

[130] T. Tanaka, S. Hara, Z. Metallkd. 92(11) (2001) 1236-1241.

[131] M.P. Harmer, Science 332 (2011) 182-183.

[132] G. Kaptay, J. Mater. Sci. 47(24) (2012) 8320-8335

[133] C. Servat, C. Gueneau, I. Ansara, J. Alloys & Compds 220 (1995) 19-26.

[134] B.X. Liu, W.S. Lai, Z.J. Zhang, Adv. Phys. 50(4) (2001) 367-420.

[135] B.B. Straumal, S.G. Protasova, A.A. Mazilkin, G. Schütz, E. Goering, B. Baretzky, P.B. Straumal, Jetp Lett. 97(6) (2013) 367-377.

[136] B.B. Straumal, A.A. Mazilkin, S.G. Protasova, A.A. Myatiev, P.B. Straumal, B. Baretzky, Acta Mater 56(20) (2008) 6246-6256.

[137] B.B. Straumal, S.V. Dobatkin, A.O. Rodin, S.G. Protasova, A.A. Mazilkin, D. Goll, B. Baretzky, Adv Eng Mater 13(6) (2011) 463-469.

[138] J.D. Cox, D. Wagman, V.A. Medvedev, CODATA Key Values for Thermodynamics, Hemisphere Publishing Corp1989.

[139] T.A. ROTH, Mat Sci Eng a-Struct 18 (1975) 183--192.

[140] A. Paesano, S.R. Teixeira, L. Amarai, Hyperfine Interactions 67(1-4) (1991) 665-669.

[141] H. Gleiter, Acta Materialia 48(1) (2000) 1-29.

[142] L. Lu, X. Chen, X. Huang, K. Lu, Science 323(5914) (2009) 607-610.

[143] Y. Wang, M. Chen, F. Zhou, E. Ma, Nature 419(6910) (2002) 912-915.

[144] Y.H. Zhao, X.Z. Liao, S. Cheng, E. Ma, Y.T. Zhu, Advanced Materials 18(17) (2006) 2280-2283.

[145] H. Gleiter, Progress in Materials Science 33(4) (1989) 223-315.

[146] R. Birringer, Materials Science and Engineering: A 117 (1989) 33-43.

[147] B. Günther, A. Kumpmann, H.D. Kunze, Scripta Metallurgica et Materialia 27(7) (1992) 833-838.

[148] M. Tschopp, H. Murdoch, L. Kecskes, K. Darling, JOM 66 [6](6) (2014) 1000-1019.

[149] A.R. Kalidindi, T. Chookajorn, C.A. Schuh, JOM 67 [12](12) (2015) 2834-2843.

[150] H. Höfler, R. Averback, Scripta metallurgica et materialia 24(12) (1990) 2401-2406.

[151] Z. Gao, B. Fultz, Nanostructured materials 4(8) (1994) 939-947.

[152] A. Michels, C. Krill, H. Ehrhardt, R. Birringer, D. Wu, Acta materialia 47(7) (1999) 2143-2152.

[153] A. Khalajhedayati, Z. Pan, T.J. Rupert, Nature communications 7 (2016) in press.

[154] A.J. Detor, C.A. Schuh, Journal of Materials Research 22(11) (2007) 3233-3248.

[155] N. Zhou, T. Hu, J. Luo, Current Opinion in Solid State and Materials Science.

[156] P. Wynblatt, D. Chatain, Metallurgy and Materials Transactions 37A (2006) 2595-2620.

[157] P. Lejcek, Grain Boundary Segregation in Metals, Springer Berlin Heidelberg, 2010.

[158] Z.P. Lu, H. Wang, M.W. Chen, I. Baker, J.W. Yeh, C.T. Liu, T.G. Nieh, Intermetallics 66 (2015) 67-76.

[159] S. Praveen, J. Basu, S. Kashyap, R.S. Kottada, Journal of Alloys and Compounds 662 (2016) 361-367.

[160] K.Y. Tsai, M.H. Tsai, J.W. Yeh, Acta Materialia 61(13) (2013) 4887-4897.

[161] G. Gottstein, L.S. Shvindlerman, Grain Boundary Migration in Metals: Thermodynamics, Kinetics, Applications, CRC express, Florida, 1999.

[162] J. Dąbrowa, W. Kucza, G. Cieślak, T. Kulik, M. Danielewski, J.-W. Yeh, Journal of Alloys and Compounds 674 (2016) 455-462.

[163] R.D. Doherty, D.A. Hughes, F.J. Humphreys, J.J. Jonas, D.J. Jensen, M.E. Kassner, W.E. King, T.R. McNelley, H.J. McQueen, A.D. Rollett, Materials Science and Engineering: A 238(2) (1997) 219-274.

[164] V.K. Gupta, D.-H. Yoon, H.M. Meyer Iii, J. Luo, Acta Materialia 55(9) (2007) 3131-3142.